LAPPEENRANTA
UNIVERSITY OF TECHNOLOGY

Rafał Piotr Jastrzębski

DESIGN AND IMPLEMENTATION OF FPGA-BASED LQ CONTROL OF ACTIVE MAGNETIC BEARINGS

Thesis for the degree of Doctor of Science (Technology) to be presented with due permission for public examination and criticism in the Auditorium 1382 at Lappeenranta University of Technology, Lappeenranta, Finland on the 19th of December, 2007, at noon.

Acta Universitatis
Lappeenrantaensis
296

Supervisors Professor Olli Pyrhönen
Department of Electrical Engineering
Lappeenranta University of Technology
Lappeenranta, Finland

Professor Riku Pöllänen
Department of Electrical Engineering
Lappeenranta University of Technology
Lappeenranta, Finland

Reviewers Professor Jerzy T. Sawicki
Department of Mechanical Engineering
Cleveland State University
Cleveland, USA

Dr. Adam Piłat
Department of Automatics
AGH University of Science and Technology
Kraków, Poland

Opponent Professor Josu Jugo
Electricity and Electronics department
University of the Basque Country
Leioa (Bizkaia), Spain

ISBN 978-952-214-508-6
ISBN 978-952-214-509-3 (PDF)
ISSN 1456-4491

Lappeenrannan teknillinen yliopisto
Digipaino 2007

Abstract

Rafał Piotr Jastrzębski
Design and implementation of FPGA-based LQ control of active magnetic bearings
Lappeenranta 2007
159 p.
Acta Universitatis Lappeenrantaensis 296
Diss. Lappeenranta University of Technology
ISBN 978-952-214-508-6, ISBN 978-952-214-509-3 (PDF), ISSN 1456-4491

The need for high performance, high precision, and energy saving in rotating machinery demands an alternative solution to traditional bearings. Because of the contactless operation principle, the rotating machines employing active magnetic bearings (AMBs) provide many advantages over the traditional ones. The advantages such as contamination-free operation, low maintenance costs, high rotational speeds, low parasitic losses, programmable stiffness and damping, and vibration insulation come at expense of high cost, and complex technical solution. All these properties make the use of AMBs appropriate primarily for specific and highly demanding applications.

High performance and high precision control requires model-based control methods and accurate models of the flexible rotor. In turn, complex models lead to high-order controllers and feature considerable computational burden. Fortunately, in the last few years the advancements in signal processing devices provide new perspective on the real-time control of AMBs. The design and the real-time digital implementation of the high-order linear-quadratic controllers, which focus on fast execution times, are the subjects of this work.

In particular, the control design and implementation in the field programmable gate array (FPGA) circuits are investigated. The optimal design is guided by the physical constraints of the system for selecting the optimal weighting matrices. The plant model is complemented by augmenting appropriate disturbance models. The compensation of the force-field nonlinearities is proposed for decreasing the uncertainty of the actuator. A disturbance-observer-based unbalance compensation for canceling the magnetic force vibrations or vibrations in the measured positions is presented. The theoretical studies are verified by the practical experiments utilizing a custom-built laboratory test rig. The test rig uses a prototyping control platform developed in the scope of this work.

To sum up, the work makes a step in the direction of an embedded single-chip FPGA-based controller of AMBs.

Keywords: Active magnetic bearings, linear-quadratic control, unbalance compensation, field programmable gate arrays

UDC 681.587 : 621.822 : 621.318

Acknowledgments

This thesis is the result of the research work I carried out at Lappeenranta University of Technology (LUT) during the years 2004-2007. These years I have worked in the Laboratory of Control Engineering and Digital Systems, in the Department of Electrical Engineering. It is impossible to thank all who contributed to this work. Nevertheless, I would like to express my sincere gratitude to some people to whom I am deeply indebted.

First of all, I wish to thank you, my supervisors Professor Olli Pyrhönen and Professor Riku Pöllänen for the opportunity and priviledge to be your student, for scientific freedom, countless discussions, and your invaluable scientific guidance.

I would express my thanks to Professor Aki Mikkola, who has proofread part of the thesis. I thank you Dr. Jusi Sopanen, Dr. Antti Kärkkäinen, and M.Sc. Aki Penttinen for the fruitful collaboration on the AMB project. Thanks to all my working colleagues at LUT for creating the real inspiring working environment.

I would like to thank the engineers from the Electronics Design Center for the tricky control electronics and other laboratory personel. The practical results would not be possible without your contribution.

Special thanks to Ph.D. Hanna Niemelä for her patient language inspections and numerous comments on the layout improvements.

I am grateful to the pre-examiners Professor Jerzy T. Sawicki from the Cleveland State University and Dr. Adam Piłat from the AGH University of Science and Technology for examining the manuscript and their valuable comments.

The project was co-financed by the Finnish Funding Agency for Technology and Innovation – TEKES. Financial support by the Lappeenrannan teknillisen yliopiston tukisäätiö is greatly acknowledged.

Very special thanks to my parents for their love, encouragement, and support throughout all my studies.

Last but not least my dearest Ola – thank you for your true love, patience, and understanding during the lengthy preparation of this work.

Lappeenranta, November 2007

Rafał Piotr Jastrzębski

List of Appended Publications

I R. Jastrzębski, R. Pöllänen, O. Pyrhönen, "*Analysis of System Architecture of FPGA-based Embedded Controller for Magnetically Suspended Rotor*", IEEE Proceedings of the International Symposium on System-on-Chip, Tampere, Finland, pp. 128-132, 2005.

II R. Jastrzębski, R. Pöllänen, O. Pyrhönen, "*Real-Time Emulator of Magnetic Suspension System for FPGA-based Controller*", IEEE Proceedings of the International Conference on Mechatronics, Budapest, Hungary, July 3-5, pp. 98-103, 2006.

III R. Jastrzębski, R. Pöllänen, O. Pyrhönen, "*Real-Time Emulation of Magnetic Suspension System for Flexible Rotor in FPGA*", WSEAS Trans. on Circuits and Systems, vol. 5, no. 7, pp. 1081-1088, 2006.

IV R. Jastrzębski, R. Pöllänen, O. Pyrhönen, A. Kärkkäinen and J. Sopanen, "*Modeling and Implementation of Active Magnetic Bearing Rotor System for FPGA-based Control*", Proceedings of the tenth International Symposium on Magnetic Bearings, Martigny, Switzerland, August 21-23, CD proceedings, 2006.

V R. Jastrzębski, R. Pöllänen, O. Pyrhönen, "*Linearization of Force Characteristics of Active Magnetic Bearings for the FPGA-based LQ-controller*", IEEE International Conference on Industrial Technology, Mumbai, India, December 15-17, CD proceedings, 2006.

VI A. Penttinen, R. Jastrzębski, Pöllänen, O. Pyrhönen, "*Run-Time Debugging and Monitoring of FPGA Circuits Using Embedded Microprocessor*", IEEE Ninth Workshop on Design and Diagnostics of Electronic Circuits and Systems, Prague, Czech Republic, pp. 147-148, 2006.

Contents

Nomenclature

Symbols

a	coefficient
$\boldsymbol{A}$	state matrix in state-space representation
b	coefficient
$\boldsymbol{B}$	input matrix in state-space representation
$B, \mathbf{B}$	magnetic flux density; also called magnetic field (scalar, vector)
c	closed flux path
$\boldsymbol{C}$	output matrix in state-space representation
d	thickness, length
d_M	damping in mechanical model
d_r	rotor diameter
$\boldsymbol{D}$	feedthrough (or feedforward) matrix in state-space representation
$\boldsymbol{D}_\mathrm{M}$	damping matrix in mechanical model
D	electric flux density
$\mathbf{e}$	vector of reference error signals
$E, \mathbf{E}$	electric field (scalar, vector)
$f, \mathbf{f}$	force (scalar, vector)
F	function
g	gravity constant
G	transfer function
G_P	proportional gain
G_F	feedforward gain
$\boldsymbol{G}$	gyroscopic matrix in mechanical model

$\boldsymbol{G}_{\mathrm{pl}}$	transfer function matrix of plant
$\boldsymbol{G}_{\mathrm{c}}$	transfer function matrix of controller
$H, \mathbf{H}$	magnetic field strength (scalar, vector)
i	current
i_{cc}	compensated control current
i_{cp}	compensation current
$\mathbf{i}$	vector containing currents
$\mathbf{I}$	unity matrix
I	mass moment of inertia
j	increment variable or index of summation, integer
$J, \mathbf{J}$	current density (scalar, vector)
$\boldsymbol{J}$	Jacobean matrix
J_{Q}	cost function or performance index
$\boldsymbol{K}$	gain matrix in state-feedback law
k	increment variable or index of summation, integer
k_i	current stiffness (actuator gain)
k_x	position stiffness (negative open-loop stiffness)
k_{M}	stiffness in mechanical model
k_u	velocity-induced voltage coefficient
$\boldsymbol{K}_i$	matrix of actuator gains
$\boldsymbol{K}_{\mathrm{M}}$	stiffness matrix in mechanical model
$\boldsymbol{K}_x$	open-loop stiffness matrix
$l, \mathbf{l}$	length of flux path (scalar, vector)
l_0	nominal air-gap
L	inductance
L_{a}, $\mathbf{L}_{\mathrm{a}}$	angular momentum (scalar, vector)
L_{br}	bearing core length
$\boldsymbol{L}$	proportional gain matrix in estimator design
m	mass
M	number of modes, upper summation index

$\boldsymbol{M}$	mass matrix in mechanical model
n	density of carrier electrons in conductor
N	number of coil turns
$\boldsymbol{N}$	linkage matrix
P	number of nodes
P_{p}	polynomial
r	radius
R	resistance
$\boldsymbol{R}$	control weighting matrix
$\boldsymbol{R}_v$	measurement noise intensity matrix or covariance
$\boldsymbol{R}_w$	process noise intensity matrix or covariance
s	Laplace variable
$S, \mathbf{S}$	area (scalar, vector)
$\boldsymbol{S}_{\mathrm{m}}$	position measurement sensors matrix
t	time
T	sample period
$\boldsymbol{T}$	transformation matrix of state variables
$\boldsymbol{T}_u$	transformation matrix of input variables
$\boldsymbol{T}_y$	transformation matrix of output variables
u	voltage
$\mathbf{u}$	vector of inputs in state-space representation
q	electron charge
$\boldsymbol{Q}$	state weighting matrix
v, $\mathbf{v}$	velocity (scalar, vector)
V	volume
$\mathbf{w}$	vector of total control effort (at the output of the controller)
W_1	disturbance attenuation factor
W_2	additive plant discrepancy bound
W_3	multiplicative plant discrepancy bound
W_{ce}	electromagnetic field co-energy

W_{fe}	electromagnetic field energy
W_{P}	dissipation energy
W_{T}	kinetic energy
W_{V}	potential energy
$\boldsymbol{W}$	weighting matrix
x	displacement in x axis
$\mathbf{x}$	space coordinates, vector of displacements or state variables in state-space representation
y	displacement in y axis
$\mathbf{y}$	vector of outputs in state-space representation or vector of measurements
$\mathbf{y}_j$	deflection of a point of the elastic body
z	displacement in z axis
z_0	location of the center of gravity on z axis
α	distribution of sensors on stator circumference, measured in degrees
β	tilting angle of the rotor
δ	angle between ideal sensing line and actual sensing line
ζ	damping ratio
η	modal amplitude
$\boldsymbol{\eta}$	vector of modal amplitudes or modal coordinates
θ	gain and offset in measured position
ϑ	parameter in the Pincer procedure
μ_0	permeability of vacuum
μ	relative permeability
ξ	time delay
$\boldsymbol{\rho}$	vector of input disturbance signals
σ	real part of complex pole
$\bar{\sigma}$	the greatest singular value
ς	phase angle
τ	time constant
$\boldsymbol{\upsilon}$	vector of imput disturbances

ϕ	phase
$\boldsymbol{\phi}$	mode shape vector
χ	force acting angle
ψ	magnetic flux linkage
ω	angular frequency
Γ	describing function
Θ	torque
Λ	determinant
Σ	summation
$\mathbf{\Phi}$	mode shape matrix
Φ_m	magnetic flux
$\mathbf{\Phi}_\mathrm{m}$	vector of magnetic fluxes
$\mathbf{\Phi}_\mathrm{ml}$	vector of magnetic loop fluxes
$\mathbf{\Psi}$	vector of magnetic flux linkages
Ω	rotational speed
Ω_p	angular velocity of precession
$\mathfrak{R}$	reluctance
$\boldsymbol{\mathfrak{R}}$	reluctance matrix
$\nabla\times$	curl operator
$\times$	vector product

Subscripts

A	referring to the end-A of the rotor with bearing A
a	actuator
air	air
b	bearing coordinates
B	referring to the end-B of the rotor with bearing B
base	base value
bias	bias
BW	bandwidth
c	control

cl	closed loop
d	damped
DC	direct current
del	delay
dist	disturbance
dyn	dynamic
f	filter
fb	feedback
ff	feedforward
Fe	iron
flex	flexible
H	Hall
in	input
I	integral
ld	lead
L	Lorentz
LL	line to line
m	measured
max	maximal
md	modulation
ol	open-loop
out	output
p	primary
P	proportional
pi	proportional integral
pl	plant
r	rotor
ref	reference
rigid	rigid
rise	rise

s	settling
sd	secondary
sat	saturation
tri	triangle
x	x axis
y	y axis
z	z axis

Superscripts

g	global – complete model in physical coordinates in FEM or global coordinates
m	modal
pu	per-unit
r	residual
T	matrix transpose

Other symbols

$\bar{}$	estimated signal
$\angle$	angle

Abbreviations

ADC	analog-to-digital converter
ALU	arithmetic logic unit
AMB	active magnetic bearing
ASIC	application-specific integrated circuit
AU	arithmetic unit
CAD	computer-aided design
CAM	computer-aided manufacturing
DAC	digital-to-analog converter
DFT	discrete Fourier transform
DOF	degree of freedom

DSP	digital signal processor
EDA	electronic design automation
EMC	electromagnetic compatibility
FE	finite element
FEM	finite element method
FPGA	field programmable gate array
HDL	hardware description language
IDE	integrated design environment
INL	inverse nonlinearities
I/O	input-output
IP	intellectual property
LTI	linear time-invariant
LQ	linear-quadratic
LQR	linear-quadratic regulator
MAGLEV	magnetically levitated vehicles
MDOF	multi-degree of freedom
MIMO	multi-input, multi-output
mmf	magnetomotive force
MAC	multiply-accumulate
NoC	Network-on-a-chip
RAM	random access memory
RDS	rotor delevitation system, also known as retainer bearings, auxiliary bearings, touch-down bearings and safety bearings
RISC	reduced instruction set computer
RNM	reluctance network method
SDRAM	synchronous dynamic random access memory
SISO	single-input sinle-output
SoC	System-on-a-chip
TTL	transistor-transistor logic
UFRC	unbalance force rejection control
ZOH	zero-order hold
VHDL	very high speed integrated circuits hardware description language

Chapter 1

Introduction

1.1 From invention of the wheel to magnetic levitation

The invention of the wheel is regarded as one of the oldest and most famous human inventions. It originated in the geographical area watered by the Euphrates and Tigris Rivers referred to as the "Cradle of Civilization" in the fifth millennium BC, which falls in the late Neolithic (early village communities) before the Bronze Age. In the ancient Mesopotamia (modern Iraq), the first function of the invention was a potter's wheel, which was followed by a wheel-and-axle concept. However, the wheel appeared also in the Neolithic Europe. According to Małecki (1996), it is supposed that the earliest depiction of the function as a four-wheel, two-axles vehicle (wagon) is on a clay pot, ca. 4000 BC, excavated in Bronocice village in central Europe.

It is notable that when taking into account the macroscopic nature, there are no spinning wheels in plants and animals. Therefore, the invention of the wheel can be regarded as one of the breakthrough concepts in the history of engineering. According to the notable laureate of the National Medal of Science[1] Theodore von Kármán: "Scientists study the world as it is; engineers create the world that has never been". Whether we agree or not that the concept of the wheel is a creation of human ingenuity, it certainly gained significant publicity. Considering that there is not much use of a wheel without an axle and socket, which are predecessors of a sleeve bearing, it is regrettable that the invention of the bearing is belittled.

Since the ancient times, the development of bearings has been driven by a demand for higher speeds and extreme working conditions. An early type of wooden ball bearings was found in the wreck of a Roman ship dated to 40 BC. The idea of the caged ball bearings was described by an Italian physicist Galileo Galilei in the year 1600. Officially, the caged ball bearings were invented and applied by an English clockmaker John Harrison in his marine chronometer to successfully determine longitude at sea, in the mid 18th century. At the end of the 18th century and at the beginning of the 19th century, ball bearings were employed in an increasing number of applications. The modern self-aligning ball bearing was patented in 1907 by a Swedish engineer Sven Wingquist, who

---

[1] a medal given by the President of the United States to honor scientists and engineers

founded the SKF, today's largest bearing manufacturer in the world. Generally, ball bearings are not expensive but they are limited by a high friction, low load-carrying capacity, and short life for high-speed operation. The performance of ball bearings can be evaluated using a top rotational speed and bearing size, namely a DN number[2]. Modern hybrid ball bearings are capable of achieving the DN$\approx 1.5 \cdot 10^6$ (Popoli, 2000). The limitations of mechanical bearings can be overcome by the use of non-contact bearings. For the non-contact bearings, the DN number is limited by the rotor strength to centrifugal forces. To exemplify, assuming the achievable peripheral speed v =200 m/s, the DN=$200 \cdot 60 \cdot 10^3/\pi = 3.820 \cdot 10^6$. The examples of non-contact bearings are fluid bearings and magnetic bearings.

The fluid bearings support the load on a thin layer of liquid or gas. They can provide much lower friction than mechanical bearings, they are able to support heavier loads, and do not require frequent maintenance. As an example, the first Kingsbury/Michell fluid bearing (named after its inventors) in the USA was installed in Holtwood Hydroelectric Power Plant, and it has been in service without maintenance since 1912. It supports a water turbine and generator with a rotating mass of about 165 tonnes. The up-to-day technologies bring new extreme applications, which require contamination-free solutions, higher rotational speeds, lower vibrations, contactless support, operation in difficult environments (e.g. process gases, corrosive fluids, and high temperatures). In these applications, the conventional mechanical or fluid bearings have proven insufficient. From the point of view of such extreme or special conditions, the sufficient concept is magnetic levitation.

The idea of using magnetic levitation proved to be anything but trivial. The instability of the ferromagnetic body kept in free hovering in the six degrees of freedom by fixed magnets and electric charges was shown by Earnshaw (1842) and is known as Ernshaw's theorem. This theorem applies to the classical Maxwell's electromagnetism, which neglects quantum mechanics; it states that a static magnetic suspension of the ferromagnetic body cannot reach a stable equilibrium when the acting forces are inversely proportional to the square of the distances. However, the magnetic levitation is possible by violating the theorem's assumptions, such as the use of diamagnetic and superconducting objects or an oscillating magnetic field that induces an alternating current in a conductor, thus generating the levitating force. Another way to overcome the theorem is an active feedback. It took roughly a century to find out that stable free hovering and large forces can be achieved by ferromagnets and a continuously adjusted magnetic field. The effects of this evolution may be traced through the patents issued in two areas: a new means of transportation – the magnetically levitated vehicles (MAGLEVs) and active magnetic bearings (AMBs) applied to rotating bodies.

As the MAGLEVs' predecessor, we may consider Kemper's patent in 1937 (Kemper, 1937), and his practical experiments. Kemper described a system consisting of a load-carrying electromagnet, valve amplifiers and sensors. In fact, the properties of such a load-carrying magnet have a name that reminds of the famous invention mentioned earlier, a magnetic wheel. The magnetic wheel has not won the market, owing to the high costs of the tracks. The first in

---

[2] DN number equals to the product of a bearing diameter in [mm] and maximal speed in [rpm].

the world commercial high-speed conventional MAGLEV railway connected the Pudong international airport and Shanghai in 2004 (inaugurated in 2002). In spite of the tragic MAGLEV accident caused by a human error on September 22$^{\mathrm{nd}}$, 2006, at the test track in Lathen, Germany, the technology is regarded as the safest, fastest and most reliable ground transportation method ever invented. The successful use of the magnetic levitation in ground transportation is leading to other interesting applications; for example Foster-Miller is building a system, called maglifter, to launch rockets into outer space (Foster-Miller, 2007).

When considering the support of rotors, in 1937, Beams and Holmes at the University of Virginia used an electromagnetic suspension for testing material strength. One of their experiments concerned the electromagnetic suspension of a steel ball. The ball was 0.8 mm in diameter and it reached the rotational speed of 18 million rpm, in vacuum. At the University of Virginia, this work continued with relation to ultracentifuges used for purification of isotopes during the World War II. The early AMB patent concerning this work is assigned to aforementioned Beams and Holmes (1941). However, at that point, the AMB technology was not yet matured. The technology started to mature with the advances of solid-state electronics, digital control, and with the pioneering works of Schweitzer and Lange (1976) and Habermann and Liard (1979). The new solutions in this field have been reported in the biannual International Symposia on Magnetic Bearings, which have been organized since 1988. The advances of the last two decades in such fields as high-speed microprocessors for complex control algorithms, precise sensor technology, materials and coatings for high-stress and high-temperature operations, safety bearings technology, rotor dynamics, and modeling have made the AMBs a more competitive solution for rotating machinery. Despite these advances, the overall complexity and price are still limiting factors in widespread industrial use.

1.2 Active magnetic bearings in rotor suspension

In this section, the principles of operation, advantages, disadvantages and applications of the magnetic levitation are discussed. The magnetic levitation can be implemented using different technologies and different materials. For instance, the classification of different magnetic bearings and types of magnetic levitation is presented by Schweitzer et al. (2003). In addition, possible applications are numerous. Therefore, we narrow the scope to ferromagnetic bodies supported by electromagnets. In particular, classical active magnetic bearings in rotor suspension are considered.

The active magnetic levitation is based on an attractive magnetic force produced by an electromagnet on a ferromagnetic body. The forces acting in the opposite directions require a pair of electromagnets positioned on the opposite sides of the suspended body. The principle of operation for a single degree of freedom, using one horseshoe electromagnet is depicted in Fig. 1.1. The deviation of the body x_{m} from the central position is measured by a proximity probe and is used by the control unit as a feedback signal. The control unit reacts according to a specific control law with the control current i_{c} in the electromagnet, which produces magnetic force f in such a way that the body with a mass m remains in free hovering. This principle extends in the case of the rotor to all its degrees of freedom as illustrated in Fig. 1.2. In a typical active magnetic

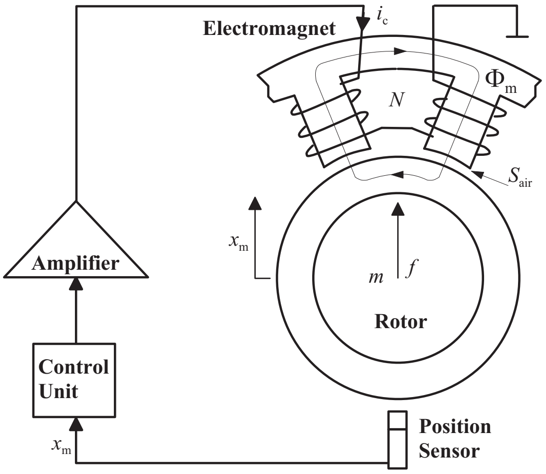

Figure 1.1: Principle of electromagnetic levitation for 1-DOF magnetic bearing system, where Φ_m, S_{air}, N, and m are the magnetic flux crossing the air-gap, the smallest cross-section area of the electromagnet (i.e., usually a stator tooth), number of coil turns, and mass.

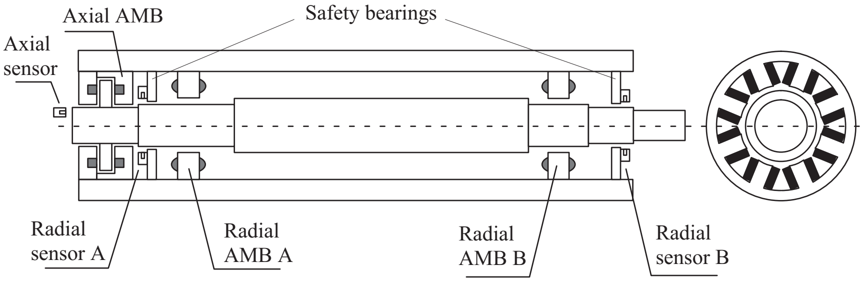

Figure 1.2: Principle of electromagnetic levitation for 5-DOF magnetic bearing system

bearing rotor system, ten electromagnets and five position measurements control five degrees of freedom of a rotating rotor with respect to the stationary part – namely the stator.

In general, the AMB system comprises three distinct parts: magnetic bearings, a control unit, auxiliary bearings or a rotor delevitation system (RDS). The bearings come in two configurations. The first one is a radial bearing, in which typically four electromagnets are symmetrically distributed around the rotor. That is, they generate the forces acting in two dimensions along x and y axes. In horizontal applications, the magnets are positioned in such a way that the gravity force is compensated by two electromagnets. This increases the load capability of the bearings. The second configuration is an axial bearing. It operates like the radial bearing but in one dimension only, that is along z axis. It comprises a ferromagnetic disk, attached to the rotor and electromagnets located at either side of the disk. The more technical treatment of the bearings and their modeling is given in Chapters 2 and 3, respectively.

The AMBs have specific properties, which differentiate them from mechanical and fluid bearings. First, they are able to provide completely contactless and fluidless support. This leads to the following advantages:

- contamination-free and seal-free solutions
- environmentally friendly solutions (no lubrication oil and no waste parts because of periodical maintenance)
- low maintenance costs
- high rotational speeds up to the rotor strength to centrifugal forces as explained earlier
- low breaking torques for high speeds (parasitic, hysteresis, and eddy-current losses), see e.g. (Schweitzer et al., 2003)
- in general, low power loss compared with the fluid film bearings (Chen and Gunter, 2005) because of low parasitic losses (power from drivetrain minus power converted to useful work)
- operation in difficult environments; e.g. process gases, corrosive fluids and high temperatures
- vibration insulation (low noise)

Second, they require active control owing to the system instability, which is usually viewed as the main difficulty. However, the presence of the control unit and sensors provides the following advantages:

- adjustable parameters, i.e., stiffness and damping, controllable system dynamics
- wide speed operation range
- active control of bending modes
- automatic balancing possibility
- diagnostics and monitoring built in the control unit

Third, the main AMB disadvantages pointed out in the literature, see e.g. (Wassermann et al., 2003), (Chen and Gunter, 2005) are:

- high costs when compared with conventional bearings
- breakdown of the load may be caused by a failure of any single component
- backup bearings must be provided; they also require extra space
- limited load carrying capacity in regard to required space (i.e. bearing load to pole face area ratio); the load that can be carried is lower than that of fluid (oil-film) bearings

For the time being, all these properties make the use of AMBs appropriate primarily for specific and highly demanding applications such as:

- turbo compressors, e.g. in natural gas, hydrogen, cooling and air process applications
- rotating equipment operating in vacuum without contamination, e.g. in biotechnology processes, clean rooms, semiconductor industry, and as turbomolecular pumps
- medical equipment, e.g. blood pumps
- energy generation products and energy storage, e.g. fly wheels, plant generators
- research and test applications, e.g. testing novel force and vibration control methods, measurement systems, testing rotor dynamics
- precise machine tools, e.g. milling, grinding and high-speed spindles
- high temperature bearings for aerospace and defense markets, e.g. gas turbine engines

The examples of early industrial applications of AMBs in contactless support rotors are given by Brunet (1988) and Dussaux (1990). With varying applications, also the sizes of magnetic bearings and their loads vary considerably, from the relatively small applications such as an artificial heart (Katoh and Masuzawa, 2006), to the gas-turbine in a nuclear power plant (Suyuan et al., 2006).

As far as the author knows, the first company to commercially market AMBs was the French S2M (Wagner, 1988), formerly Société de Mécanique Magnétique, founded in 1976. Since then, the number of companies producing the AMBs has been increasing. SKF, which had its own AMB solutions, purchased all the shares of S2M in summer 2007 (Brunet, 2007). Some other industrial players are: Foster-Miller Technologies, High Speed Tech Oy Ltd, LEViTEC, Levitronix, MECOS Traxler AG, Synchrony Inc., and Waukesha Bearings.

1.3 Digital control for embedded system

This section addresses the background and nomenclature of the digital control. The properties of the embedded real-time control systems are studied by the example of AMB rotor systems. The possible strengths and weaknesses of programmable logic circuits in an AMB control are introduced.

The modern computer science is often associated with the English mathematician, cryptographer and logician Alan Turing. His concepts of logical design and a universal machine have contributed to modern digital computers (Turing, 1936). The Turing machine and von Neumann architecture mark the beginnings of the digital revolution, which is a prerequisite for a digital control.

The first controllers of dynamical systems (e.g. AMB rotor systems) were implemented using analog electronics. The main advantage of the analog control was its short input-output delay compared with its early digital equivalents. However, most of the present-day control systems are implemented using digital computers, such as microprocessors, microcontrollers, and logic circuits.

To introduce the control, the physical processes are usually first approximated by continuous-time differential equations. However, digital computers cannot integrate, and they operate on sampled and quantized signals represented with binary numbers. Therefore, the differential equations have to be approximated again by reduction to sums and products only. These reduced, algebraic, recursive equations operate on discrete variables and are called difference equations. The process of transferring continuous-time models into time-discrete ones is called discretization. What is more, the analog signals are changed by the analog-to-digital converter (ADC) into digital ones, which can be represented by binary numbers. This process is sometimes referred to as digitization. The conversions occur periodically with periods of time equal T seconds (called sample period) and with the accuracy limited by the ADC capabilities and the resulting number format. The discrete signals can be changed back to the analog ones by using the DAC and the zero-order-hold (ZOH) circuitry, which holds the same value, usually voltage, on its output. To put it briefly: "Truth is much too complicated to allow anything but approximations" – the quotation attributed to John von Neumann.

To get back to the AMB rotor system, the measured analog signals represent the rotor's displacements from the central position and currents in the actuators, which produce the magnetic forces. In the actuators, switched power amplifiers are used, which do not require any additional DACs. The sampling period has to be selected according to the system bandwidth to keep the errors from the approximation small. In general, the smaller the physical dimensions of the rotor, the faster the system's dynamics and the wider the bandwidth. As a result, the shorter the sampling period, the tougher the time and number format requirements for the real-time digital controller. Too short a sampling period can lead to numerical problems when integrating and to stability issues after discretization of the continuous time controllers.

The AMB controller is an embedded system, which has special purposes and specific requirements unlike a general-purpose computer. The controller has to perform only a few pre defined tasks:

- collecting and processing the system's measurements – displacements, currents, rotational speed, and performing a coordinate transformation of the displacements
- executing control algorithm, i.e., control of rotor position and rotor dynamics, adaptation of parameters according to changeable speed, control of currents in actuators, biasing of amplifier current signals
- controlling system in safety critical situations, e.g. in the case of rotor touch-down
- monitoring and diagnostics
- handling various non-time-critical tasks, e.g. user interface, calibration of sensors, clearance checking

Furthermore, the AMB controllers, as well as most of the embedded systems, have to be compliant with special requirements, which are for instance small size, low cost, very high reliability, or they must withstand severe conditions such as electromagnetic interference and disturbance, vibration, radiation, and heat.

Building and validation of the real-time embedded control for the active magnetic support of high-speed, flexible rotors is a very demanding engineering task. High performance and robust control systems often employ model-based and nonlinear control methods. However, applying accurate, high-order models (for controller synthesis and its validation) require higher overall complexity, modeling of faster dynamics, and above all, powerful processing devices.

Digital signal processors (DSPs) are especially dedicated microprocessors designed for real-time embedded control systems. They comprise the ADCs, DACs and efficient arithmetic logic units (ALUs). The first single chip DSPs were produced by Bell Labs and NEC in 1978 and 1980, respectively. In 1983, Texas Instruments, presented its first DSP TMS32010$^{\mathrm{TM}}$. It worked on 16-bit data, had a Harvard architecture, could perform multiply accumulate operation in 390 ns (Giang et al., 1988) and was very successful. Texas Instruments is now the number one producer of DSPs. The modern DSPs provide some features in order to increase parallelism in data processing, such as parallel accumulator and multiplier, parallel memory architecture. Despite that, they could still be classified as serial processing devices when compared with modern field programmable gate arrays (FPGAs).

Modern FPGAs offer even more computational power and more flexibility than microprocessors. The FPGAs were invented in 1984 by engineer Ross Freeman (Buell et al., 2007), who was also the co-founder of Xilinx (www.xilinx.com, 1994-2007) – the world's largest manufacturer of reconfigurable hardware chips. The FPGAs are built of programmable components, such as logic cells, memories, and arithmetic blocks, which are interconnected by a matrix of wires and programmable switches. Such an architecture offers parallel processing capabilities and plenty of input-outputs (I/Os) for interfacing with the outside world. The FPGAs employed in the AMB control systems bring new possibilities for implementing novel control strategies and extend the area of possible industrial applications.

Unfortunately, the design work, which involves large FPGAs employed for complex controllers, faces many difficulties such as long and complex design flow, lack of superior tools, awkward testing, and the absence of complete and verified libraries for use in control applications.

1.4 Related work

Since the beginnings of the AMB technology, the complexity of the solutions as well as constantly growing number of possible applications have resulted in a significant amount of scientific publications in the field. From the perspective of this dissertation, the important references concern: the model-based centralized AMB control, actuator linearization, details of the implementation, and in particular, FPGA-based realizations.

Speaking about the position control of the levitated body, in the first years of the AMBs development, the researchers were limited by the computing power of early microprocessors, and therefore focused on the controllers with low computational burden. In 1984, Bleuler (1984) presented a method for designing the decentralized PD controllers for rigid rotors. For a predefined structure, better results than PD and PID control were given by Larsonneur's direct design controller layout (SPOC-D) algorithm (Larsonneur, 1990), which produced the optimal low-order controllers, without taking into account the gyroscopic effect. This method closed the gap between the PID and linear-quadratic (LQ) control methods. In regard to the low computational cost and direct use of state feedback, the PID-based control and other decentralized solutions are still attractive for various applications, (e.g. Polajzer et al., 2006). Nevertheless, in some cases, neglecting a gyroscopic effect may cause even instability (Ahrens et al., 1996).

The model-based, coupled control structures, which take into account a gyroscopic effect, proved to be superior, in terms of unbalance response (while still without special unbalance compensation), to the decentralized controllers as stated by Zhuravlyov et al. (1994), Ahrens et al. (1996), Zhuravlyov (2000), Piłat (2002), and Grega and Piłat (2005). These controllers were based on a LQ control of rigid rotors. Additionally, Piłat (2002) studied an LQ control applied together with a feedback linearization. Zhuravlyov (2000) presented an LQ control with a switching controller (as in that work copper losses were optimal). In general, the LQ control is suitable for applications that hold linearized models, where the plant model can be accurately determined, which in many applications is the case for AMBs.

In AMBs, the model of a control plant consists of the actuators, filtered measurements and flexible rotor models. The accurate rotor model can be derived using finite element modeling as given by Chen and Gunter (2005), Yamamoto and Ishida (2001), and Genta et al. (1993). The model can then be further corrected by the experimental modal analysis, and the reduction of the number of degrees of freedom can be carried out. Finally, it is formed into the state-space representation and transformed in a suitable form for the controller development. The formulation and scaling of the flexible state-space rotor model used in this work is based on the works of Lantto (1999) and Genta (2005). The latter employs the complex coordinates in formulation of the system dynamics.

All applications exhibit certain model uncertainties, which may be associated either with modeling errors or with changing plant's dynamics (e.g. due to a considerable change in working conditions). For such uncertain AMB systems, adaptive and robust control could be applied. For instance, the adaptive controller based on the recursive prediction error method was used by Wurmsdobler (1997), the robust control like μ-synthesis was employed by Lösch (2002) and H^{∞} was utilized by Ren et al. (2006). A collection of different control schemes, based on H^{∞} was presented by Aeschlimann (2002). Ren et al. (2006) also used gain scheduling according to the rotational speed. The robust and adaptive control can alleviate model uncertainties up to some point, yet the control of AMBs still requires expert knowledge and application-specific design. Therefore, some authors have tried to automate the controller design (reduce modeling effort, minimize manual system identification and controller tuning); see for example Lösch (2002). Lösch's work is a good example how the model-based control, which took into account the flexible and gyroscopic effects, increased the complexity of the controller. According to Lösch (2002), the augmented model that included two flexible modes per plane was of order 44, and the resulting controller was up to order of 70. Such models were considered not practical for DSP realization so they were reduced to about 24 states and then discretized before implementation. The controllers similar in size were used in the work of Wurmsdobler (1997). Lösch's automated controller was able to identify the plant's dynamics when only a few initial parameters were known. In order to overcome this initial knowledge, an automatic initial levitation with AMBs was proposed by Glaser and Sandagol (2006), where almost no initial parameters had to be known. The comparisons of different position control methods applied in AMB rotor systems can be found in the works of Knospe and Collins (1996), Lösch (2002), and Grega and Piłat (2005). Last but not least, the robust design methods result in high-order, robust, but often relatively slow controllers.

As for the model-based position control, the starting point for this work is an optimal state-space controller with additional integrative feedback sugested by Wurmsdobler (1997) and Zhuravlyov (2000). Most components of the studied AMB rotor system can be effectively linearized, and therefore they comprise a plant suitable for LQ control method. Furthermore, the control loops are organized by the same token as those given by (Larsonneur, 1990) and Wurmsdobler (1997), that is, the position control serves as an outer control loop to the inner current control loops. The cascaded control structure makes the inner current control loop to look like the linear one to the position control. The fast inner high-gain feedback effectively linearizes the nonlinear inductance of the coil of the electromagnet.

In the inner current control loop, the differential driving mode is used to linearize the force-current-displacement characteristics of the electromagnets. However, in order to reduce losses, a reduced premagnetization current (bias current) is applied resulting in the still nonlinear characteristics - out of the operating point. This essential nonlinearity of the AMBs should be compensated, if high performance is required. The nonlinear performance characteristics of the radial AMB can be sufficiently determined by numerical computation methods studied by Nerg et al. (2005) and Polajzer et al. (2004). These obtained nonlinear models, after verification, can be used for building the force compensation and validation of control.

Different methods can be applied to alleviate the problem of compensating the actuator nonlinearities. One of the most popular methods in control engineering for compensating different nonlinear actuators is that of an inverse nonlinearity (INL) control as explained by Franklin et al. (1998). It assumes that nonlinearity is invertible and can be undone. Some variations of the INL method for AMBs were studied by Hoffmann et al. (1998), and by Skricka and Markert (2002), where a polynomial formulation was used in the implementation; and also by Oberbeck and Ulbrich (2002), where an analytical method was employed. The alternative solution such as an extended Kalman filter applied for accurate position measurements in the collocated system was presented by Schuhmann et al. (2006).

In the real-time control systems, the minimization of an input-to-output controller delay is of major importance. Therefore, functional and software integration of the actuator compensation should not introduce extra delay into the system. Hoffmann et al. (1998) sugested the integration of the INL compensation, into the digital controller. The improvement in this integration were given by Skricka and Markert (2002).

Another intrinsic problem in AMB applications is the unbalance compensation. For example, Bleuler et al. (1994) briefly summarizes different unbalance compensation methods. In this work, an observer-based unbalance compensation is proposed. The proposed method extends and applies to AMBs a basic technique for estimation of sinusoidal disturbances (Franklin et al., 1998).

As stated before, the embedded AMB control, which comprises fast dynamics and nonlinearities, requires fast signal processing and flexible hardware platforms. Literature reports many examples of digital magnetic suspension controllers realized with DSPs (Bleuler et al., 1994), (Knospe et al., 1997), (Schroder et al., 1998), and (Krach et al., 2003). Additionally, one has to bear in mind that the implementation of such an embedded control system needs careful prototyping. Regarding the efficient control prototyping, a PC-based platform that utilizes DSP for the AMB control, is presented by Schroder et al. (1998) and the control implementation in a RT-Linux and PC system is given by Humphrey et al. (1999). Considerations on a general software architecture of the AMB controller, when using microprocessors, are presented by Betschon (2000) and Schweitzer et al. (2003). Additionally, Betschon (2000) studies different approaches to reduce cost and size of the AMB system. However, most research activities focus on control and modeling. Usually research teams use industrial test rigs and control platforms in prototyping, for instance dSPACE, automated DSP code generation by Matlab® and Simulink®. The possibility of improving performance of the AMB controller, by replacing DSP with FPGA ia suggested by Krach et al. (2003), but only simple control structures are considered.

Regarding the use of FPGAs in the control design for power electronic applications, such as inverter type welding machine and frequency converter, the comprehensive study was carried by Rauma (2006). On the contrary, there were no similar studies about the use of FPGAs or application-specific integrated circuits (ASICs) in AMB control, which would include similar in detail aspects of realization.

In the control of the AMBs, the low level current control algorithms and a PWM are typically realized with the help of analog devices or special digital logic devices, that is, integrated circuits or programmable logic. In particular, not only DSPs but also ASICs and FPGAs are commonly used for the digital control of currents. This tendency is similar in all applications that involve a fast control of power electronics, for example fast inverter control algorithms (Jastrzębski et al., 2003) in electric motors.

In the early stage of the author's doctoral studies, he has been working on the implementation of an induction motor control, motor emulation, and the possibility of integrating a motor control with an inverter control (Jastrzębski et al., 2004a) and (2004b), in a single FPGA. These studies contribute to the idea of a single chip AMB controller that utilizes an FPGA-based embedded control platform.

The beginnings of AMB technology in Finland date back to 1985. In 1988, the Conference on High Speed Technology was held in Lappeenranta, where special attention was paid to magnetic bearings (Larjola, 1988). The electromechanical properties of the radial AMB were studied by Antila (1998), and the robust control of AMBs in subcritical machines was researched by Lantto (1999).

1.5 Outline of the thesis

The first objective of this work is to examine and describe the use of FPGAs in the real-time control of high performance AMB rotor systems. The complete working embedded FPGA-based control platform is built, tested and validated in laboratory conditions. The second objective is to develop the model-based

AMB controller, which explores the advantages of the designed control platform, takes into account the bending modes of the rotor (they controllability), and nonlinearities of the actuator. The requirements for the controller include a high performance and unbalance compensation, at variable rotational speeds. For the obtained controller a robust analysis is conducted. Furthermore, the thesis focuses not only on control and system level design issues, but also it addresses the hardware description language (HDL) design and testing problems. The specific design issues are considered: single chip control solution, emulation of AMB system, built-in testing, design portability and reusability, custom tailored digital arithmetic, on-chip interconnections, and the use of embedded processors. The available literature does not provide enough information on all these issues.

Last but not least, the research was a part of a wider work that aimed at building a completely custom AMB laboratory test rig with AMB actuators available for experimental testing of novel control algorithms and examination of rotor dynamics at Lappeenranta University of Technology. The project was co-financed by TEKES[3].

The dissertation is presented as an introduction to the collection of the original scientific publications. In addition to that, the thesis includes some original results, which have not been presented to the wider audience up to now.

The highlights of the appended publications and the contribution of the authors are reported below.

Publication I addresses a design and implementation of an application specific architecture (of AMB controller), in an FPGA circuit. The publication presents a prototyping platform that eases the development of control, testing and integration of tested algorithms into the FPGA. It shows the FPGA implementation of an AMB current controller of a set of ten H-bridge switching amplifiers. Different architectures and data flow of the AMB controller are examined. The paper shows the opportunities and threads of a flexible HDL implementation of an embedded control system.

Publication II analyzes the benefits of an FPGA-based real-time emulation for mechatronic applications. As a case study, AMBs for contactless support of rigid rotors, are selected. This publication shows that for a general class of state-space models with separable nonlinearities, it is possible to build an optimized hardware implementation of the plant emulator or state observer (a basic part of a state-space controller). The emulator can be used for real-time validation of the control system and its components. Publication II uses the 4-DOF rotor model from subsection 3.1.2.

Publication III includes the description of the real-time emulation of magnetic suspension system, with a flexible rotor, in FPGA. The publication compares the realizations of the rigid and flexible rotor models, which can be used for emulation or for the implementation of the controller. It introduces the concepts of: numerical conditioning of the fixed-point discrete-time model, discrete realization of differential equations, very high speed integrated circuits hardware description language (VHDL) implementation of the non-linear actuator model and state-space rotor model. The

---

[3] Finnish Funding Agency for Technology and Innovation

emulator and the LQ controller with integral feedback are tested in VHDL Mentor Graphics® ModelSim® simulations. Publication III utilizes the flexible rotor model from section 3.2.

Publication IV presents FEM of the rotor and different variants of the LQ position control (considered in regard to the rotor model). In the publication, the rotor model is obtained using the FEM, modal reduction technique and experimental analysis. Publication IV includes the VHDL implementation of the obtained flexible rotor model with the nonlinear actuator, but it focuses on the different variants of the position controller, their HDL implementations, and on an active damping of flexible modes.

Publication V describes an LQ control and nonlinearities compensation of a rotor suspended by AMBs. The LQ control is based on a state-space controller with an additional integrative feedback, and disturbance estimator. An effective compensation of performance variations in dynamic force characteristics of radial AMBs is performed using two nonlinear principles. The publication studies the well-known inverse nonlinearity method. Next, it presents a novel model reference-based method. It is shown that the proposed compensation provides certain advantages over conventional solutions. The overall control is tested with the flexible rotor model and the nonlinear AMBs. Finally, the paper presents an integration of the proposed compensation into the digital controller. Accurate modeling of the AMB nonlinearities in an FPGA is achieved by using multi-variable interpolation and look-up table.

Publication VI illustrates the technique of an in-circuit verification with the custom made embedded logic analyzer. The analyzer provides the means to monitor internal signals, state of buses, and registers of the embedded controller. The heart of the tool comprises of the hardcore PowerPC processor, in the Virtex$^{\text{TM}}$-II Pro FPGA-circuit. In addition to monitoring, the described tool is a feasible alternative to the similar commercial solutions.

Looking at the major contributions to the appended publications, the author developed all the programs in VHDL and Matlab, carried out the simulations, and was the main author of all the publications but Publication VI. In addition, he was involved in the testing, designing of the software part, and commissioning of the FPGA-based AMB rotor prototyping platform. The text of all the appended publications, with the exception of Publication VI and sections of Publication IV, was written by the author. The co-author R. Pöllänen developed the reluctance network model used for obtaining the accurate force field of radial AMB. The co-authors A. Kärkkäinen and J. Sopanen wrote the FEM code, performed the mechanical modeling, obtained the flexible modes and eigenfrequencies of the test rotor (the final test rotor, described in the thesis, is different though). They also wrote the sections of Publication IV, which required expertise in mechanical engineering. The remaining sections of Publication IV was written by the author. The co-author A. Penttinen was the main author of Publication VI. He developed the C++ code for the PowerPC processor in Virtex-II Pro; and he determined the transfer rates for different configurations of the communication between the FPGA, PowerPC, and PC console. In Publication VI, the AMB controller and the connection between the logic and the processor were realized and tested by the author. The co-authors R. Pöllänen and O. Pyrhönen supervised and inspired the appended publications and the whole AMB project.

The main body of the dissertation provides the reader with introductory information, the main topic treated in the organized and consistent manner, as well as the key results and conclusions. Experimental and simulation results are not organized in separate chapters, however, they follow through all parts of the dissertation. The main body is organized into six chapters.

Chapter 1 introduces the historical background, properties, applications and principles of operation of the magnetic bearings. Basic control of the AMB rotor system is discussed in the context of digital and embedded systems. A brief introduction to modern signal processing devices and their use in embedded control applications is given. The related work and important references in the studied field are listed. The outline, main goals and objectives of this dissertation are stated.

Chapter 2 considers the rotor, magnetic bearings, and control system as an mechatronic product. The hardware parts and control hardware of the studied prototype system are introduced; physical phenomena behind their principles of operation are shown. The necessary background for the accurate system modeling is prepared.

Chapter 3 discusses modeling of the AMB rotor system for the control synthesis and its validation. The reader is introduced to the rotor modeling and main system nonlinearities. The construction of the overall plant model is presented. The viability of models with different complexities is considered. In particular, a FEM rotor model is developed and corrected, according to a modal analysis, to match the prototype sufficiently to design reliable model-based controllers. The effect of the reduced premagnetization current on the force characteristics of the radial AMB is discussed.

Chapter 4 studies the design of the controller, its inner and outer control loops, their requirements and realizations. The classical decoupled PID-based position control and LQ model-based control methods are discussed. The main concern are LQ control based on physical quantities and different methods of the force-field linearization. Special attention is paid to the automated LQ controller design and selection of the weighting functions for the LQ performance index. Furthermore, the unbalance compensation, robust stability analysis, and the controller evaluation according to the selected criteria are presented.

Chapter 5 focuses on the issues associated with FPGA-based control platform, such as the design methodology, hardware description language tools, use of embedded processor cores, on chip interconnections, and FPGA emulation. The software architecture and realization of controller sub-functions in VHDL are described. The means for efficient utilization of the FPGA architecture in the AMB control are developed.

Chapter 6 concludes the main results, summarizes the content and suggests future research work.

1.6 Scientific contribution

In this doctoral thesis (and appended publications), the following main scientific contributions to control design and embedded control implementation can be highlighted:

1. Utilization of the FPGA-based control platform in the outer and inner control loops of the AMB rotor control system. The employment of FPGA for this application enables a design of the single chip controller solution.
2. Building of the custom blocks of digital arithmetic in the FPGAs, which alleviate the AMB controller implementation, in VHDL. The written custom VHDL intellectual properties (IPs) such as state-variable-form realization and nonlinear force field (as a piece-wise interpolation) are general, and can be used in many other embedded control systems.
3. Handling of computationally intensive tasks in a real-time embedded control system, is analyzed, both, in respect of the numerical conditioning of the model-based control models (their discretization, digitization), as well as of their implementation in FPGA.
4. Application of the describing function analysis for predicting the actuator bandwidth. The saturation frequency of the actuator, and bandwidth of the inner current control loop, for different signal amplitudes, are studied (with different methods).
5. Compensation of the actuator force-field nonlinearity by the use of the model reference method and the inverse nonlinearity principle.
6. Formulation of the model-based LQ control, based on physical quantities. The active control of the selected flexible modes, when taking into account their controllability, is achieved.
7. Application of the observer-based unbalance compensation controller with the optimal gains. One variant of the controller can cancel the magnetic force vibrations, and the other variant may cancel the measured displacement vibrations.

Chapter 2

AMB system as a mechatronic product

This chapter presents an overview of the typical AMB rotor system, its main components, their connections, naming conventions and principles of operation. At the end of the chapter, the details of the studied prototyping platform are shown.

2.1 Mechatronic product

Mechatronics is a portmanteau; it fuses above other the mechanical engineering (mecha) and electronic engineering (tronics). Engineering field synergism in mechatronics is depicted in Venn diagram, in Fig. 2.1. As seen from the diagram, the development of AMB application, which is an example of the mechatronic application, requires expertise in many various fields. Another option would be to name the studied system a cybernetic application. However, the definition of cybernetics is more generic, and therefore it is more convenient to use the former term.

The mechatronics stresses the interdisciplinary elements, such as the electromechanical subsystems and control electronics. The software components play a very important role; these are the software tools for computer-aided manufacturing, computer aided design and electronic design automation, and the control software for implementation of a control law and control intelligence. The tools of control engineering, such as modeling and simulation, bind together all other elements in the diagram.

Apart from the Venn diagram, it is practical to depict the physical interconnections between the different subsystems, required engineering fields and the main AMB system parts, as in Fig. 2.2. The mechanical and electrical subsystems are coupled by the magnetic one. This coupling manifests in the electromechanical actuator and proximity sensors. It results from Maxwell's equations that describe the interactions between electric and magnetic fields, and matter, to say, an electric charge is influenced by and produces electromagnetic fields. Electrical engineering deals with control electronics, and along with computer science, it is closely related to modern control engineering. Control engineering focuses on the mathematical modeling of the overall control sys-

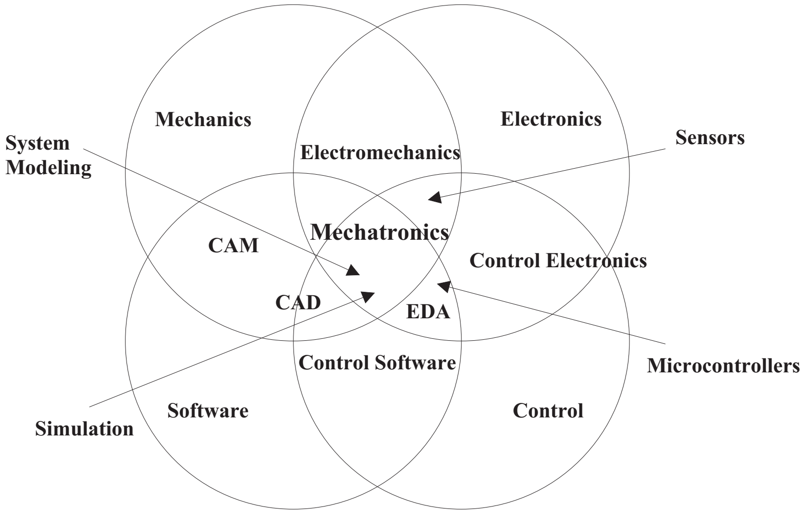

Figure 2.1: Venn diagram of mechatronics

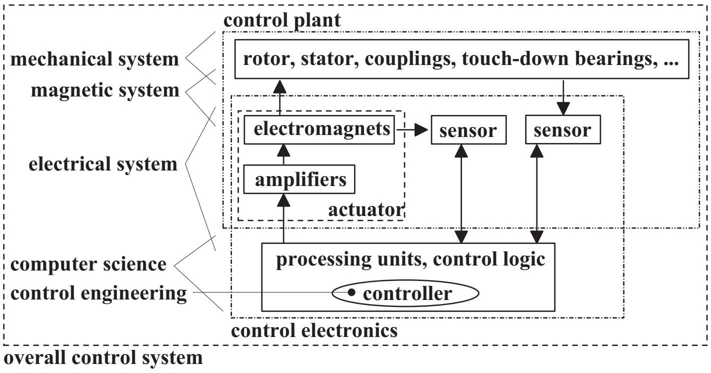

Figure 2.2: Overall AMB control system

tem and the analysis of its dynamic behavior. It uses control theory to build the controller that will cause the control plant to behave in a desired manner. The controller implementation issues are considered by computer (or more appropriately by computing) science, which applies the theoretical foundations of information and computation in the digital control system.

2.2 Mechanical subsystem

In a typical AMB rotor system, the mechanical subsystem consists of a rotor, AMB stators, axial disk, touch-down bearings, and integrated working part, for example, couplings. An AMB rotor consists of a solid steel shaft (a solid iron core made of Fe52 as depicted in Fig. 2.3), a stack of circular laminations pressed onto a sleeve and fitted to the shaft at the radial AMBs, a solid steel disk (may be cut to prevent eddy currents) fitted radially and secured axially at the one end of the shaft for the axial AMB, and a propeller coupling fitted radially and

Figure 2.3: Shaft alone

secured axially at the other end of the shaft. In the absence of an electric motor, a propeller provides the means of rotation. At the shaft, on radial bearings, thin laminations of electric steel are used to provide high magnetic permeability and low eddy current losses. The strength of these laminations with respect to the centrifugal forces limits the achievable peripheral speed to about 200 m/s. The disk at the axial bearing is not laminated. In the disk, the magnetic field is not alternating because of rotation, and therefore the induced eddy currents result from alternating coil currents. Aluminum sleeves form surfaces for the position measurements.

The clearance between the auxiliary bearings and the rotor constitutes the actual operating position range. The connection of the shaft with some other mechanical parts can be accomplished by mechanical couplings at the ends of the shaft. The dimensions of the rotor used in the studied prototype can be found in Appendix B.1.

In general, the radial AMB stator is similar to the one used in electrical motors. It is built from the stack of laminations with slots and electromagnet coils. The axial AMB stator is a solid steel toroidal disk having a C-cross-sectional shape; it hosts a double-acting thrust bearing.

2.3 Actuators

In this study, the actuators comprise the switching amplifiers and the electromagnets. The amplifier converts the control signals, namely control currents, into the electrical currents in the coils. These currents produce the magnetic field in the electromagnet, which in turn produces the magnetic force.

2.3.1 Electromagnets

For multi-degree of freedom suspension system, we use radial and axial AMBs as electromechanical actuators. The radial bearing has a single-piece eight-

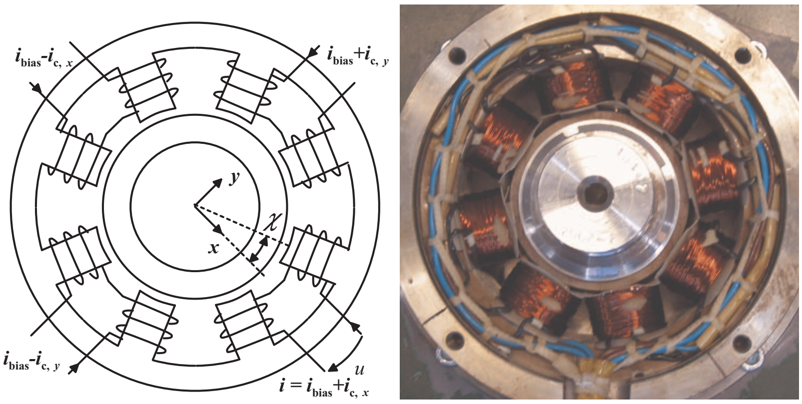

Figure 2.4: Geometry of the studied radial bearing with its coils and currents, where $i_{\mathrm{c},x}$, $i_{\mathrm{c},y}$, i_{bias} and χ are control currents associated with x and y axes, bias current and force acting angle, respectively.

pole stator arranged into four horseshoe electromagnets. They are wound and connected such that we have NSNS configuration and four total coil currents per radial bearing. By using the current biasing, the opposite electromagnets are paired in order to provide two perpendicular force components, specifically in the direction of x and y axes, as in Fig. 2.4 and Fig. 2.5. With such an arrangement, there is, not much flux coupling in the stator, which would result in the force coupling between the x and y directions. As an alternative, an NNSS configuration of the four horseshoe electromagnets would lower rotating losses but increase the force coupling (Antila, 1998), increase the iron saturation, and decrease the maximal attainable magnetic force.

In general, in the bearings with horseshoe electromagnets, the current control is simple, but the minimal load capacity is lower (i.e., less efficient use of iron) compared with the bearings with independently controlled coils. As an illustration, in the eight-pole radial AMB with horseshoe electromagnets, the force (e.g. in x direction) is generated only by the single electromagnet (two poles). However, in the bearings with independently controlled coils, the force is generated by the four electromagnets (four poles). Usually, the increased load capacity is not worth the expense. It requires twice as many power amplifiers as the traditional solution.

In the traditional stator configuration (Fig. 2.4), the control of the forces can be performed with only two control currents $i_{\mathrm{c},x}$, $i_{\mathrm{c},y}$. A constant premagnetization current, also called a bias current $i_{\text{bias}} \leq 0.5 \cdot i_{\max}$ is applied to all of the coils, where the total coil current is $0 \leq i \leq i_{\max}$. The reason for such a control scheme, called a differential driving mode, is a nonlinear relation of the attractive magnetic force with respect to the current and displacement.

The magnetic force phenomena can be explained with the help of Maxwell's equation, namely the currents and changing electric fields produce magnetic fields

$$\nabla \times \mathbf{H} = \mathbf{J} + \frac{\partial \mathbf{D}}{\partial t}, \tag{2.1}$$

where $\mathbf{H}$, $\mathbf{J}$ and $\mathbf{D}$ are the magnetic field strength, current density, and electric

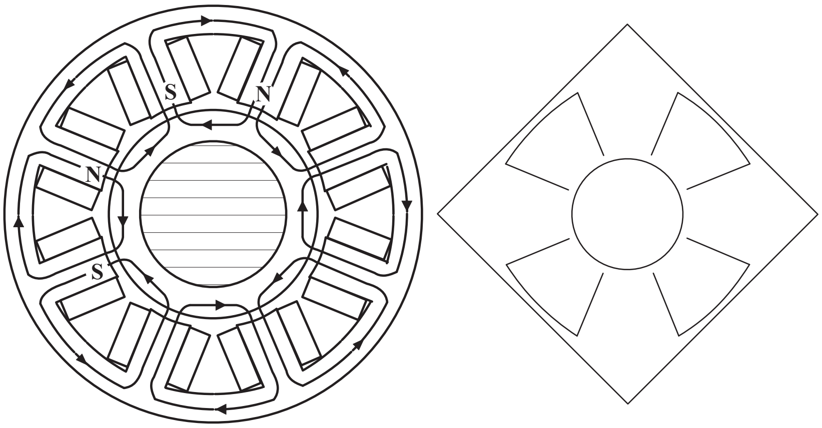

Figure 2.5: On the left, the main flux paths are presented. On the right, the load capacity of the eight-pole radial bearing, with stator arranged into four horseshoe electromagnets (NSNS configuration), is indicated. The tip of maximal force vector forms the perimeter of the rectangle.

flux density. Assuming no time dependence and applying the Kelvin-Stokes theorem, we obtain the integral form of Ampère's Circuital Law

$$\oint_c \mathbf{H} \cdot d\mathbf{l} = \int_S \mathbf{J} \cdot d\mathbf{S}. \tag{2.2}$$

The left-hand side integral of Eq. (2.2) is carried out along the closed flux line c, which defines the circumference of the area S. We consider the magnetic circuit of Fig. 1.1. The flux travels through two media: iron and air, and the flux density $B = \text{const}$ is equal in both media. The magnetic circuit equations are

$$l_{\text{Fe}} H_{\text{Fe}} + 2 l_{\text{air}} H_{\text{air}} = Ni, \tag{2.3}$$

$$l_{\text{Fe}} \frac{B}{\mu_0 \mu_{\text{Fe}}} + 2 l_{\text{air}} \frac{B}{\mu_0} = Ni, \tag{2.4}$$

where l_{Fe}, l_{air}, μ_{Fe} are the average length of flux paths in iron, air, and the relative permeability of iron. Furthermore, assuming $\mu_{\text{Fe}} \gg 1$ the magnetization of iron can be neglected, and the magnetic flux density in the air-gap becomes

$$B = \mu_0 \frac{Ni}{(\frac{l_{\text{Fe}}}{\mu_{\text{Fe}}} + 2 l_{\text{air}})} \approx \mu_0 \frac{Ni}{2 l_{\text{air}}}. \tag{2.5}$$

Now, having the flux density, we can compute the field energy stored in the air-gap. Assuming linear magnetic circuit, the stored magnetic energy W_{fe} and co-energy W_{ce} are equal. For a single horseshoe electromagnet, as in Fig. 1.1, and homogeneous field in the air-gap, the magnetic energy equals

$$W_{\text{ce}} = \int\limits_V \int\limits_0^{\mathbf{H}} \mathbf{B} d\mathbf{H} dV = \int\limits_V \int\limits_0^{\mathbf{B}} \mathbf{H} d\mathbf{B} dV = \frac{1}{2\mu_0} \int\limits_V B^2 dV = \frac{1}{2\mu_0} B^2 S_{\text{air}} 2 l_{\text{air}}, \tag{2.6}$$

where S_{air} is the cross-section area of a stator tooth tip. According to the principle of the virtual work, presented by Krause and Wasynczuk (1989), the force equals the partial derivative of the magnetic co-energy W_{ce} with respect to the virtual displacement l. The derivation of this relation is repeated in Appendix A.1. Using the previous solution for W_{ce}, the magnetic force f can be written as

$$f = \frac{\partial W_{\mathrm{ce}}}{\partial l} = \frac{B^2 S_{\mathrm{air}} \cos\chi}{\mu_0}, \tag{2.7}$$

where, χ is the force acting angle (half the angle between the poles of an electromagnet equals to $\frac{\pi}{8}$). Substituting magnetic flux density (2.5) that neglects the effect of magnetization of iron gives the approximation of the attractive force generated by the single electromagnet

$$f = \frac{\mu_0 N^2 i^2 S_{\mathrm{air}} \cos\chi}{4 l_{\mathrm{air}}^2}. \tag{2.8}$$

The single horseshoe electromagnet generates only attractive force in one direction.

Considering the force that can act in opposite directions along the x or y axis, generated by the pair of two opposite horseshoe electromagnets, yields

$$f_x = f_{1,x} - f_{2,x} = \frac{\mu_0 N^2 S_{\mathrm{air}} \cos\chi}{4} \left(\frac{i_{1,x}^2}{(l_0 - x)^2} - \frac{i_{2,x}^2}{(l_0 + x)^2} \right), \tag{2.9}$$

$$f_y = f_{1,y} - f_{2,y} = \frac{\mu_0 N^2 S_{\mathrm{air}} \cos\chi}{4} \left(\frac{i_{1,y}^2}{(l_0 - y)^2} - \frac{i_{2,y}^2}{(l_0 + y)^2} \right), \tag{2.10}$$

where $(x,\, y)$ represents the coordinates of the rotor center relative to the bearing center, respectively. Bearing in mind the nonlinear, attractive nature of the magnetic force, it is convenient to limit the coil currents i_1, i_2 and introduce a bias linearization, e.g for f_x

$$i_1 = \max(i_{\mathrm{bias}} + i_{\mathrm{c}}, 0), \tag{2.11}$$

$$i_2 = \max(i_{\mathrm{bias}} - i_{\mathrm{c}}, 0), \tag{2.12}$$

$$f_x = \frac{\mu_0 N^2 S_{\mathrm{air}} \cos\chi}{4} \left(\frac{(i_{\mathrm{bias}} + i_{\mathrm{c},x})^2}{(l_0 - x)^2} - \frac{(i_{\mathrm{bias}} - i_{\mathrm{c},x})^2}{(l_0 + x)^2} \right), \tag{2.13}$$

where l_0 and i_{bias} are the nominal air-gap and the bias current, which is equal to or smaller than the half of the maximal coil current ($i_{\mathrm{bias}} \leq 0.5 \cdot i_{\mathrm{max}}$). The force relation, linearized about the operating point ($x = 0$, $i_{\mathrm{c}} = 0$), for two coupled horseshoe electromagnets, becomes

$$f_x = k_i i_{\mathrm{c},x} + k_x x, \tag{2.14}$$

$$k_i = \frac{\partial f}{\partial i_{\mathrm{c}}} \Big|_{x=0,\, i_{\mathrm{c}}=0} = \frac{\mu_0 N^2 S_{\mathrm{air}} i_{\mathrm{bias}} \cos\chi}{l_0^2}, \tag{2.15}$$

$$k_x = \frac{\partial f}{\partial x}\,|_{x=0,\,i_\mathrm{c}=0} = \frac{\mu_0 N^2 S_\mathrm{air} i_\mathrm{bias}^2 \cos\chi}{l_0^3}, \tag{2.16}$$

where k_i and k_x denote the current stiffness (actuator gain) and position stiffness (perceived by a rotor as a negative open-loop stiffness). In addition, the introduced bias linearization provides a larger force slew rate (maximum possible rate of change of a magnetic force), which in the operating point is doubled, in regard to the single magnet. Some authors even suggest to ignore the effect of saturation (Knospe and Collins, 1996), when a high bias current is used. For single electromagnet, the current stiffness and position stiffness (linearized about the operating point) are equal to half of the values computed for two coupled horseshoe electromagnets.

The maximum force, which the single electromagnet can attain is assumed at the saturated silicon iron stator core $B_\mathrm{sat} \approx 1.6$ T, for the rotor remaining in the central position. Assuming the saturation occurring at the saturation current $i_\mathrm{c} + i_\mathrm{bias} = i_\mathrm{sat}$ and using Eq. (2.7), the maximal force in terms of bearing dimensions yields

$$f_\mathrm{max} = \frac{B_\mathrm{sat}^2 S_\mathrm{air} \cos\chi}{\mu_0} \approx L_\mathrm{br} d_\mathrm{r} \cdot 37 \frac{\mathrm{N}}{\mathrm{cm}^2}, \tag{2.17}$$

where $\mu_0 = 4\pi \cdot 10^{-7}\,\mathrm{NA}^{-2}$, L_br and d_r are the bearing core length and the rotor diameter. For the eight-pole actuator, the load capacity varies with direction as shown in Fig. 2.5.

2.3.2 Amplifiers

In the actuator, the coils of the electromagnets are fed by the power amplifiers. The amplifiers operate within the current control scheme, where the control current is biased, as explained earlier, producing the reference current ($i_\mathrm{ref} = i_\mathrm{bias} \pm i_\mathrm{c}$). Then, a total coil current i is generated according to the reference signal by the power circuit using internal current control and current feedback as in Fig. 2.6. There are two types of power amplifiers: linear and switched power amplifiers. In the simple case, the linear amplifier is controlled by the current controller, which is just a proportional gain and the current feedback. Such a linear amplifier produces ripple-free current, but has high power losses. Therefore, almost all applications use switched power amplifiers. With this type of amplifiers, a better efficiency is achieved, but we have to deal with electromagnetic compatibility (EMC) issues. Another, but a small disadvantage of the switching amplifiers is the ripple produced in the current and the remagnetization of the magnetic circuit, which it causes. This ripple decreases with an increased carrier frequency that leads to a shorter switching period.

As the power circuit, we used a three-phase line-frequency diode rectifier to produce a DC link voltage and an H-bridge switching amplifier (depicted in Fig. 2.7) to build the coil current. The switching pattern is produced with carrier-based PWM (two carrier signals) and asymmetric regular sampling (at double carrier frequency) analogically to Holtz (1992) and Zhang and Karrer (1995). This PWM results in the unipolar switching scheme, described by Mohan et al. (1995), where the output voltage changes between positive and zero,

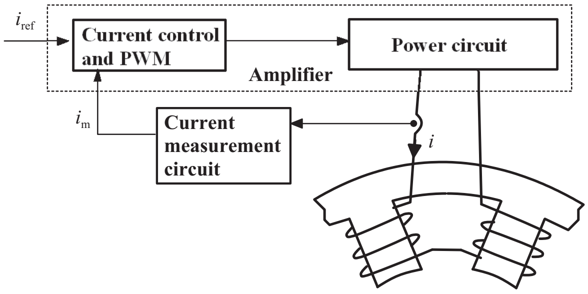

Figure 2.6: Scheme of current amplifier with an radially applied electromagnet

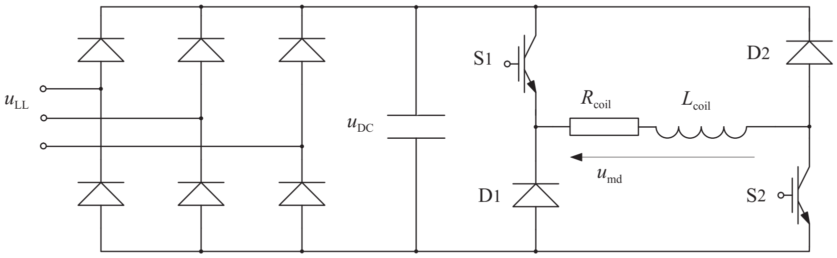

Figure 2.7: Power circuit with H-bridge switching amplifier

or between zero and negative DC link voltage. In detail, the triangle carrier signal u_{tri} (and its inverse) are compared with the reference voltage u_{ref} produced by the local current controller. This results in the following switching patterns for the S1 and S2 transistors of the H-bridge amplifier as in Fig. 2.7:

S1: When $u_{\text{ref}} > u_{\text{tri}}$, the S1 is on.

S2: When $u_{\text{ref}} > -u_{\text{tri}}$, the S2 is on.

The PWM signals and currents resulting from this scheme, when a sinusoidal u_{ref} is applied, are shown in Fig. 2.8 and Fig. 2.9, respectively.

2.4 Sensors

The operation of the amplifier depends on the current control and thus on the quality of the measured current signal in the electromagnet. Similarly the quality of the position control is dependent on the measured position signal. The paired electromagnets are used to exert the magnetic forces on the suspended rotor. For each pair, there are two measured current feedback signals, and one position feedback signal, provided to the inner current and outer position control loops, respectively.

2.4.1 Current transducers

For the current measurements, we used closed-loop (compensated) Hall-effect LEM transducers. The Hall effect was discovered by Edwin Hall in 1879. He described that placing a conductor (in his experiment a thin rectangle of gold)

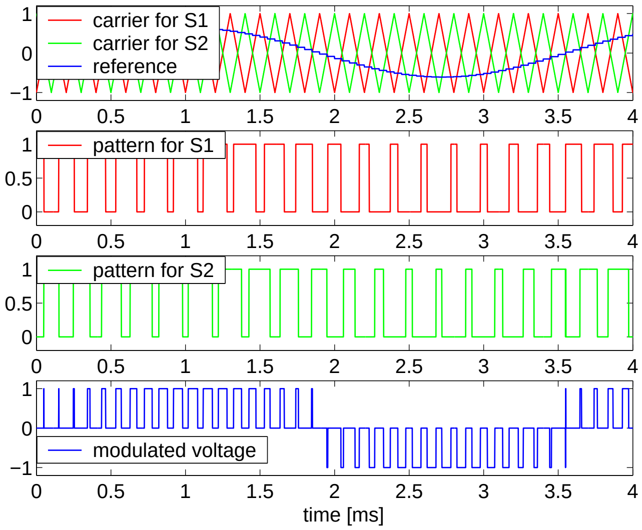

Figure 2.8: PWM signals: carrier for S1 (u_{tri}), carrier for S2 ($-u_{\text{tri}}$), reference (u_{ref}), switching pattern for S1 and S2, modulated voltage (u_{md})

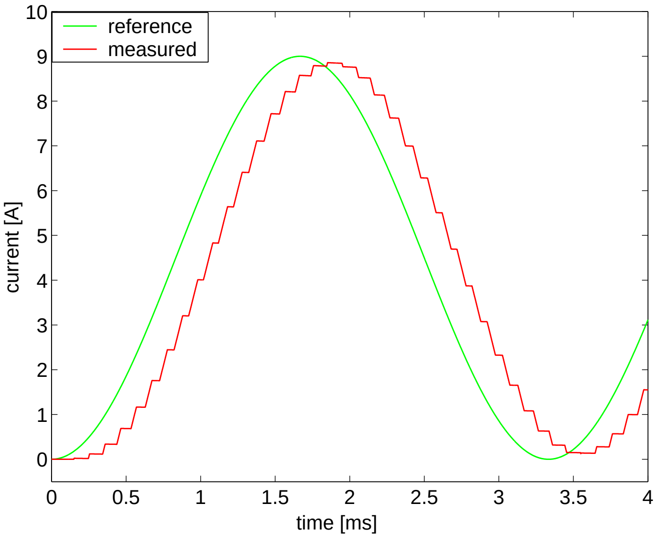

Figure 2.9: Measured and reference currents are depicted. The carrier frequency is equal to 5 kHz, $i_{\text{bias}} = 3\,\text{A}$, and the high gain current controller (control design for $t_{\text{rise}} = 500\mu\text{m}$) are applied.

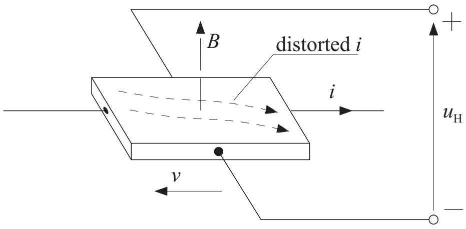

Figure 2.10: Hall sensor – principle of operation

through which a current was flowing into a perpendicular magnetic field, resulted in a voltage generated perpendicular to the current and the field.

In fact, this phenomenon appears because of the Lorentz Force. The Lorentz force vector $\mathbf{f}_\mathrm{L}$ acting on the single carrier electron is

$$\mathbf{f}_\mathrm{L} = q(\mathbf{E} + \mathbf{v} \times \mathbf{B}), \tag{2.18}$$

where q, $\mathbf{E}$, $\mathbf{v}$ are the electron charge, electric field vector and velocity of the particle vector, respectively. In the Hall sensor, the Lorentz Force is exerted on the electrons and disturbs their distribution, as well as current flow, as illustrated in Fig. 2.10. The resulting potential difference across the output of the Hall sensor is called the Hall voltage and it can be expressed as

$$u_\mathrm{H} = \frac{iB}{qnd}, \tag{2.19}$$

where i, n, and d are the current across the plate, the density of the carrier electrons in the conductor, and the material thickness.

The principle of operation of the closed-loop Hall-effect compensated current transducer (Cristaldi et al., 2001) is presented in Fig. 2.11. The transducer consists of a thin plate conductor (a Hall generator) mounted in an air-gap of a magnetic core, a secondary winding wound around the core, and a current amplifier. The measured current called a primary current exerts the circular magnetic field B_p on the magnetic core. The field is proportional to the primary current and is sensed by the Hall generator, which produces the Hall voltage. The voltage is amplified in the amplifier that drives the coil with a secondary current i_sd. The secondary current produces an opposing field B_sd to that provided by the primary one. Thus, the flux in the core is compensated to zero. The relation between the i_p and i_sd is

$$i_\mathrm{p} = N_\mathrm{sd} i_\mathrm{sd}, \tag{2.20}$$

where the N_sd is the number of turns in the secondary winding. The output current is changed into the voltage and scaled by selecting the appropriate shunt resistor R_sd connected between the ground and the coil. The voltage across this resistor is the output signal.

The closed-loop Hall-effect current sensors offer good separation by interfacing between the current, magnetic field and current again. They are characterized by a fast response, a high linearity, and a low temperature drift. Additionally, they are relatively immune to electrical noise. All these properties make them suitable for AMB applications.

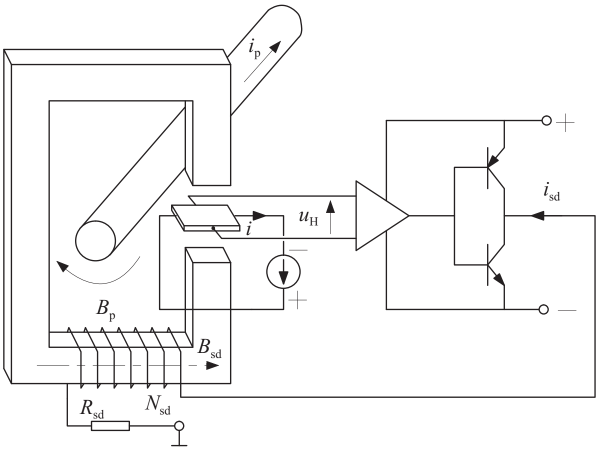

Figure 2.11: Schematic of a closed-loop Hall-effect compensated transducer

2.4.2 Position sensors

In order to provide stable electromagnetic suspension, the controller needs accurate information about the position of the suspended rotor. This position is provided by the position sensors, which have to fulfill specific requirements for the given application; first they have to be contactless in nature, but also require suitable bandwidth, linearity, sensitivity, low susceptibility of noise, appropriate measuring range, and low cost. There is a high variety of position sensors with different operation principles: optical, ultrasonic, Hall effect, capacitive, inductive, and eddy current sensors. In fact, the accurate position sensors can contribute significantly to the overall cost of the magnetic suspension system; therefore they should be carefully selected or custom built (serial production). Based on the survey on sensors by Boehm et al. (1993), it seems that the most versatile type of sensor in the short measuring range is the eddy current transducer. Its main advantages are high resolution combined with a small physical size, temperature stability, small phase shift, and high dc stability. Its main drawback is its high cost.

A typical eddy current sensor system comprises a probe, which contains two coils (an active coil and balance coil), and a driver (driving, demodulating, amplifying, and conditioning electronics). The structure and operation principle of such a sensor type are depicted in Fig. 2.12. In the eddy current sensors, as in the bearings, we can observe the electromagnetic interactions based on Maxwell's equations. Specifically the Maxwell equation in question is the one that expresses Faraday's law of induction

$$\nabla \times \mathbf{E} = -\frac{\partial \mathbf{B}}{\partial t}. \tag{2.21}$$

In the sensor probe a high-frequency alternating current runs through the active coil producing a high-frequency magnetic field. According to Faraday's law, the changes of the magnetic flux density on the surface of the conducting object (a target), in the proximity of the coil, induce rotating electric field. The rotating electric field creates eddy currents in the direction opposite to the coil current, hence the magnetic flux density is reduced and the energy is dissipated. The

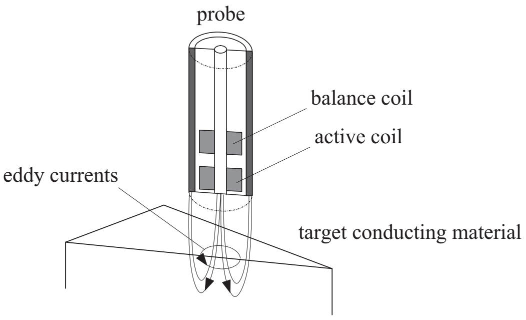

Figure 2.12: Eddy current transducer comprises the probe and driver. The sensors probe consists of the active coil, with the alternating current at a high constant frequency, typically about 1-2 MHz, and the balance coil.

energy dissipation and the amplitude and phase of the oscillating current varies according to the distance of the target to be measured. This current is evaluated electronically in the sensor's driver providing the voltage signal proportional to the measured clearance. The task of the balance coil is to balance the output bridge circuit in the driver and to compensate temperature changes.

The eddy currents are confined to a thin surface layer of the conductor on the rotor. The inhomogeneities on the rotor surface add the noise to the signal and therefore decrease the effective sensitivity of the sensor. The sensitivity also depends on the properties of the measuring surface (i.e., conductivity, permeability) and is higher on aluminum than on steel. The high sensitivity is not enough if it is accompanied by a high susceptibility of noise, caused by power switches. The noise caused by the high-frequency electromagnetic fields of the amplifiers can be neutralized by shielded sensors.

The sensors should be carefully positioned and rigidly mounted. Each sensor can be calibrated for gain and offset; however, it is essential that the measuring range requirements and proper measuring surface are fulfilled. In regard to the measuring range, some extra margin is recommended owing to the previously mentioned effective depth of the eddy currents in the rotor and the sensor's response variations with different target materials.

2.4.3 Analog to digital converters

The analog to digital converters are crucial for reliable operation of the AMB control system. The measured continuous signals, which include currents and positions have to be accurately converted to discrete digital numbers. The input signals to the ADCs, represented by the voltages, contain frequency components above half the sampling rate. To attenuate these components, a low-pass filter (anti-aliasing filter) is placed ahead of the ADC input. A simple single-order filter is feasible for this task. Additionally to the aforementioned measurements, the AMB controller also requires at least two bits from the speed encoder.

2.5 Prototyping platform

In the prototyping platform, we use two radial bearings and one axial bearing, that is, five pairs of electromagnets to control magnetic suspension of the rotor. The technical details and dimensions of the bearings and the rotor used in the studied prototype can be found in Appendix B.1. The total rotor mass is 46.2 kg.

Using Eq. (2.17) and the dimensions of the bearings, the maximal static force load capacity of the radial bearing can be estimated as $f_{\max} \approx 2\,\mathrm{kN}$ (at the nominal air-gap). Alternatively, the more accurate estimate of the maximal bearing load capacity (which still does not resort to the complex numerical solutions) may take into account the magnetization of the iron (Schweitzer et al., 2003). Equation (2.17) defines the load capacity of the studied radial bearing in the weakest direction. It assumes that the maximal radial force occurs at the current i_{sat} that roughly can be determined from (2.5), as

$$i_{\mathrm{sat}} \approx \frac{2 l_0 B_{\mathrm{sat}}}{\mu_0 N} \approx 8.5\,\mathrm{A}, \tag{2.22}$$

where the magnetic air-gap length l_0 is estimated for the rotor remaining in the central position (Appendix B.1). In Eq. (2.22), we assume such a B_{sat} that we still can neglect the effect of iron for the coil current $i < i_{\mathrm{sat}}$ ($i_{\max} > i_{\mathrm{sat}}$). In this work, the maximal current $i_{\max} = 10\,\mathrm{A}$; it is the same for all used types of bearings. In the thrust bearing, the $i_{\max}$ is smaller than the $i_{\mathrm{sat}} \approx 12.7\,\mathrm{A}$. Therefore, it is safe to estimate the load capacity of the axial bearing from Eq. (2.8) as $f_{\max} \approx 2.13\,\mathrm{kN}$. In order to tackle the power losses in the amplifiers, the reduced bias current was pre-selected $i_{\mathrm{bias}} = 0.25 \cdot i_{\max} = 2.5\,\mathrm{A}$. This choice affects the current stiffness k_i and an open-loop gain, which becomes low at a zero load. Additionaly, the possible rate of change of force decreases, compared with the non-reduced i_{bias}. This can be observe by examining Fig. 3.13.

At the beginning of this chapter, the AMB control system as a whole is presented using the mechatronics Venn diagram and general associations with different engineering fields. The physical components of the particular prototyping platform and their physical associations can be presented using the conceptual static model (according to Goma, 2000), which offers a more detailed physical insight to the studied system (Fig. 2.13 and Fig. 2.14).

2.5.1 Control electronics

The main components of the control electronics, apart from the processing units, of the prototyping control system were the following:

1. The custom-built power circuit board, with the IGBT Semitop®2 SK 30 GAR 123 was used. The digital switching signals from the control unit were delivered through the optically isolated gate drivers.
2. For the current sensors we utilized ten closed-loop (compensated) Hall-effect LEM transducers (LA 25-NP).
3. The position sensors, we used three single-channel DT3701 U1-A-C3, two differential (two-channel) DT3703 U3-A-C3 and one single-channel CMSS 68 eddy current displacement sensors from MICRO-EPSILON (used with the radial suspension) and SKF® (2003) (used with the axial suspension),

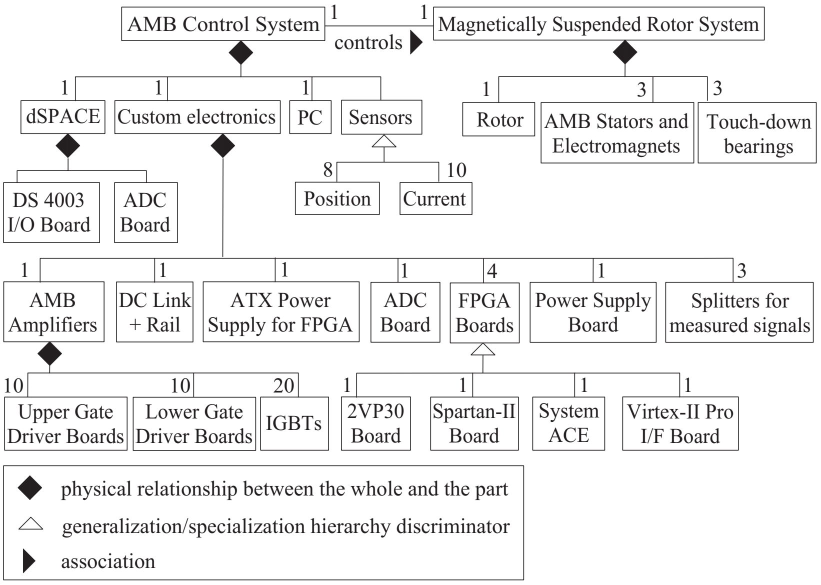

Figure 2.13: Conceptual static model for AMB system, where each number refers to the number of particular entities

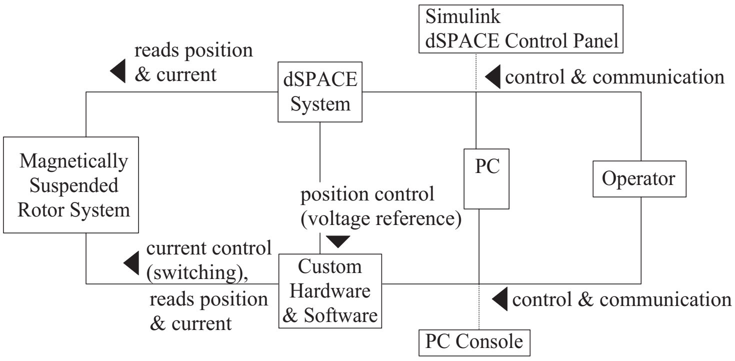

Figure 2.14: Main associations in the static model for AMB system are depicted; the PC Console is as a property of connection between the Custom Hardware & Software block and the PC; the Simulink Control Panel is as a property of connection between the dSPACE and the PC.

respectively. The sensors used for the radial AMBs had aluminum sleeves attached on the steel shaft as the measurement surface, and the sensor for the axial AMB had steel as the measurement surface. The arrangement of the sensors in the prototype, computing the rotor displacements in x and y axes and the calibration of the sensors are summarized in Appendix A.3.

4. The measured signals are split in the signal splitters, and then they are sampled by two sets of ADCs, connected to two control platforms: FPGA-based, and a modular electronic control unit from dSPACE (dSPACE platform). The ADC board that is a part of the dSPACE platform is DS2001, and the ADC board that is a part of the FPGA-based platform is custom-built.

The selected, more detailed characteristics of the control electronics can be found in Appendix B.2.

2.5.2 Processing units

When building the control electronics for the studied system, we were looking for a solution, which would on the one hand provide the powerful and flexible FPGA-based control platform, and on the other hand secure the means to easily test and modify new algorithms. With this in mind, we combined a Memec's development board containing a Xilinx's Virtex-II Pro FPGA with a dSPACE platform that is traditionally used in control development. In such an arranged prototyping platform, the control algorithms can be developed in a graphical Simulink environment, then automatically compiled into the PowerPC processor (in dSPACE) and tested in the system in real-time. The FPGA provides at least a PWM for the gate drivers, or more if it uses its own ADC board. The Memec's development board comprises the Virtex-II Pro FPGA, which contains 30816 logic cells (13696 slices) and two PowerPC 405 (32-bit implementation) embedded processor blocks.

The dSPACE Inc. offers modular, commercial solutions for electronic control unit software development; it is used for rapid control prototyping in a graphical Simulink environment. In particular, we used the DS1005-09 board, from dSPACE, that contains its own PowerPC$^{\text{TM}}$ processor, capable of working in real time. The DS4003 Digital I/O Board (96 TTL I/Os) served as an interface between two control platforms. The selected FPGA contains two embedded 32-bit microprocessor cores, and it enables flexible partitioning of the control software into the programmable hardware and microprocessor program. The development of the control for the FPGA was carried out in VHDL, and the control software development for the dSPACE platform was carried out in the Simulink environment.

Apart from the already listed components, a control electronics featured such components as: host PC, custom-built power distribution board, and a custom-built interface board containing a Spartan$^{\text{TM}}$-II FPGA interface between the Virtex-II FPGA and DS4003 board from dSPACE.

The components of the control electronics and the Memec's FPGA board are presented in Fig. 2.15.

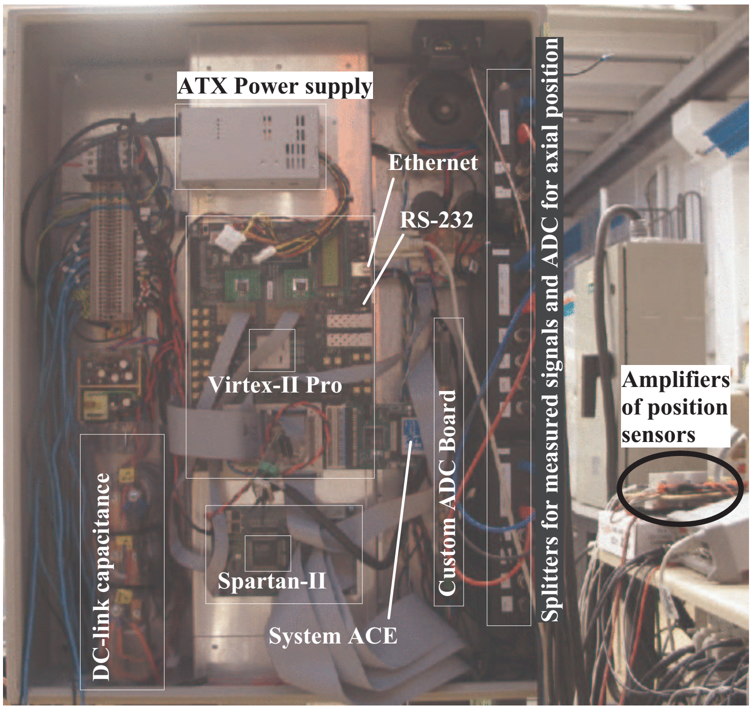

Figure 2.15: Custom-built components of the control electronics and the Memec's FPGA board are mounted in a single box.

2.6 Summary

In this chapter, the principles of operation and components of a typical AMB system were presented. We can point out that the interrelationships in electromagnetism described by Maxwell's equations are behind the principles of generating magnetic force, eddy-current displacement sensors, and Hall-effect current transducers. The knowledge necessary for building a successful control for AMB rotor system comes from different fields of engineering, constituting a complex and challenging control problem. The control platform built and used for the purposes of this study was presented. In this work, we were not granted the comfort of the ready prototype, and instead we were restricted to an ad hoc custom modular design. Hence, the prototyping platform cannot be regarded as a single-chip, FPGA-based solution; however, this study can be, de facto, used as a basis for such an integration.

The integration of the processing units into a single chip is possible even for complex and sophisticated controllers, when the large FPGA devices are considered. The FPGA with embedded floating-point DSP and embedded microprocessor cores may host all the necessary control, including drivers for the sensors, ADCs, actuators, and user interfaces. Thus EMC problems caused by switching devices do not disturb interchip or interboard communication. Such a one-board, one-chip solution makes possible a decrease in cost, and space.

As for the widely understood reliability issues, which include EMC and debugging capabilities, they are not considered in detail, in this work, but can be found, for example, in the works of Wassermann et al. (2003), Schulz et al. (2006), and in Publication VI, respectively.

Chapter 3

AMB system modeling

Before formulating the appropriate controller for the AMB rotor system, we have to build a suitable system model. First, the components of the system: the rotor, sensors with low-pass filters, and amplifiers are modeled. Then, the overall model of the system is formed using the standard state-space representation. The chapter also contains a brief introduction to the very basics of rotor discretization methods and modeling of the electromechanical characteristics of AMB.

3.1 Rigid rotor

As mentioned in the introduction, we may use different strategies when designing the controller. Whether we need a more or less accurate plant model for the controller synthesis is determined by the centralized or decentralized control strategy. Whatever the controller, it requires verification by simulations with an even more detailed plant model.

In the simplest case, we can model the rotor as two point masses, at the locations of two radial bearings. We recall Newton's Second Law written as a differential equation $\mathbf{f} = d(m\mathbf{v})/dt$, that is, the net force on a point mass is proportional to the rate of change of its linear momentum in time. Assuming the constant mass and the linear transfer function of a magnetic bearing (2.14), the net bearing force acting in the x direction becomes

$$f = m\ddot{x} = k_i i_{\mathrm{c}} + k_x x. \tag{3.1}$$

In this way, when describing the suspension in z direction, the 1-DOF axially suspended rotor model is formed. When a radial suspension in x and y directions is considered, the use of Eq. (3.1) results in the rotor model described by four independent 1-DOF equations. A slightly more complex alternative solution is a 2-DOF model that introduces the coupling of transversal motion of the center of gravity with tilting motion.

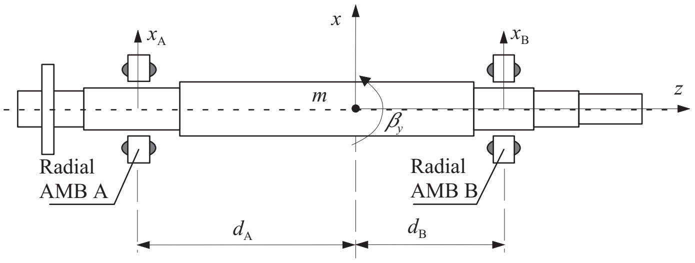

Figure 3.1: Rigid rotor can be modeled using a 2-DOF model, where d_A and d_B mark the locations of the radial bearings measured in z direction.

3.1.1 Rigid rotor 2-DOF model

For the rigid rotors with a relatively weak gyroscopic effect[1], we can model the symmetrical rotor using the 2-DOF model as presented in Fig. 3.1. The model can be described using two state variables x and β_y, which represent the transversal motion and tilting motion (about y axis) of the rotor, in a (x, z) plane. The model in the matrix notation is

$$\boldsymbol{M}\ddot{\mathbf{x}} = \mathbf{f} = \boldsymbol{T}_1\boldsymbol{K}_x\mathbf{x}_\mathrm{b} + \boldsymbol{T}_1\boldsymbol{K}_i\mathbf{i}_\mathrm{c}, \tag{3.2}$$

$$\boldsymbol{M} = \begin{bmatrix} m & 0 \\ 0 & I_y \end{bmatrix}, \boldsymbol{K}_x = \begin{bmatrix} k_x & 0 \\ 0 & k_x \end{bmatrix}, \boldsymbol{K}_i = \begin{bmatrix} k_i & 0 \\ 0 & k_i \end{bmatrix}, \tag{3.3}$$

$$\mathbf{x} = \begin{bmatrix} x \\ \beta_y \end{bmatrix}, \mathbf{x}_\mathrm{b} = \begin{bmatrix} x_\mathrm{A} \\ x_\mathrm{B} \end{bmatrix}, \mathbf{i}_\mathrm{c} = \begin{bmatrix} i_\mathrm{c,A} \\ i_\mathrm{c,B} \end{bmatrix}, \boldsymbol{T}_1 = \begin{bmatrix} 1 & 1 \\ d_\mathrm{A} & d_\mathrm{B} \end{bmatrix}, \tag{3.4}$$

where the I_y, $\boldsymbol{T}_1$, d_A and d_B represent the transversal moment of inertia about the y axis, the transformation of the forces generated by the bearings to the center of gravity $\mathbf{f} = \boldsymbol{T}_1\mathbf{f}_\mathrm{b}$ and the locations of the radial bearings measured in the z direction (distance d_A is negative), respectively. The $\boldsymbol{M}$, $\boldsymbol{K}_x$ and $\boldsymbol{K}_i$ denote the mass matrix, position stiffness matrix and current stiffness matrix, respectively. The currents $i_\mathrm{c,A}$ and $i_\mathrm{c,B}$ refer to the electromagnets, which exert the forces acting in the (x, z) plane. The subscripts A and B refer to the different rotor ends as explained in Fig. 3.1. In Eq. (3.2), the generalized force vector $\mathbf{f}$ represents the bearing forces (the force in the x direction and torque in the y direction). In a general case, it denotes the sum of the bearing forces, load forces and disturbance forces.

In order to simplify the force calculation, it is practical to use the currents and displacements related to the bearings $i_\mathrm{c,A}$, $i_\mathrm{c,B}$, x_A, x_B instead of variables related to the center of gravity x, β_y. The system transformed to the bearing coordinates yields

$$\boldsymbol{M}_\mathrm{b}\ddot{\mathbf{x}}_\mathrm{b} = \mathbf{f}_\mathrm{b} = \boldsymbol{K}_x\mathbf{x}_\mathrm{b} + \boldsymbol{K}_i\mathbf{i}_\mathrm{c}, \tag{3.5}$$

---

[1] If $I_z/I_x > 1$ the rotor is usually referred to as highly gyroscopic rotor (disk). If $I_z/I_x < 1$ the rotor is referred to as a long rotor; and for the rotors with $I_z/I_x \ll 1$, the gyroscopic effect can be very weak. The moments I_z and I_x are rotational moment of inertia (polar moment of inertia) and transversal moment of inertia (equatorial moment of inertia), respectively.

$$\boldsymbol{M}_{\mathrm{b}} = \boldsymbol{T}_2^{\mathrm{T}} \boldsymbol{M} \boldsymbol{T}_2,\ \boldsymbol{T}_2^{\mathrm{T}} = \boldsymbol{T}_1^{-1}, \tag{3.6}$$

where matrix $\boldsymbol{T}_2$ is invertible and it enables the transformation of the bearing variables to the variables related to the center of gravity $\boldsymbol{x} = \boldsymbol{T}_2 \mathbf{x}_{\mathrm{b}}$. This relation is called a congruent transformation (equivalence relation[2]), and the real matrices $\boldsymbol{M}$ and $\boldsymbol{M}_{\mathrm{b}}$ are called congruent matrices. The transformation matrix $\boldsymbol{T}_1$ is obtained by assuming small values for β_x and β_y.

In this model, the (x, z) and (y, z) planes can be considered individually and the rotor is described with two uncoupled 2-DOF equations (3.5). Going still somewhat further with the complexity of the model, we can add a gyroscopic coupling between the two planes.

3.1.2 Rigid rotor 4-DOF model

The gyroscopic effect should be considered when the rotors, with high rotational speed or substantial I_z/I_x ratio, are modeled. For the radial suspension and the variables $\mathbf{x} = [x,\ \beta_y,\ y,\ -\beta_x]^{\mathrm{T}}$ in the 4-DOF model of the symmetrical disk, the equations of motion can be written as

$$\boldsymbol{M}\ddot{\mathbf{x}} + \Omega \boldsymbol{G} \dot{\mathbf{x}} = \mathbf{f}. \tag{3.7}$$

Now, the mass matrix $\boldsymbol{M}$, the gyroscopic matrix $\boldsymbol{G}$, and the generalized force vector $\mathbf{f}$ applied at the center of gravity are

$$\boldsymbol{M} = \begin{bmatrix} m & 0 & 0 & 0 \\ 0 & I_y & 0 & 0 \\ 0 & 0 & m & 0 \\ 0 & 0 & 0 & I_x \end{bmatrix},\ \boldsymbol{G} = \begin{bmatrix} 0 & 0 & 0 & 0 \\ 0 & 0 & 0 & 1 \\ 0 & 0 & 0 & 0 \\ 0 & -1 & 0 & 0 \end{bmatrix} I_z,\ \mathbf{f} = \begin{bmatrix} f_x \\ \Theta_y \\ f_y \\ -\Theta_x \end{bmatrix}, \tag{3.8}$$

where the Ω, I_z and Θ denote the rotational speed, the rotational moment of inertia about the z axis, and the torque (moment about x or y axes), as in Fig. 3.2. Because of the assumed rotational symmetry of the rotor body $I_x = I_y$. In the 4-DOF model, the (x, z) and (y, z) planes are coupled by the $\boldsymbol{G}$ matrix. For example, the torque applied perpendicular to the axis of rotation (i.e., z axis), and for that reason to the angular momentum $\mathbf{L}_{\mathrm{a},z} = I_z \Omega$, results in a angular velocity perpendicular to both. This angular velocity is given by the cross product $\boldsymbol{\Theta} = (\dot{\beta}) \times \mathbf{L}_{\mathrm{a},z}$. As an illustration, in Fig. 3.3, the torque $\boldsymbol{\Theta}_x$ is applied to the rotor. A non-rotating rotor would only turn about x axis. If a rotor is spinning (with an angular speed Ω), the longitudinal axis of the rotor (defined by the direction between end-A and end-B) moves into the direction of the overturning moment $\boldsymbol{\Theta}_x$. Hence, the rotor also turns about y axis.

Similarly to the 2-DOF, the 4-DOF system transformed to the bearing coordinates yields

$$\boldsymbol{M}_{\mathrm{b}} \ddot{\mathbf{x}}_{\mathrm{b}} + \boldsymbol{G}_{\mathrm{b}} \dot{\mathbf{x}}_{\mathrm{b}} = \mathbf{f}_{\mathrm{b}}, \tag{3.9}$$

$$\boldsymbol{M}_{\mathrm{b}} = \boldsymbol{T}_2^{\mathrm{T}} \boldsymbol{M} \boldsymbol{T}_2,\ \boldsymbol{G}_{\mathrm{b}} = \boldsymbol{T}_2^{\mathrm{T}} \boldsymbol{G} \boldsymbol{T}_2, \tag{3.10}$$

---

[2] A congruence relation may change the eigenvalues of a matrix but it cannot change the signs of the eigenvalues

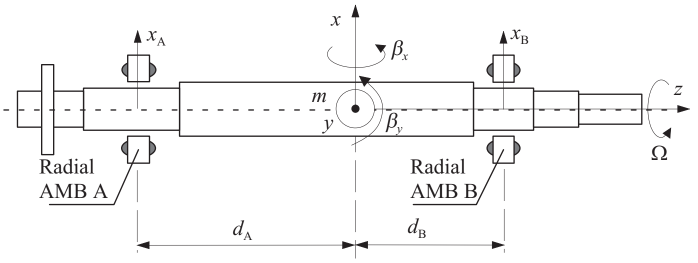

Figure 3.2: Rigid rotor can be modeled using 4-DOF model, where the $(x,\ z)$ and $(y,\ z)$ planes are coupled by the gyroscopic effect.

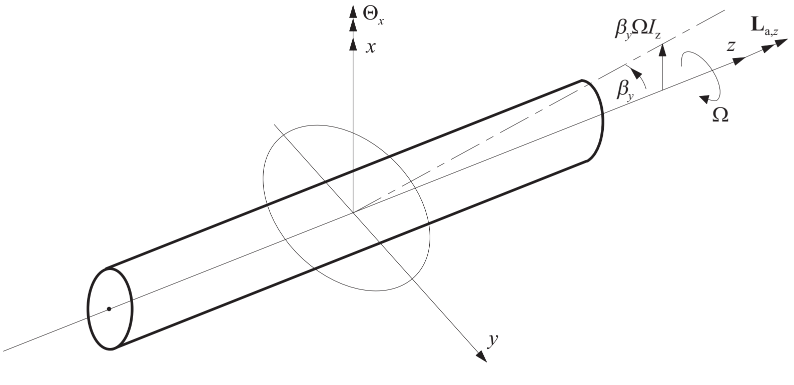

Figure 3.3: Angular moment in spinning rotor $\boldsymbol{\Theta}_x = d\mathbf{L}_{\mathrm{a},x}/dt$, where for small angular displacement β_y the angular momentum $\mathrm{L}_{\mathrm{a},x} = I_x\dot{\beta}_x + I_z\Omega\beta_y$.

where the bearing variables now are $\mathbf{x}_\mathrm{b} = [x_\mathrm{A},\ x_\mathrm{B},\ y_\mathrm{A},\ y_\mathrm{B}]^\mathrm{T}$, the control currents are $\mathbf{i}_\mathrm{c} = [i_{\mathrm{c},x,\mathrm{A}},\ i_{\mathrm{c},x,\mathrm{B}},\ i_{\mathrm{c},y,\mathrm{A}},\ i_{\mathrm{c},y,\mathrm{B}}]^\mathrm{T}$ and the transformation matrix $\boldsymbol{T}_2$ is

$$\boldsymbol{T}_2 = \frac{1}{d_\mathrm{B} - d_\mathrm{A}} \begin{bmatrix} d_\mathrm{B} & -d_\mathrm{A} & 0 & 0 \\ -1 & 1 & 0 & 0 \\ 0 & 0 & d_\mathrm{B} & -d_\mathrm{A} \\ 0 & 0 & -1 & 1 \end{bmatrix}. \tag{3.11}$$

3.2 Flexible rotor

In practice, flexible rotors require more complex models and are approximated by higher-order multi-degree of freedom (MDOF) models. The continuous flexible structure can be approximated as an MDOF discrete system using different discretization principles. Before describing the flexible rotor model used in this work, a brief general introduction to the discretization process itself and the model construction is given. A more comprehensive treatment of the dynamics of rotating systems, discretization, and FEM methods are presented by Genta (2005), Chen and Gunter (2005) and also by Yamamoto and Ishida (2001).

3.2.1 Discretization techniques

According to Genta (2005), three different classes of the discretization techniques can be distinguished. The first class of the discretization techniques comprises assumed mode methods. These methods assume that the deflected shape of a continuous elastic body is a linear combination of M arbitrary mode shape functions $\boldsymbol{\phi}_k(\mathbf{x})$ (for $k \in [1,\ M]$) of the space coordinates $\mathbf{x}$. As an example, the deflection $\mathbf{y}_j$ of a specific point of the body (in the undeformed body the point $\mathbf{x}_j \in V$, where the V is the spatial volume occupied by the body) at time t can be expressed in terms of the assumed $\boldsymbol{\phi}_k(\mathbf{x}_j)$ and modal amplitudes $\eta_k(t)$ as

$$\mathbf{y}_j(\mathbf{x}_j, t) = \sum_{k=1}^{M} \boldsymbol{\phi}_k(\mathbf{x}_j)\eta_k(t), \tag{3.12}$$

where η_k can be considered as the modal coordinates. Furthermore, we assume that the displacement of the structure is measured at the P discrete points (nodes) $\mathbf{x} = \mathbf{x}_j$ (for $j \in [1,\ P]$) and therefore the measurement vector field is

$$\mathbf{y}^\mathrm{T} = \begin{bmatrix} \sum_{k=1}^{M} \boldsymbol{\phi}_k(\mathbf{x}_1)\eta_k(t) & ... & \sum_{k=1}^{M} \boldsymbol{\phi}_k(\mathbf{x}_P)\eta_k(t) \end{bmatrix}. \tag{3.13}$$

In the matrix notation, Eq. (3.13) can be expressed as

$$\mathbf{y} = \boldsymbol{\Phi}\boldsymbol{\eta}, \tag{3.14}$$

where

$$\boldsymbol{\Phi} = \begin{bmatrix} \boldsymbol{\phi}_1(\mathbf{x}_1) & \cdots & \boldsymbol{\phi}_M(\mathbf{x}_1) \\ \vdots & \ddots & \vdots \\ \boldsymbol{\phi}_1(\mathbf{x}_P) & \cdots & \boldsymbol{\phi}_M(\mathbf{x}_P) \end{bmatrix},\ \boldsymbol{\eta} = \begin{bmatrix} \eta_1 \\ \vdots \\ \eta_M \end{bmatrix}. \tag{3.15}$$

From the obtained displacement field, the expressions of the kinetic, potential, and dissipation energies can be obtained. The total kinetic energy of the system (with the positive and definite mass matrix, that is, for instance, for real symmetric matrix $\boldsymbol{M}$ and for all non-zero real vectors $\dot{\boldsymbol{\eta}}$, $\dot{\boldsymbol{\eta}}^{\mathrm{T}} \boldsymbol{M} \dot{\boldsymbol{\eta}} > 0$) is expressed in terms of the generalized coordinates $\boldsymbol{\eta}$ and generalized velocities $\dot{\boldsymbol{\eta}}$ as $W_{\mathrm{T}} = W_{\mathrm{T}} \left(\boldsymbol{\eta}, \dot{\boldsymbol{\eta}}\right)$. The potential energy is expressed in terms of the generalized coordinates only $W_{\mathrm{V}} = W_{\mathrm{V}} \left(\boldsymbol{\eta}\right)$ and the dissipation energy depends on the generalized velocities only $W_{\mathrm{P}} = W_{\mathrm{P}} \left(\dot{\boldsymbol{\eta}}\right)$. In general, for our purposes, these expressions can be expressed as

$$W_{\mathrm{T}} = \frac{1}{2} \dot{\boldsymbol{\eta}}^{\mathrm{T}} \boldsymbol{M} \dot{\boldsymbol{\eta}},\ W_{\mathrm{V}} = \frac{1}{2} \boldsymbol{\eta}^{\mathrm{T}} \boldsymbol{K}_{\mathrm{M}} \boldsymbol{\eta},\ W_{\mathrm{P}} = \frac{1}{2} \dot{\boldsymbol{\eta}}^{\mathrm{T}} \boldsymbol{C}_{\mathrm{M}} \dot{\boldsymbol{\eta}}, \tag{3.16}$$

where $\boldsymbol{K}_{\mathrm{M}}$ and $\boldsymbol{C}_{\mathrm{M}}$ are the general stiffness matrix and general damping matrix that consists of a skew-symmetric gyroscopic matrix $\boldsymbol{G}$ ($\boldsymbol{G}^{\mathrm{T}} = -\boldsymbol{G}$) and a symmetric damping matrix $\boldsymbol{D}_{\mathrm{M}}$. The $\boldsymbol{M}$, $\boldsymbol{K}_{\mathrm{M}}$ and $\boldsymbol{C}_{\mathrm{M}}$ are of order M and they depend on the inertial and elastic properties of the system. Now, the equations of motion can be computed using Lagrange's equation. Lagrange's equation for a particular DOF (associated with the η_k) can be written

$$\frac{d}{dt} \left(\frac{\partial W_{\mathrm{T}}}{\partial \dot{\eta}_k} \right) - \frac{\partial W_{\mathrm{T}}}{\partial \eta_k} + \frac{\partial W_{\mathrm{P}}}{\partial \dot{\eta}_k} + \frac{\partial W_{\mathrm{V}}}{\partial \eta_k} = f_k, \tag{3.17}$$

where

$$f_k = \sum_{j=1}^{P} f_j \boldsymbol{\phi}_k(\mathbf{x}_j) \tag{3.18}$$

is the modal force equal to the sum of the discrete force components f_j applied at each node ($\mathbf{x}_j$). The equations of motion, in modal coordinates $\boldsymbol{\eta}$, derived from Lagrange's equations for the rotational speed Ω can be written in the matrix form

$$\boldsymbol{M} \ddot{\boldsymbol{\eta}} + \left(\boldsymbol{D}_{\mathrm{M}} + \Omega \boldsymbol{G} \right) \dot{\boldsymbol{\eta}} + \boldsymbol{K}_{\mathrm{M}} \boldsymbol{\eta} = \mathbf{f}. \tag{3.19}$$

The second group of the discretization techniques are lumped-parameter methods. In these methods, the physical structure is divided into a number of rigid bodies connected by massless fields that possess the elastic and damping properties. Here, the generalized coordinates are defined by the displacements of the rigid bodies. Furthermore, using the same application of Newton's Second Law as for the 1-DOF model, we can compose a M-DOF model. The $\boldsymbol{M}$ and $\mathbf{f}$ are written directly using the engineering judgment. However, for complex structures, obtaining the $\boldsymbol{K}_{\mathrm{M}}$ matrix is difficult. Therefore, the lumped-parameter methods often resort to finite element methods (FEMs) to compute the stiffness matrix.

The third most versatile class of the discretization techniques are FEMs (also assumed modes are usually derived using FEM), which are based on the subdivision of the structure into finite elements. Each element has its own set of DOF associated with the discrete nodes. Inside each element, similarly as in the assumed mode method, the displacement $\mathbf{w}(\mathbf{x}, t)$ is approximated by the usually linear combination of the shape functions (Eq. 3.13), where $\boldsymbol{\eta}$ are now the generalized coordinates of the particular element. The shape functions $\boldsymbol{\phi}_k$ are arbitrary but must satisfy a number of conditions, particularly to be continuous and derivable, and they have to match the shape of the neighboring elements. The neighboring elements share the nodes placed at the side of the elements. For each element, the equations of motion can be written analogically as for the assumed modes method. Next, the complete set of equations has to be assembled. In the case of the rotor modeling, the disk and beam elements can be used; if their reference frames coincide with the global reference frame, no coordinate transformations from the local to the global reference frames are required. Now, the generalized coordinate vector $\boldsymbol{\eta}^{\mathrm{g}}$ contains all the coordinates of various elements and the global $\boldsymbol{M}^{\mathrm{g}}$, $\boldsymbol{K}_{\mathrm{M}}^{\mathrm{g}}$ and $\boldsymbol{C}_{\mathrm{M}}^{\mathrm{g}}$ are formed by adding each term of the matrices of all finite elements in the correct place.

3.2.2 Flexible rotor model

In this work, the continuous elastic rotor and the laminations are modeled using the beam finite elements, which are based on the Timoshenko beams, and the rigid disks. For both elements, the analysis focuses on the lateral vibrations, and therefore the axial and torsional degrees of freedom are not considered.

The rigid disks are prismatic (properties of all cross sections are equal), homogeneous, straight, and untwisted (the principal axes of elasticity are equally directed in space). Each disk assumes a lumped mass matrix, comprises four DOF, and is analogous to the 4-DOF rotor model described in subsection 3.1.2. However, in order to unify the description of all the elements, the vector of the nodal displacements, the generalized coordinates of the only node of the element, is $\boldsymbol{\eta} = [x, y, \beta_x, \beta_y]^{\mathrm{T}}$ and the $\boldsymbol{M}$, $\boldsymbol{G}$, $\mathbf{f}$ are modified appropriately as

$$\boldsymbol{M} = \begin{bmatrix} m & 0 & 0 & 0 \\ 0 & m & 0 & 0 \\ 0 & 0 & I_x & 0 \\ 0 & 0 & 0 & I_y \end{bmatrix}, \boldsymbol{G} = \begin{bmatrix} 0 & 0 & 0 & 0 \\ 0 & 0 & 0 & 0 \\ 0 & 0 & 0 & 1 \\ 0 & 0 & -1 & 0 \end{bmatrix} I_z, \mathbf{f} = \begin{bmatrix} f_x \\ f_y \\ \Theta_x \\ \Theta_y \end{bmatrix}. \tag{3.20}$$

The beam elements are prismatic and homogeneous beams, as presented in Fig. 3.4, that account for the shear deformation in the beam element transverse (radial) direction. Specifically, in the approach used the shear effect is included in the shape functions (Chen and Gunter, 2005). Each beam element has two nodes located at the ends of the beam, and each node has four DOF. The vector of the generalized coordinates of the element, is

$$\boldsymbol{\eta} = [x_1, y_1, \beta_{x,1}, \beta_{y,1}, x_2, y_2, \beta_{x,2}, \beta_{y,2}]^{\mathrm{T}}. \tag{3.21}$$

It describes the time-dependent displacements of the end-points of the finite shaft element. With this definition, the generalized displacement of an internal point of the element placed on the z axis (center line) can be expressed by interpolation, using Eq. (3.13) as

$$\begin{bmatrix} x(z, t) \\ y(z, t) \\ \beta_x(z, t) \\ \beta_y(z, t) \end{bmatrix} = \boldsymbol{\Phi}(z)\boldsymbol{\eta}(t), \tag{3.22}$$

where the shape function matrix $\boldsymbol{\Phi}$ consists of translational and rotational interpolation shape functions of the Timoshenko beam. Each column of the $\boldsymbol{\Phi}$

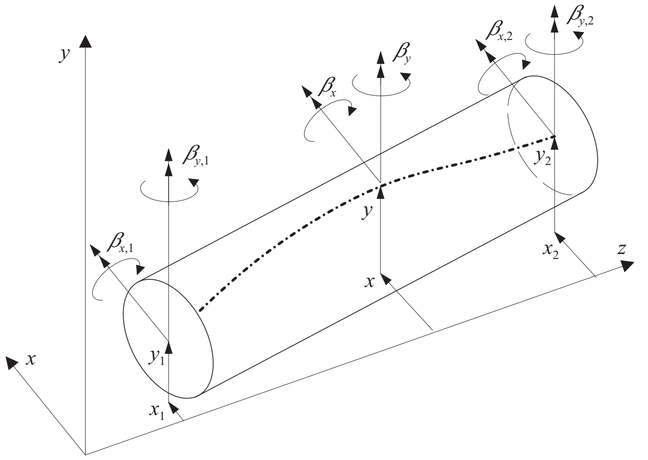

Figure 3.4: Beam element and coordinates

is an individual shape function vector, which represents the mode associated with a unit displacement of one of the coordinates of one of the nodes. Utilizing the derivations from the literature, the shape functions and energies can be computed, according to Chen and Gunter (2005), for each finite element. Then, as stated earlier, the equations of motion for the particular elements can be computed, and after that, the equations of motion for the complete system are assembled.

In the complete system, we may assume only the displacement at the nodes. The complete system is expressed in the global coordinate system; now a new displacement vector has all the node displacements of all the elements as its components, namely for P nodes, each with the local j-th displacement vectors $\boldsymbol{\eta}_j$, the global displacement vector is $\boldsymbol{\eta}^{\mathrm{g}} = \left[\begin{array}{ccc} \boldsymbol{\eta}_1 & \dots & \boldsymbol{\eta}_P \end{array} \right]^{\mathrm{T}}$. Such a straightforward transformation is possible because the displacements in the corresponding axes in the local and global systems have the same magnitudes and directions. The complete rotor system is described by

$$\boldsymbol{M}^{\mathrm{g}}\ddot{\boldsymbol{\eta}}^{\mathrm{g}} + \left(\boldsymbol{D}^{\mathrm{g}}_{\mathrm{M}} + \Omega\boldsymbol{G}^{\mathrm{g}}\right)\dot{\boldsymbol{\eta}}^{\mathrm{g}} + \boldsymbol{K}^{\mathrm{g}}\boldsymbol{\eta}^{\mathrm{g}} = \mathbf{f}^{\mathrm{g}}, \tag{3.23}$$

where the global mass, damping, gyroscopic and stiffness matrices are obtained as explained earlier. Equation (3.23) features many DOF, it is coupled and thus not practical for control engineering purposes.

3.2.3 Reduction of the number of degrees of freedom

In practical control problems, only a limited number of degrees of freedom is usually required. The number of DOF in the derived model can be reduced by modal decomposition and then truncation of high-frequency modes. In the case of the symmetric positive definite matrices, the method leads to an uncoupled system in the familiar form of Eq. (3.13), where the measurement vector represents the physical coordinates. In other words, the center-line of the rotor, determined by the aforementioned measurement vector, is a linear combination of the mode shape functions, weighted by the modal weights. The principle of the method is as follows.

First, the M (where M equals to the number of DOF) independent normal mode shape functions (eigenvectors) and corresponding critical speeds (eigenvalues) are obtained by solving the M-DOF eigenvalue problem. We assume the free-free vibrations of the undamped system (Eq. 3.23), which is considered for $\Omega = 0$. The critical speeds of the system, at which the self-excited vibrations occur, can be found by solving the following generalized eigenvalue problem

$$\left[\boldsymbol{K}^{\mathrm{g}} - \omega_k^2 \boldsymbol{M}^{\mathrm{g}}\right] \boldsymbol{\phi}_k^{\mathrm{m}} = 0, \tag{3.24}$$

where ω_k, $\boldsymbol{\phi}_k^{\mathrm{m}}$ are M critical speeds and corresponding mode shape functions, respectively. The system's self-excited vibrations are equal to the superposition of the global displacements as

$$\eta_k^{\mathrm{g}}(t) = \boldsymbol{\phi}_k^{\mathrm{m}} \cdot \cos(\omega_k t + \varsigma_k), \tag{3.25}$$

where ς_k is the arbitrary phase angle. In physical systems, the matrix $\boldsymbol{K}^{\mathrm{g}}$ is symmetric, real, and positive semidefinite (all of whose eigenvalues are non-negative). The matrix $\boldsymbol{M}^{\mathrm{g}}$ is symmetric, real, and positive definite. Therefore, critical speeds and mode shape functions are real. Furthermore, mode shape functions, which correspond to different critical speeds are orthogonal. In control engineering, it is a common practice to obtain an orthonormal set of eigenvectors (orthogonal and with unit length) for the mass-weighted stiffness matrix (mass matrix becomes identity matrix). This may offer certain advantages in control engineering, albeit the physical meaning of parameters and variables is lost. Here we use a different procedure.

Second, in order to preserve the physical meaning of the system's parameters and variables we follow Lantto (1997), and we define the matrix of the mode shape functions as consisting of the rigid body mode and flexible mode shape functions as $\boldsymbol{\Phi}^{\mathrm{m}} = \left[\boldsymbol{\Phi}^{\mathrm{m}}_{\mathrm{rigid}}, \boldsymbol{\Phi}^{\mathrm{m}}_{\mathrm{flex}}\right]$. The order of the system is reduced by using the $\boldsymbol{\Phi}^{\mathrm{m}}_{\mathrm{flex}}$ that consists of the mode shape functions $\boldsymbol{\phi}_k^{\mathrm{m}}$, arranged in the matrix according to the ascending critical speeds ω_k, and then truncated. In $\boldsymbol{\Phi}^{\mathrm{m}}_{\mathrm{flex}} = \left[\begin{array}{ccc} \boldsymbol{\phi}_5^{\mathrm{m}} & ... & \boldsymbol{\phi}_{4+M_2}^{\mathrm{m}} \end{array}\right]$, only M_2 low-frequency flexible mode shape functions are retained, from the original M ones (also zero-frequency rigid modes, obtained from the eigenvalue problem, are dropped). We define new orthogonal zero-frequency rigid body mode shape functions $\boldsymbol{\Phi}^{\mathrm{m}}_{\mathrm{rigid}} = \left[\begin{array}{ccc} \boldsymbol{\phi}_1^{\mathrm{m}} & ... & \boldsymbol{\phi}_4^{\mathrm{m}} \end{array}\right]$ as

$$\left[\begin{array}{cc} \boldsymbol{\phi}_1^{\mathrm{m}} & \boldsymbol{\phi}_2^{\mathrm{m}} \end{array}\right] = \left[\begin{array}{ccccccccc} 1 & 0 & 0 & 0 & \cdots & 1 & 0 & 0 & 0 \\ 0 & 1 & 0 & 0 & \cdots & 0 & 1 & 0 & 0 \end{array}\right]^{\mathrm{T}}, \tag{3.26}$$

$$\begin{aligned} \left[\begin{array}{cc} \boldsymbol{\phi}_3^{\mathrm{m}} & \boldsymbol{\phi}_4^{\mathrm{m}} \end{array}\right] \; = \; & \left[\begin{array}{ccccccccc} 0 & -z_1 & 1 & 0 & \cdots & 0 & -z_{\mathrm{M}} & 1 & 0 \\ z_1 & 0 & 0 & 1 & \cdots & z_{\mathrm{M}} & 0 & 0 & 1 \end{array}\right]^{\mathrm{T}} \\ & + \left[\begin{array}{cc} z_0 \boldsymbol{\phi}_2^{\mathrm{m}} & -z_0 \boldsymbol{\phi}_1^{\mathrm{m}} \end{array}\right], \end{aligned}$$

where $\boldsymbol{\phi}_1^{\mathrm{m}}$, $\boldsymbol{\phi}_2^{\mathrm{m}}$, $\boldsymbol{\phi}_3^{\mathrm{m}}$, $\boldsymbol{\phi}_4^{\mathrm{m}}$, z_k, z_0 correspond to the transversal motion (in x and y axis), tilting motion (about x and y axis), location of k-th node, and location of the center of gravity of the rotor. In addition, to add some physical meaning to the displacements that result from the flexible modes, the $\boldsymbol{\Phi}^{\mathrm{m}}_{\mathrm{flex}}$ is scaled in such a way that the maximal displacement (resulting from the same mode) in x or y direction is equal to the unit modal weight (1 m).

Now, it is possible to relate the physical displacement vector $\boldsymbol{\eta}^{\mathrm{g}}$ and the modal coordinates $\boldsymbol{\eta}^{\mathrm{m}}$ as

$$\boldsymbol{\eta}^{\mathrm{g}} = \boldsymbol{\Phi}^{\mathrm{m}}\boldsymbol{\eta}^{\mathrm{m}}. \tag{3.27}$$

Equation (3.27) is the approximation after truncation of high-frequency modes, hence it neglects high-frequency dynamics. The set of reduced and decomposed (coupled only by $\boldsymbol{G}^{\mathrm{m}}$ matrix) equations of motion for the studied system in the modal coordinates and in the generalized form are

$$\boldsymbol{M}^{\mathrm{m}}\ddot{\boldsymbol{\eta}}^{\mathrm{m}} + \left(\boldsymbol{D}_{\mathrm{M}}^{\mathrm{m}} + \Omega\boldsymbol{G}^{\mathrm{m}}\right)\dot{\boldsymbol{\eta}}^{\mathrm{m}} + \boldsymbol{K}^{\mathrm{m}}\boldsymbol{\eta}^{\mathrm{m}} = \mathbf{f}^{\mathrm{m}}, \tag{3.28}$$

where the modal matrices and modal vector of forces are

$$\boldsymbol{M}^{\mathrm{m}} = (\boldsymbol{\Phi}^{\mathrm{m}})^{\mathrm{T}}\boldsymbol{M}^{\mathrm{g}}\boldsymbol{\Phi}^{\mathrm{m}},\ \boldsymbol{D}_{\mathrm{M}}^{\mathrm{m}} = (\boldsymbol{\Phi}^{\mathrm{m}})^{\mathrm{T}}\boldsymbol{D}_{\mathrm{M}}^{\mathrm{g}}\boldsymbol{\Phi}^{\mathrm{m}}, \tag{3.29}$$

$$\boldsymbol{G}^{\mathrm{m}} = (\boldsymbol{\Phi}^{\mathrm{m}})^{\mathrm{T}}\boldsymbol{G}^{\mathrm{g}}\boldsymbol{\Phi}^{\mathrm{m}},\ \boldsymbol{K}^{\mathrm{m}} = (\boldsymbol{\Phi}^{\mathrm{m}})^{\mathrm{T}}\boldsymbol{K}^{\mathrm{g}}\boldsymbol{\Phi}^{\mathrm{m}}, \tag{3.30}$$

$$\boldsymbol{f}^{\mathrm{m}} = (\boldsymbol{\Phi}^{\mathrm{m}})^{\mathrm{T}}\mathbf{f}^{\mathrm{g}}. \tag{3.31}$$

In Eq. (3.28), the diagonal matrices $\boldsymbol{M}^{\mathrm{m}}$, $\boldsymbol{K}^{\mathrm{m}}$ and the skew-symmetric $\boldsymbol{G}^{\mathrm{m}}$ are obtained from the FEM model. However, the damping matrix $\boldsymbol{D}_{\mathrm{M}}^{\mathrm{m}}$, which for the system decoupling is assumed to be stiffness-proportional, is obtained from the measured damping.

The damping factors and critical speeds of the few lowest bending modes can be measured using modal analysis. The damping is measured in relation to the critical damping ($\zeta_k = 1$). Therefore, the damping element $d_{\mathrm{M},k}^{\mathrm{m}}$ in the k-th DOF governing equation of form

$$m_k^{\mathrm{m}}\ddot{\eta}_k^{\mathrm{m}} + d_{\mathrm{M},k}^{\mathrm{m}}\dot{\eta}_k^{\mathrm{m}} + k_{\mathrm{M},k}^{\mathrm{m}}\eta_k^{\mathrm{m}} = 0, \tag{3.32}$$

which is equivalent to

$$\ddot{\eta}_k^{\mathrm{m}} + 2\zeta_k\omega_k\dot{\eta}_k^{\mathrm{m}} + \omega_k^2\eta_k^{\mathrm{m}} = 0, \tag{3.33}$$

is determined as $d_{\mathrm{M},k}^{\mathrm{m}} = 2\zeta_k k_{\mathrm{M},k}^{\mathrm{m}}/\omega_k$. The damping factors for the higher-frequency modes, which cannot be measured, has to be estimated. Usually, for high-frequency modes, ζ increases (up to the critical value) when the frequency is increased. However, the estimation of ζ is uncertain.

Equation (3.28) consists of the rigid body modes and the selected number of distinct slightly damped oscillators, which represent the flexible modes. As previously stated, k-th oscillator describes the free vibration of the mode shape function $\boldsymbol{\phi}_k^{\mathrm{m}}$. The corresponding oscillator has complex poles $s_k = -\sigma_k \pm j\omega_{\mathrm{d},k} = -\zeta_k\omega_k \pm j\omega_k\sqrt{1-\zeta_k^2}$ and, as it represents the under-damped case, its vibration decays as $\eta_k \sim e^{-\sigma_k t}\cos(\omega_{\mathrm{d},k}t + \varsigma_k)$.

Usually, four to ten modes with the lowest critical speeds are sufficient for accurate representation of the flexible rotor. The reduced mode shape functions matrix can be corrected by modal correction; also the FEM model can be iteratively corrected until the differences between the experimental modal analysis and the model are small enough.

The presented models assume that the axial motion is independent from the radial one. The axial motion is modeled as the motion of the point mass.

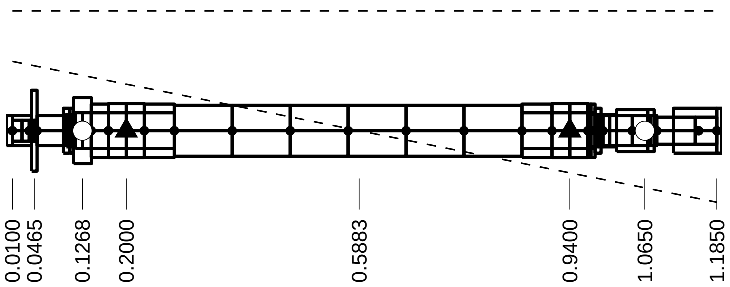

Figure 3.5: Sketch of the rotor model with the important locations given in [m], and the rigid body mode shape functions

Table 3.1: Critical speeds obtained from the FEM rotor model are slightly higher than the measured ones. The measurements were done using Brüer's & Kjeær's mode analyzer.

Mode k	FEM model, frequency [Hz]	Modal analysis, frequency [Hz]	Difference [%]	Damping ratio ζ_k
1	260.3	259.8	0.2	0.004118
2	539.0	526.7	2.3	0.002263
3	951.8	948.2	0.4	0.004345

3.2.4 Rotor of the test rig

In particular, the FEM representation of the rotor of the test rig comprises $P = 32$ nodes, located on the rotor's axis of symmetry (z axis); this corresponds to 128-DOF system. The rotor shape with the locations of its most important nodes (beginning of the shaft, location of axial disk, sensors – white circles, radial actuators – black triangles, end of the shaft) and the location of the center of the mass, is presented in Fig. 3.5.

The damping factors and critical speeds of the three lowest bending modes of the rotor were measured using Brüer's & Kjeær's mode analyzer. The results for the damping and critical speeds are presented in Table 3.1. The damping of the flexible modes for the complete rotor is higher than for the rotor without couplings, as presented in Publication IV, the first three free-free frequencies of the shaft alone are 343, 653, 1154 Hz. As the damping of the high-frequency modes, which are not measured, is unknown, it is estimated as in a worst-case scenario ($\zeta_{k>3} \approx 0.001$).

The rigid body modes and the first three flexible mode shape functions of the rotor model are presented in Fig. 3.5 and Fig. 3.6, respectively. In general, as can be seen in Fig. 3.6, the nodes of the mode shape functions are close to the location of bearings and sensors. In Fig. 3.7, the complete rotor, that is, the shaft, radial AMB laminations and couplings, under the modal analysis, is presented.

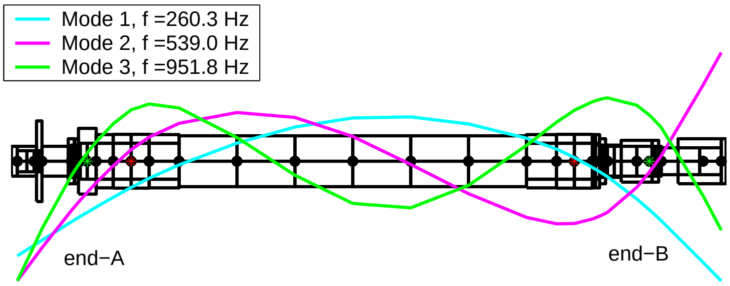

Figure 3.6: Sketch of the rotor model and the mode shapes of the first three low-frequency flexible modes, in (y, z) plane, are depicted. The mode shapes are multiplied by 0.2 in order to fit into the same figure as the rotor. The locations of the actuators and sensors are indicated with red and green stars, respectively. The rotor is at rest, i.e., there are no external forces, under free-free support, and $\Omega = 0$.

Figure 3.7: Complete rotor, under the modal analysis, consists of the shaft, axial disk, propeller coupling, AMB laminations fitted with aluminum sleeves, and additional aluminum sleeves for the position measurements.

3.3 Modeling of actuators

As has been shown, the mechanical subsystem can be modeled quite accurately; while, on the contrary, similarly accurate modeling of the nonlinear electromagnetic actuators is more difficult. In the analytical derivation of the magnetic force presented in subsection 2.3.1, we assume a linear magnetic circuit, neglect the leakage fluxes and magnetization of the iron. What is more, by writing Eq. (2.14) in the synthesis of the linear controller, we assume a linear relation between current and force. However, as argued by Polajzer et al. (2004), the nonlinearities of the magnetic force can be considerable, and hence they can degrade the performance of the control. Therefore, accurate electromechanical characteristics of the AMB are required to validate the controller and eventually to compensate the nonlinearities. Such accurate characteristics can be obtained using numerical methods.

3.3.1 Electromechanical characteristics of radial AMBs

The performance characteristics of radial AMBs were studied using a reluctance network method (RNM) by Pöllänen et al. (2005). This work took into account the magnetic saturation, cross coupling and leakage flux over the stator slots. The method was verified by comparing it with very accurate three-dimensional FEM analysis and experimental results (Nerg et al., 2005). The RNM provided a sufficient accuracy compared with FEM, yet it was less computationally intensive.

In the RNM, Maxwell's field equations are used to build a set of magnetic circuit equations. First, using Ampère's Circuital Law (2.2) introduced previously, the magnetic flux loops are described as

$$\sum_j H_{k,j} l_{k,j} = N_k i_k, \tag{3.34}$$

where $N_k i_k$ are the magnetomotive forces (mmf) that cause flux in the k-th loop, which consists of $j = 1$ to M branches, of the circuit. Second, Gauss' Law for magnetism $\nabla \cdot \mathbf{B} = 0$ is used to describe the conservation of flux in the nodes of the magnetic circuit. The RNM of a single electromagnet of the radial AMB is depicted in Fig. 3.8. As now the simplifying assumptions of the force derivations from subsection 2.3.1 are no longer valid, we can obtain the generalized set of the nonlinear equations in the matrix form

$$\boldsymbol{T}\boldsymbol{\Re}(\boldsymbol{\Phi}_{\mathrm{m}})\boldsymbol{T}^{\mathrm{T}}\boldsymbol{\Phi}_{\mathrm{ml}} = \boldsymbol{N}\mathbf{i}, \tag{3.35}$$

where $\boldsymbol{\Re}$, $\boldsymbol{\Phi}_{\mathrm{m}}$, $\boldsymbol{\Phi}_{\mathrm{ml}}$, $\boldsymbol{T}$, $\boldsymbol{N}$ and $\mathbf{i}$ are the diagonal reluctance matrix, the vector of branch fluxes, the vector of loop fluxes, the loop-set matrix (relates the branch fluxes to loop fluxes), the linkage matrix, and the vector of coil currents, respectively. The reluctances of the air-gaps are of the form

$$\Re_j = \frac{(l_0 - x_j)}{\mu_0 S_{\mathrm{air}}}, \tag{3.36}$$

where x_j is the deviation of the length of the j-th air-gap from the nominal

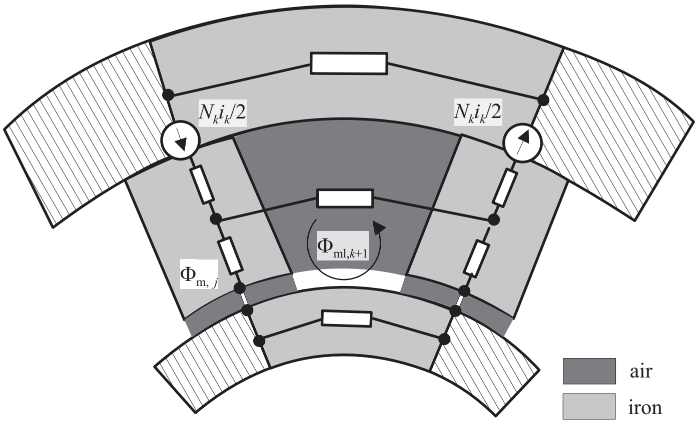

Figure 3.8: RNM of a single horseshoe electromagnet of the radial AMB

air-gap. In general, the initial values of the volume reluctances are of the form

$$\Re_j = \frac{l_j}{\mu_0 \mu_j S_j}, \tag{3.37}$$

where l_j, μ_j and S_j are the length of the j-th volume element, its relative permeability and area, respectively. The reluctances of the iron are updated according to the material B-H diagram, between the iteration steps, as

$$\Re_j = H_j \left(B_j\right) \frac{l_j}{\Phi_{\mathrm{m},j}}, \tag{3.38}$$

where $\Phi_{\mathrm{m},j}$ is the flux in the j-th branch. In Eq. (3.35), the fluxes are solved iteratively using a Newton-Raphson algorithm. Finally, from the field solution, the static electromagnetic characteristics of the radial AMB can be obtained. Similarly to the simplified force derivations, the accurate force characteristics are calculated using the magnetic energy as

$$W_{\mathrm{fe}} = \int\limits_V \int\limits_0^{\mathbf{B}} \mathbf{H} d\mathbf{B} dV = \int_0^{\boldsymbol{\Phi}_{\mathbf{m}}} \boldsymbol{\Phi}_{\mathrm{m}}^{\mathrm{T}} \boldsymbol{\Re} d\boldsymbol{\Phi}_{\mathrm{m}} = \frac{1}{2} \boldsymbol{\Phi}_{\mathrm{m}}^{\mathrm{T}} \boldsymbol{\Re} \boldsymbol{\Phi}_{\mathrm{m}}, \tag{3.39}$$

and the principles of the virtual work, with respect to the virtual displacement $\mathbf{x}$ as

$$\boldsymbol{f} = -\frac{\partial W_{\mathrm{fe}}}{\partial \mathbf{x}} = -\frac{1}{2} \boldsymbol{\Phi}_{\mathrm{m}}^{\mathrm{T}} \frac{\partial \boldsymbol{\Re}}{\partial \mathbf{x}} \boldsymbol{\Phi}_{\mathrm{m}}. \tag{3.40}$$

The detailed derivation of Eq. (3.39) can be found in Appendix A.2. The dynamic inductance matrix $\boldsymbol{L}_{\mathrm{dyn}}$, containing self and mutual inductances, can be calculated from the flux linkage as $\boldsymbol{L}_{\mathrm{dyn}} = \partial \boldsymbol{\Psi} / \partial \mathbf{i}$, where $\boldsymbol{\Psi}$ is the vector of coil flux linkages.

The force characteristics of a single horseshoe electromagnet versus the coil current and position (for the reduced premagnetization current $i_{\mathrm{bias}} = 2.5$ A, when the maximum total coil current $i_{\max} = 10$ A) obtained by the RNM are depicted in Fig. 3.9. The linearized force characteristics of two paired horseshoe

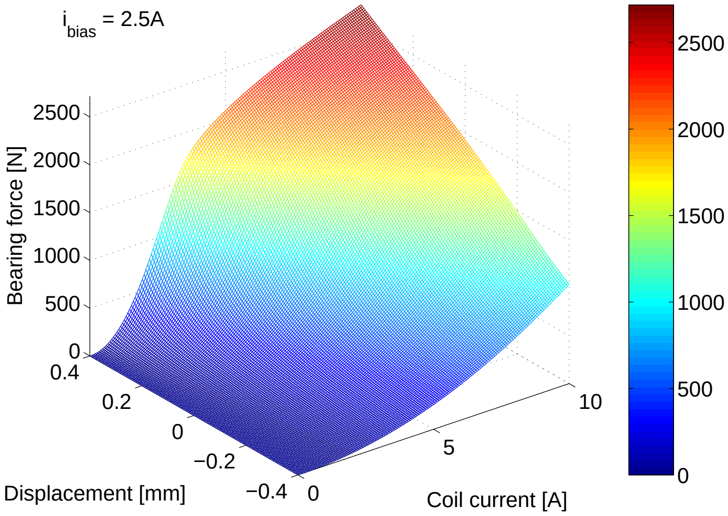

Figure 3.9: Force characteristics of single electromagnet as a function of the coil current and displacement in the x and y planes.

electromagnets are presented in Fig. 3.10. The obtained inductance of the single electromagnet as a function of the coil current and the rotor displacement is shown in Fig. 3.11. The presented three-dimensional magnetic force and inductance fields can be used in simulations and for the control purposes, provided that they are combined with a computationally non-intensive look-up table and polynomial interpolations (Publication V).

The comparison of the force-field relation measured in the prototype with the one obtained with the RNM is presented in Fig. 3.12. The weight of the rotor was used as a counterforce for the magnetic forces. The measurements were carried out within the available clearances, for stable operation ranges under the closed-loop control.

We refer those readers interested in a more detailed study of the RNM to Antila (1998) and Pöllänen et al. (2005).

3.3.2 Characteristics of axial AMBs

For the axial magnetic bearing, as discussed in section 2.5, the $i_{\text{sat}} < i_{\max}$, and therefore, when modeling the magnetic force, we can use Eq. (2.9) (more safely than with the radial bearing). The linearized force characteristics of the axial electromagnet as a function of control current at the nominal air-gap, and as a function of position at the bias current, are shown in Fig. 3.13.

3.3.3 Actuator dynamics

The bearing dynamics are examined using the voltage equation of the coil of a single electromagnet. The voltage of the coil u equals to the voltage drop according to Ohm's Law Ri plus the change of the flux linkage in time.

$$u = \frac{d\psi}{dt} + Ri = \frac{\partial\psi}{\partial i}\frac{di}{dt} + \frac{\partial\psi}{\partial x}\frac{dx}{dt} + Ri. \tag{3.41}$$

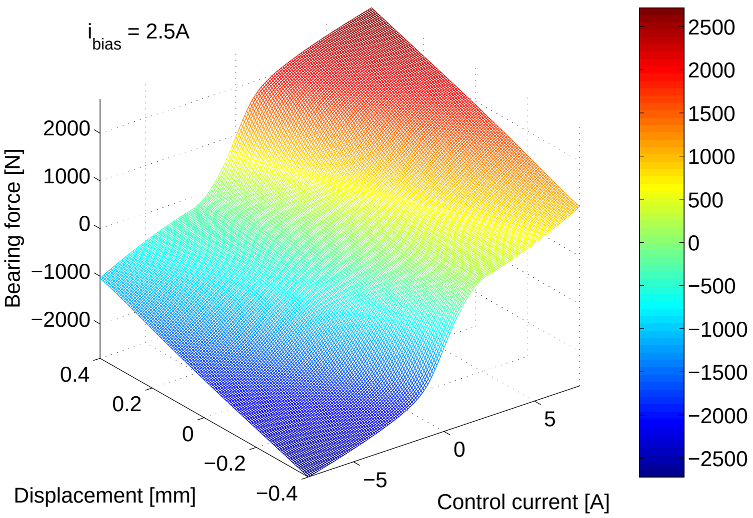

Figure 3.10: Force characteristics of two paired horseshoe electromagnets as a function of the control current and displacement in the x and y planes.

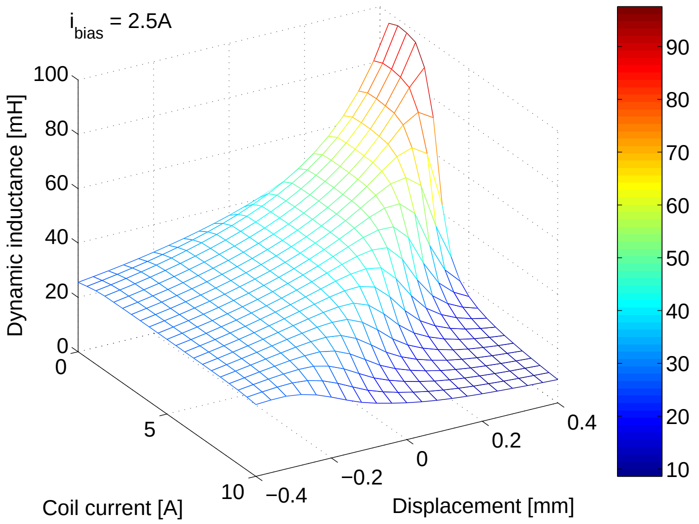

Figure 3.11: Calculated dynamic inductance of one electromagnet, as a function of coil current and displacement of the rotor from the central position toward the electromagnet.

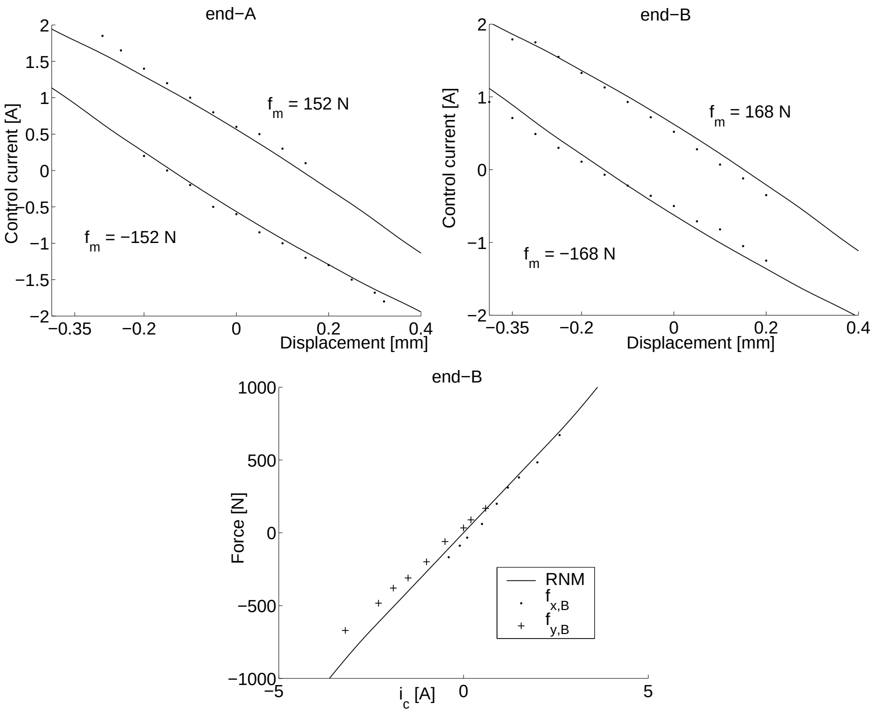

Figure 3.12: Top two graphs depict the control currents as a function of displacements, measured (dots) and computed with the RNM (solid lines), in the radial bearings, are depicted. In the bottom figure, the measured magnetic force as a function of control current is shown.

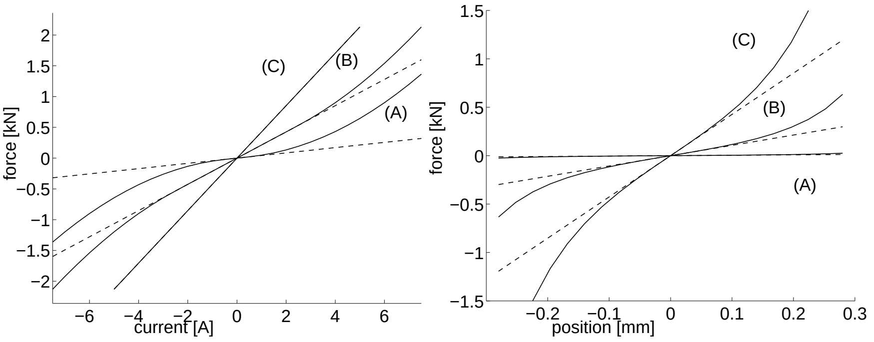

Figure 3.13: Force characteristics of an axial horseshoe electromagnet, for three bias currents: (A) $i_{\text{bias}} = 0.5\,[\text{A}]$, (B) $i_{\text{bias}} = 2.5\,[\text{A}]$, (C) $i_{\text{bias}} = 5\,[\text{A}]$.

Considering the displacement of the rotor in x direction (toward the electromagnet with the inductance L), and using the dynamic inductance, defined earlier, the voltage equation can be written as

$$u = L_{\mathrm{dyn}}\frac{di}{dt} + i\frac{dL}{dx}\frac{dx}{dt} + Ri = L_{\mathrm{dyn}}\frac{di}{dt} + k_u\frac{dx}{dt} + Ri. \tag{3.42}$$

Here, we introduce the flux linkage $\psi = Li$ and the velocity-induced voltage $k_u\dot{x}$ (or motion-induced back electromotive force). The inductance of a single horseshoe electromagnet (in the operating point, i.e., $x = 0$, and when the magnetization of the iron is neglected) can be computed using the flux density in the air-gap (2.5) or reluctance of the air-gap (3.36) as

$$L = NS_{\mathrm{air}}\frac{dB}{di} = \frac{N^2}{2\Re_{\mathrm{air}}} = \frac{\mu_0 N^2 S_{\mathrm{air}}}{2(l_0 - x)}. \tag{3.43}$$

Hence, using this result, comparing with Eq. (2.8), and (2.15), the velocity-induced voltage coefficient may be approximated as

$$k_u = i\frac{dL}{dx} = \frac{\mu_0 N^2 i S_{\mathrm{air}}}{2(l_0 - x)^2} \approx \frac{1}{2}k_i. \tag{3.44}$$

The same result may be obtained from (2.5) and directly from the partial derivative of the flux linkage ψ with respect to the air-gap. In the operating point, the k_u equals the current stiffness of the single electromagnet that is half of the k_i (the current stiffness of two paired, opposite electromagnets in the differential driving mode). If a more accurate model for k_u is required, it could be obtained by building the look-up table from the dynamic inductance.

We recall that we assumed a current-controlled AMBs with the biased control currents $i_{\mathrm{ref}} = \max(i_{\mathrm{bias}} \pm i_{\mathrm{c}}, 0)$. In the system, the input to the actuators consists of four radial reference currents and one axial one. Most often, in each actuator, an independently controlled current loop is built using a proportional controller as

$$u_{\mathrm{ref}} = G_{\mathrm{P}}\left(i_{\mathrm{ref}} - i_{\mathrm{m}}\right), \tag{3.45}$$

where u_{ref}, G_{P}, and i_{m} are the reference voltage, the proportional gain, and the measured coil current i, respectively. When analyzing the dynamics of the inner current closed-loop, it is typical (e.g. Schweitzer et al., 2003, Lantto, 1999, and Larsonneur, 1990) to simplify the problem by neglecting the velocity-induced voltage. This is possible because of its relatively insignificant magnitude, compared with the voltage of the coil. Additionally, the k_u introduces the derivative that has a stabilizing effect; it counteracts the effect of the negative position stiffness. Furthermore, it is typical that the resistance of the coil is small and could be neglected. With all these assumptions and utilizing (3.42), and (3.45), the simplest approximation of the closed-loop dynamics becomes

$$G_{\mathrm{cl}}(s) = \frac{i_{\mathrm{m}}}{i_{\mathrm{ref}}} \approx \frac{G_{\mathrm{P}}}{sL + G_{\mathrm{P}}} = \frac{1}{s\tau_{\mathrm{cl}} + 1}, \tag{3.46}$$

where τ_{cl} is the closed-loop time constant.

The more detailed model includes the PWM delay. The PWM delay can be approximated using a shift in time in the Laplace domain and different series expansions, for example Maclaurin (for low-order approximation), which yields

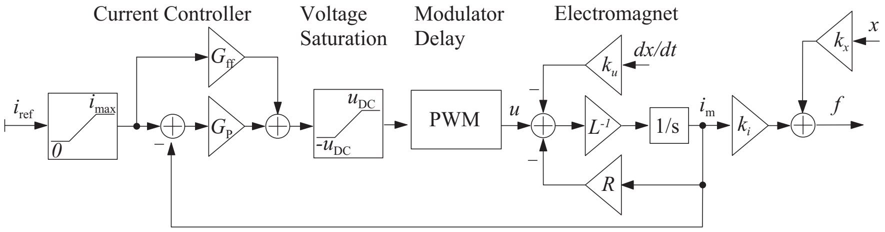

Figure 3.14: Actuator block diagram model comprises the force field (with the current stiffness k_i and position stiffness k_x), LR circuit, switched amplifier modeled as the delay, and internal current controller, where G_{P} and G_{F} indicate the proportional controller gain and feedforward controller gain, respectively.

$$e^{s\xi} \approx 1 + s\xi + \frac{(s\xi)^2}{2!} + ... + \frac{(s\xi)^n}{n!} + ..., \tag{3.47}$$

where ξ is the time shift in seconds. We can use (3.47) for the linear time invariant models (like state-variable form and transfer functions). For example, a second-order approximation of a delay is $e^{s\xi} \approx 1/[s^2T_{\mathrm{md}}^2/4 + sT_{\mathrm{md}}/2 + 1]$. In Matlab Simulink we can utilize a Transport Delay block, for PWM delay to provide much shorter simulation times compared with the switching models (Wurmsdobler, 1997). The first-order Maclaurin approximation corresponds to the first-order (0/1) Padé approximation (Franklin et al., 1998). For the delay $\xi = -T_{\mathrm{md}}/2$ this first-order approximation, as the transfer function, yields

$$G_{\mathrm{del}}(s) \approx e^{s\xi} \approx \exp_{0/1}(s\xi) = \frac{1}{1 - s\xi} = \frac{1}{s\frac{T_{\mathrm{md}}}{2} + 1}, \tag{3.48}$$

where T_{md} is the average modulation delay that equals half of the modulation period owing to the asymmetric regular sampling.

Finally, the slightly more detailed approximation of the current control closed-loop dynamics is

$$G_{\mathrm{cl}}(s) \approx \frac{G_{\mathrm{P}}G_{\mathrm{del}}(s)}{sL + R + G_{\mathrm{P}}G_{\mathrm{del}}(s)}. \tag{3.49}$$

The voltage relation together with the force relation (2.14), internal current controller and PWM delay form the complete actuator model, as presented in Fig. 3.14, where the feedforward controller gain compensates the resistive voltage drop.

The schematic of load capacity limitations of the AMB actuator is presented in Fig. 3.15. The maximum force of the bearing system is determined by the maximum coil current $f_{\max} = F(i_{\max})$. The maximum constant coil current is determined by the values of the resistance R and available DC link voltage u_{DC} ($i_{\mathrm{DC,max}} = u_{\mathrm{DC}}/R$). However, usually this limit is high and thus theoretical. In practice, the maximum force for the continuous operation is limited by the coil temperature limit. Typically, the coil temperature limit is described as the coil current, at which a maximum current density in a coil reaches the certain limit $J_{\max} = 4 - 6\,\mathrm{A/mm^2}$. One but a difficult opportunity for more accurate estimation of the current associated with the coil temperature limit could be a thermal analysis (Pöllänen et al., 2006). Another option could be to use the fact that the static load capacity of the amplifier is limited by the size and geometry of the bearing (see Eq. 2.17). Hence, to limit the saturation influence on system dynamics and linearity, we may select the limiting current to be equal to the saturation current (see Eq. 2.22). A peak transient current, at low frequencies, is determined by the artificially selected maximum peak current, at which the controller, and control electronics (limited measuring range of the current sensors and limited number format) can provide a stable suspension. For high frequencies, the dynamic load capacity is determined by either the current control bandwidth (using Eq. 3.46, $\omega_{\text{cl}} \approx G_{\text{P}}/L$) or by the power bandwidth ω_{BW}, whichever is more restrictive.

A power bandwidth results from the limited DC link voltage, the low-pass characteristics of the coil transfer function applied to sinusoidal signals, and the maximum current. It can be estimated by using the open-loop plant scaled by the u_{DC}, which is equal to the voltage limited current amplitude as

$$i_{u,\max} = u_{\text{DC}} G_{\text{pl}} = u_{\text{DC}} \frac{G_{\text{del}}}{(sL+R)}, \tag{3.50}$$

where the peak-to-peak current of $2 \cdot i_{u,\max}$ equals to the maximum current $i_{\max}$. The frequency at which the voltage enters the saturation ω_{sat} may be determined by the crossing of the magnitude Bode plots of the transfer function based on the controller dynamics (3.49) and the voltage-limited current-amplitude ratio (3.50), specifically $2u_{\text{DC}}/i_{\max} \cdot 1/(sL+R)$. The power bandwidth approximation ω_{BW} can be read, directly from the Bode magnitude plot, approximately at the -3dB crossing of the voltage-limited current-amplitude ratio (used as a transfer function). Another approximation of the dynamic force limitation that takes the inductance variations into account, as given by Lantto (1999), is based on the rise time t_{rise} of the current in the coil of the electromagnet L_{dyn} from zero to $i_{\max}$. Utilizing a response of the first-order approximation of the system, the power bandwidth is

$$\omega_{\text{BW}} = \frac{\ln(9)}{t_{\text{rise}}}, \; t_{\text{rise}} \approx \frac{1}{u_{\text{DC}}} \int_{0}^{i_{\max}} L_{\text{dyn}}(i, x_0) di, \tag{3.51}$$

where u_{DC} is the DC link voltage applied to the coil. Replacing the dynamic inductance by the nominal one, assuming the $f_{\max}$ at the $i_{\max} = i_{\text{sat}}$, using (3.43), and (2.22), the power bandwidth can be presented in terms of the maximum force amplitude $f_{\max}$ (2.17) and the maximum amplifier performance $P_{\max} = i_{\max} u_{\text{DC}}$, as

$$\omega_{\text{BW}} \approx \frac{\ln(9) u_{\text{DC}}}{L i_{\max}} = \frac{\ln(9) P_{\max}}{L i_{\max}^2} = \frac{\ln(9) P_{\max} \cos\chi}{2 l_0 f_{\max}} \approx \frac{P_{\max} \cos\chi}{l_0 f_{\max}}. \tag{3.52}$$

If the current control bandwidth is above the power bandwidth ($\omega_{\text{cl}} > \omega_{\text{BW}}$), the load capacity is limited by the amplifier performance and by the DC link voltage. In consequence, at the frequencies greater than the ω_{sat}, the bearing cannot produce forces with amplitudes determined by the controller dynamics. The ω_{sat} is determined at the point where the voltage limit curve crosses with

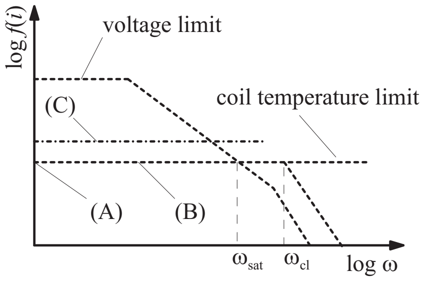

Figure 3.15: Limits on AMB: (A) the static load capacity, (B) the dynamic load capacity under continuous operation, (C) the peak transient load capacity

the magnitude plot of the transfer function of the controller. The rough first-order approximation of the actuator dynamics becomes

$$G_{\mathrm{cl}}(s) \approx \frac{\omega_{\mathrm{BW}}}{s+\omega_{\mathrm{BW}}}. \tag{3.53}$$

Alternatively, for higher-order approximations of the closed-loop dynamics, we can modify Eq. (3.49), by utilizing a describing function method (Franklin et al., 1998) and (Slotine and Li, 1991). The derivation of the describing function $\Gamma(G_{\mathrm{P}} i_{\mathrm{ref}})$ for the actuator saturation is presented in Appendix A.4. The quasi-linearized actuator, for sinusoidal input and output, yields

$$G_{\mathrm{cl}}(s) \approx \frac{\Gamma(u_{\mathrm{ref}}) G_{\mathrm{P}} G_{\mathrm{del}}(s)}{sL + R + \Gamma(u_{\mathrm{ref}}) G_{\mathrm{P}} G_{\mathrm{del}}(s)}, \tag{3.54}$$

$$\Gamma(u_{\mathrm{ref}}) = \left\{ \begin{array}{cc} \frac{2}{\pi} \arcsin\left(\frac{u_{\mathrm{DC}}}{u_{\mathrm{ref}}}\right) + \frac{2u_{\mathrm{DC}}}{\pi u_{\mathrm{ref}}} \cdot \sqrt{1 - \left(\frac{u_{\mathrm{DC}}}{u_{\mathrm{ref}}}\right)^2}, & u_{\mathrm{ref}} > u_{\mathrm{DC}} \\ 1, & u_{\mathrm{ref}} \leq u_{\mathrm{DC}} \end{array} \right\}, \tag{3.55}$$

where u_{ref} is assumed, here, to be the amplitude of the sinusoidal input (3.45). The control bandwidth can be estimated as a bandwidth of (3.54), where $u_{\mathrm{ref}} = 0.5 \cdot G_{\mathrm{P}} i_{\mathrm{max}}$ (for single electromagnet). For high amplitudes of a coil current, the effect of the dynamic inductance may be included into (3.54) by using (in the computations), such a value for L, that gives the same rise time as the L_{dyn} in Eq. (3.51). However, for high frequencies, the voltage is saturated and coil currents are bound in the region where the inductance is close to its nominal value.

The exemplary Bode plots for different approximations of actuator dynamics are presented in Fig. 3.16. The main benefit of using (3.54) is the inclusion of both the saturation and the modulation delay in one model.

As to the dynamics of two opposite horseshoe electromagnets, the maximum load capacity at different frequencies depends on the maximum possible force slew rate, for $x = 0$, $df/dt = k_i(i) \cdot di_{\mathrm{c}}(i)/dt$. As explained earlier, in the operating point, the current stiffness of a single electromagnet equals half of the corresponding k_i of two opposite electromagnets, as does the force slew rate and a peak-to-peak value of the force. The rate of change of the reference current, in the single electromagnet, corresponds to the rate of change of the biased control current, for two opposite electromagnets, where each of them generates the force in one direction only, and uses its full load capacity. We may consider two cases.

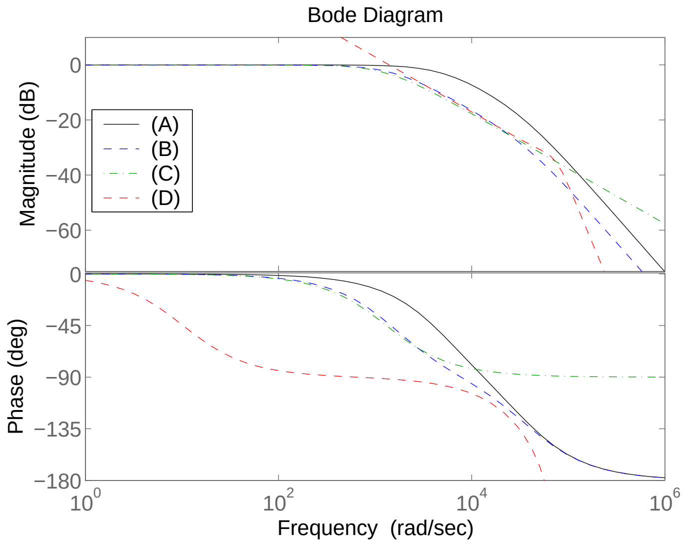

Figure 3.16: Bode plots of the approximated actuator dynamics, for $\omega_{\mathrm{cl}} > \omega_{\mathrm{sat}}$: (A) based on (3.49), (B) based on (3.54), (C) based on (3.53), (D) the DC link voltage limit for the open-loop Eq. (3.50).

1. If the control current amplitude is lower than or equal to i_{bias}, the rate of change of the control current is the same as the rate of change of the reference currents (both coils are active). Consequently, the voltage saturation appears approximately at ω_{sat}, and the frequency responses of the single electromagnet are the same as the frequency responses of two opposite electromagnets (Fig. 3.17).
2. If the control current amplitude is greater than i_{bias}, the rates of change of two resulting reference currents (from the applied i_{c}) are greater than the rate of change of the i_{c}. Consequently, the voltage saturation appears earlier than at ω_{sat} (determined for a single electromagnet without reduced premagnetization current), and the frequency responses differ from the predicted ones (the derived linear models are more uncertain). The actual ω_{sat} changes and depends on the control signal amplitude and bias. In addition, the intrinsic system nonlinearities become larger for higher values of position and current signals (Fig. 3.18).

To put the second point in another way, for low and medium frequencies and for amplitudes of the control current that are greater than the value of the bias current, the rate of change of a magnetic force is contributed mostly by one electromagnet (for very high frequencies, the coil current amplitudes are reduced below $2 \cdot i_{\mathrm{bias}}$ and both electromagnets produce force). For these reasons, the force response may deviate considerably from the linearized one, at the operating point, model prediction.

Figures 3.17 and 3.18 show comparisons of the normalized gains (resulting from different force magnitudes) and phase Bode diagrams obtained from the single electromagnet (A), two opposite electromagnets (B), and different actuator approximations of the system with $\omega_{\mathrm{cl}} > \omega_{\mathrm{BW}}$. The Bode plots (A) and

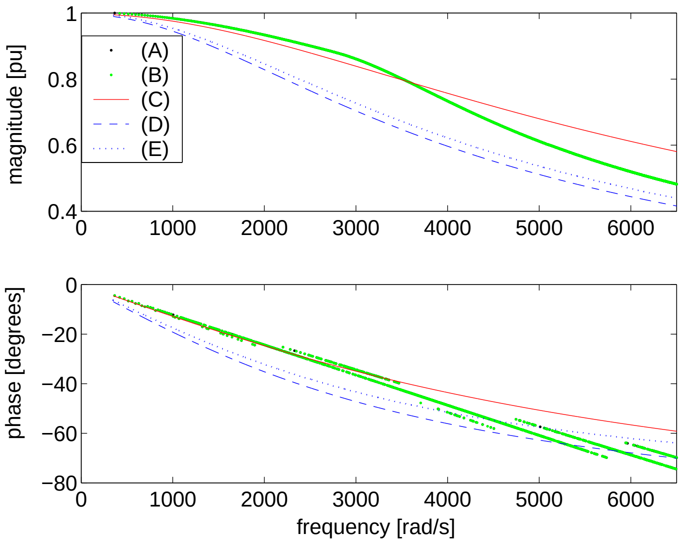

Figure 3.17: Frequency responses of the simulated models and different linear approximations are presented. The $i_{\max} = 2 \cdot i_{\text{bias}} = 5\,\text{A}$. The saturation occurred at $\omega_{\text{sat}} = 2800$ rad/s, according to prediction (3.50). The saturation occurred at $\omega_{\text{sat}} = 2762$ rad/s, according to simulation.

(B) were obtained using the Simulink models, which included the force nonlinearities, inductance nonlinearities, modulation delay, and voltage saturation. The responses of the approximated models comprise (C) approximation based on (3.49), (D) approximation based on (3.54), and (E) approximation based on (3.53). For frequencies lower than ω_{sat}, the frequency responses of the Simulink models are similar to the response of Eq. (3.49) (the agreement is not so close for the system with the high signal amplitudes), and the voltages do not saturate. For the frequencies higher than ω_{sat}, the amplifiers enter saturation, and the frequency responses of the Simulink models approach the response of (3.54). In the simulations the same current controllers (with the same gains), with a considerably high bandwidth ω_{cl} (control design for $t_{\text{r}} = 500\mu\text{s}$), were used. The applied reference for single electromagnet $i_{\text{ref}} = 0.5 \cdot i_{\max} \sin(\omega t) + 0.5 \cdot i_{\max}$, and the applied control current for opposite electromagnets $i_{\text{c}} = i_{\max} \sin(\omega t)$.

3.4 Measurements and filtering

There are two main reasons for the inclusion of filtering into the position measurements in the system. The first one is to improve the quality and reliability of the measured signal. The anti-aliasing filter, placed before the ADC input, attenuates the frequency components above half the sampling rate and thus fulfills the Nyquist theorem. The additional filter, for example, digital median filter, placed after the AD conversion, can eliminate the possible occasional erroneous conversion results and prevent the ADC error from propagating to the control system. The second reason for filtering is the elimination of the observation spillover coming from the residual modes (Balas, 1978). When assembling the

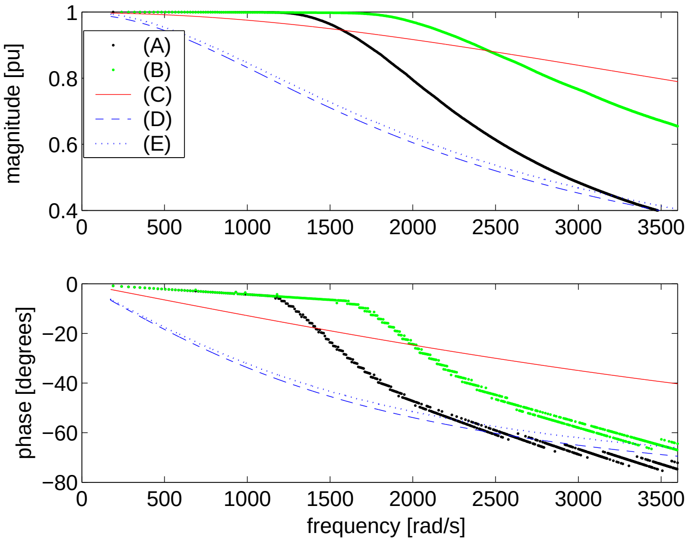

Figure 3.18: Frequency responses of the simulated models and different linear approximations are shown. The $i_{\max} = 4 \cdot i_{\text{bias}} = 10\,\text{A}$. The saturation occurred at $\omega_{\text{sat}} = 1230$ rad/s, according to prediction (3.50). The saturation occurred at $\omega_{\text{sat}} = 830$ rad/s (A-model) and $\omega_{\text{sat}} = 1322$ rad/s (B-model), according to the simulation.

plant model, the applied filter cannot be neglected. In many cases, the simple model of the first-order low-pass filter, such as $G(s) = \omega/(s+\omega)$, where ω is the cut-off frequency in [rad/s], is sufficient.

3.5 Overall plant model

In this section, as the studied physical process (control plant) is continuous, the continuous-time models are considered. First, based on the equation of motion (3.28), the state-space model of the rotor is formed according to Genta et al. (1993). Then, the obtained state-space model of the mechanical sub-system is combined with the actuator model, for instance (3.46), and the filter model, yielding an overall plant model.

The open-loop state-space equation of the radially suspended rotor, with the linear uncontrolled radial AMBs is

$$\dot{\mathbf{x}}_{\text{r}} = \boldsymbol{A}_{\text{r}}\mathbf{x}_{\text{r}} + \boldsymbol{B}_{\text{r}}\mathbf{u},\ \mathbf{y} = \boldsymbol{C}_{\text{r}}\mathbf{x}_{\text{r}} + \boldsymbol{D}_{\text{r}}\mathbf{u}, \tag{3.56}$$

$$\boldsymbol{A}_{\text{r}} = \begin{bmatrix} \mathbf{0} & \mathbf{I} \\ -(\boldsymbol{M}^{\text{m}})^{-1}(\boldsymbol{K}^{\text{m}} + \boldsymbol{K}_x^{\text{m}}) & -(\boldsymbol{M}^{\text{m}})^{-1}(\boldsymbol{D}_{\text{M}}^{\text{m}} + \Omega\boldsymbol{G}^{\text{m}}) \end{bmatrix}, \tag{3.57}$$

$$\mathbf{x}_{\text{r}} = \begin{bmatrix} \boldsymbol{\eta}^{\text{m}} \\ \dot{\boldsymbol{\eta}}^{\text{m}} \end{bmatrix},\ \boldsymbol{B}_{\text{r}} = \begin{bmatrix} \mathbf{0} \\ -(\boldsymbol{M}^{\text{m}})^{-1}\boldsymbol{K}_i^{\text{m}} \end{bmatrix},\ \boldsymbol{C}_{\text{r}} = \begin{bmatrix} \boldsymbol{S}_{\text{m}}\boldsymbol{\Phi}^{\text{m}} & \mathbf{0} \end{bmatrix}, \tag{3.58}$$

$$\boldsymbol{D}_{\mathrm{r}} = \mathbf{0},\ \boldsymbol{K}_i^{\mathrm{m}} = (\boldsymbol{\Phi}^{\mathrm{m}})^{\mathrm{T}} \boldsymbol{S}_{\mathrm{a},i} \boldsymbol{K}_i,\ \boldsymbol{K}_x^{\mathrm{m}} = (\boldsymbol{\Phi}^{\mathrm{m}})^{\mathrm{T}} \boldsymbol{S}_{\mathrm{a},x} (-\boldsymbol{K}_x) \boldsymbol{\Phi}^{\mathrm{m}}, \tag{3.59}$$

where $\boldsymbol{S}_{\mathrm{m}}$, $\boldsymbol{S}_{\mathrm{a},i}$ and $\boldsymbol{S}_{\mathrm{a},x}$ are the nodal location matrices of measurement, current stiffness and position stiffness, respectively. The $\boldsymbol{S}_{\mathrm{m}}$ has a number of rows equal to the number of nodes related to the sensors and a number of columns equal to the number of DOF $(4 \cdot P)$; likewise, the $\boldsymbol{S}_{\mathrm{a},i}$ has appropriate dimensions (number of DOF, number of nodes related to the actuators). The $\boldsymbol{S}_{\mathrm{a},x}$ is a square matrix with rows and columns equal to the number of DOF and with all elements equal to zero except for the diagonal elements corresponding to the locations of the actuators, which are equal to one. In this model, the vector of inputs $\mathbf{u}$ consists of four control currents $\mathbf{i}_{\mathrm{c}} = [i_{\mathrm{c},x,\mathrm{A}},\ i_{\mathrm{c},y,\mathrm{A}},\ i_{\mathrm{c},x,\mathrm{B}},\ i_{\mathrm{c},y,\mathrm{B}}]^{\mathrm{T}}$, and the vector of outputs $\mathbf{y}$ consists of measured rotor displacements $\mathbf{x}_{\mathrm{m}} = [x_{\mathrm{A}},\ y_{\mathrm{A}},\ x_{\mathrm{B}},\ y_{\mathrm{B}}]^{\mathrm{T}}$. Similarly, the models with input magnetic forces, retainer bearing forces, disturbance forces and output measured at different nodes can be constructed.

The pole-zero distribution of the open-loop rotor model, with the ideal, uncontrolled radial AMBs and for $\Omega = 0$, is depicted in Fig. 3.19. Each cross and each circle indicate the locations of two poles and two zeros, respectively. They occur once for each plane, because of the axial symmetry of the system. The modes are arranged into alternating $(x,\ z)$ and $(y,\ z)$ planes. The modes of each plane are decoupled from each other, and cross coupled with the modes of orthogonal plane, through gyroscopic coupling. The strongest coupling is for the modes of the same frequency. In the AMB rotor systems, the coupling of two planes causes the poles and zeros associated with the rotor to change their locations along the imaginary axis in the opposite directions, with the increased rotational speed. This is usually depicted in the Campbell diagrams, as presented by Lösch (2002) and Genta et al. (1993). The poles changing their locations upwards in the s-plane are responsible for a forward whirling; and the poles changing their locations downwards are responsible for a backward whirling.

The overall linear, augmented plant model consists of the approximated actuator, flexible rotor and filtered position measurement models. It is practical to express the whole plant as the coupled set of the first-order differential equations in the state-variable form, that is

$$\dot{\mathbf{x}} = \boldsymbol{A}\mathbf{x} + \boldsymbol{B}\mathbf{u},\ \mathbf{y} = \boldsymbol{C}\mathbf{x} + \boldsymbol{D}\mathbf{u}, \tag{3.60}$$

$$\mathbf{x} = \begin{bmatrix} \mathbf{x}_{\mathrm{a}} \\ \mathbf{x}_{\mathrm{r}} \\ \mathbf{x}_{\mathrm{f}} \end{bmatrix},\ \boldsymbol{A} = \begin{bmatrix} \boldsymbol{A}_{\mathrm{a}} & \mathbf{0} & \mathbf{0} \\ \boldsymbol{B}_{\mathrm{r}}\boldsymbol{C}_{\mathrm{a}} & \boldsymbol{A}_{\mathrm{r}} & \mathbf{0} \\ \mathbf{0} & \boldsymbol{B}_{\mathrm{f}}\boldsymbol{C}_{\mathrm{r}} & \boldsymbol{A}_{\mathrm{f}} \end{bmatrix},\ \boldsymbol{B} = \begin{bmatrix} \boldsymbol{B}_{\mathrm{a}} \\ \mathbf{0} \\ \mathbf{0} \end{bmatrix}, \tag{3.61}$$

$$\boldsymbol{C} = \begin{bmatrix} \mathbf{0} & \mathbf{0} & \boldsymbol{C}_{\mathrm{f}} \end{bmatrix},\ \boldsymbol{D} = \mathbf{0}, \tag{3.62}$$

where subscripts (a, r and f) refer to the actuator, rotor, and filter, respectively. Analogically, the plant model for the axial suspension of the rotor is formed, where Eq. (3.1) is applied as a rotor model.

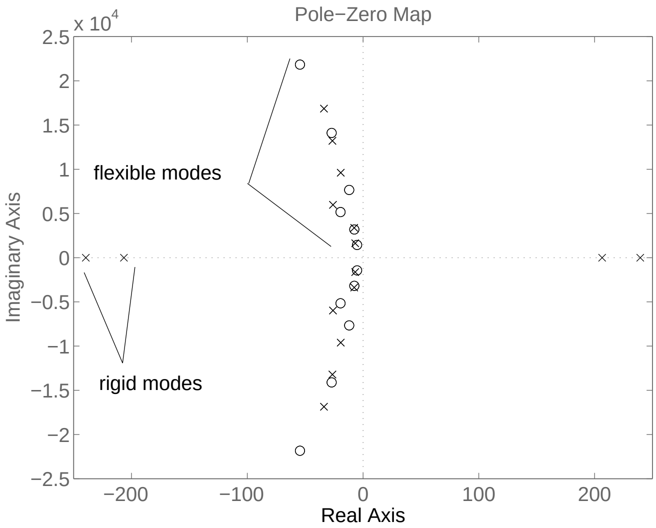

Figure 3.19: Pole-zero distribution of the flexible rotor and AMBs, at $\Omega = 0$. The model comprises four rigid body modes and twelve flexible modes.

3.6 Summary

To sum up, this chapter shows how to model AMB rotor systems by using magnetic circuit analysis for the bearings and finite elements for the rotor.

The mechanical models for radial suspensions of different complexity were presented: the set of 1-DOF decoupled systems, two 2-DOF systems coupled by the net bearing forces acting on the center of gravity (the rotor ends interact), rigid rotor 4-DOF model with states coupled by the bearing forces and gyroscopic matrix, and finally flexible rotor model. The states that correspond to the flexible modes were also gyroscopically coupled. The interactions between all the inputs and outputs of the control system were introduced. In the flexible model, the selected procedures allowed the inclusion of rigid disks and flexible beams as the finite elements. The presented FEM modeling assumed that the rotor is axisymmetric, parameters are time-invariant, the Ω is constant (though, in the simulation model it can be used as a parameter), damping was proportional, and finally, sensors and actuators were located in discrete nodes. Additionally, the axial and torsional degrees of freedom were not considered. The modeling of auxiliary bearings was beyond the scope of this work, and was not presented. However simple auxiliary bearing models, based on Kärkkäinen et al. (2006), can be used in simulations of lifting the rotor. What is more, the original FEM model, that feature many DOFs, was transformed from the global coordinates to the modal ones, and reduced by truncation of high-frequency modes. The support of the rotor was soft (the stiffness of the magnetic bearings is low compared with the rotor stiffness) and the rotor itself could be considered only slightly gyroscopic. For these reasons the eigenmodes and mode shapes do not considerably change as a function of AMB stiffness and angular speed Ω. Therefore, the model computed for $\Omega = 0$ is valid for wide rotational speed range. Nevertheless, the Ω split the eigenvalues associated with the flexible modes into the forward and backward modes. The sub-critical operation is possible for the rotational speeds below $\Omega \approx 260 \cdot 60 = 15600\,\mathrm{rpm}$. Finally, the derived FEM model yields a suitable structure for the system identification (Lösch, 2002).

Speaking about the rotor model and its equations of motion, this presentation considers the equation of motion with real values. However, the dimension of the equation can be halved by introducing the complex coordinates (see e.g. Genta et al., 1993 or Lantto, 1997).

For the actuators, the nonlinear forces can be modeled using the RNM and approximated with look-up table-based interpolation methods. For the simulation purposes, the accurate model of the current control loop of the actuator can be derived, including velocity-induced voltage, DC link voltage saturation, nonlinear force, and nonlinear inductance. The limitations introduced by the actuator were discussed. The simplified linearized model of the current control was derived for the control synthesis, and its uncertainties outside the operating point were considered. It is relatively simple to predict the frequency at which the voltage saturation occurs for different reference signal amplitudes in the actuator. On the contrary, the accurate prediction of the power bandwidth, especially when a reduced premagnetization current is applied, is more difficult.

All in all, the chapter contains a generalized description of the AMB rotor model, which is valid not only for the tested prototype but could be used as a basis for modeling of any AMB system with a flexible rotor and nonlinear actuators.

Chapter 4

Magnetic bearing control

At the beginning of this chapter, the AMB control principles, requirements and limitations are introduced. Next, the current control is discussed. After that, the PID and LQ control methods for position control are studied. The employed procedure for LQ control design is as follows. First, the different candidates for the control layout are examined. Then, the selected layout is used to build the axial position controller. Its performance, stability limits and robustness are studied. In the next section, the SISO LQ position control is generalized to the MIMO case, for the control of the radial suspension of the rotor, and compared with the multiple SISO PID-based controller. A discrete design and unbalance force rejection control are studied. The effects of dynamic inductance and static force-field nonlinearity are analyzed, and the suitable nonlinear compensation is proposed. The robust stability and performance, as well as adaptation according to changeable rotational speed are considered.

4.1 Control principles

In general, the control of a flexible rotor is far easier when the position of the sensors and actuators enhance the observability and controllability of the low-frequency modes. We will elaborate on this message, at first by introducing the spillover effect and then by recalling the flexible rotor model as in Fig. 3.6.

4.1.1 Spillover problem

From practical reasons, the model-based control utilizes the reduced-order model for the controller synthesis. However, both the controlled and residual modes contribute to the plant outputs. Contrary to what could have been perceived from Eq. (3.27), the physical displacement vector considered as a vector field of measurements is

$$\mathbf{y} = \begin{bmatrix} \mathbf{\Phi}^{\mathrm{m}} & \mathbf{\Phi}^{\mathrm{r}} \end{bmatrix} \begin{bmatrix} \boldsymbol{\eta}^{\mathrm{m}} \\ \boldsymbol{\eta}^{\mathrm{r}} \end{bmatrix}, \tag{4.1}$$

where the $\boldsymbol{\eta}^{\mathrm{m}}$ and $\boldsymbol{\eta}^{\mathrm{r}}$ represent the controlled and residual displacement vectors, respectively. After that correction, we can clarify that the control spillover appears when the controller excites the residual modes, and the observation spillover appears when the controller receives the information based on the truncated and the residual set of modes. The presence of these both spillovers can lead to instability. The third spillover type concerns the interconnection between the $\boldsymbol{\eta}^{\mathrm{m}}$ and $\boldsymbol{\eta}^{\mathrm{r}}$, hence it is called the interconnection spillover.

The spillover effect has been studied by many authors, for example by Balas (1978) and Schweitzer et al. (2003). The general rules to avoid the destabilizing effects of the spillovers are:

- to place the sensors as close to the actuators as possible
- to avoid the destabilizing feedback by designing the system in such a way that the nodes of the dominant eigenmode shapes are not between the actuator and sensor
- to enhance the observability and controllability of the low-order modes by placing the sensors and actuators far from the nodes of these controlled eigenmode shapes
- to degrade the observability and controllability of the high-order modes by placing the sensors and actuators close to the nodes of these uncontrolled eigenmode shapes

The problem is less serious in the collocated system with ideal actuation and sensing. The additional complication arises because of the variation of the location of nodes as a function of feedback amplitudes. Therefore, in the control solution, a compromise between the robustness and performance is expected.

4.1.2 Non-collocation of the prototype

In the prototype rotor, the relations between the sensors, actuators, and nodes of the eigenmode shapes were presented in Fig. 3.6. Additionally, the system dynamics can be examined by plotting the Bode diagrams of the rotor in AMBs (Fig. 4.1). In the end-A of the rotor, the node of the second flexible mode shape is located between the actuator and the sensor. Similar situation is with the first bending mode shape, in the end-B of the rotor. At the frequency associated with these modes, there is a negative phase shift. This negative phase shift indicates the non-collocation, to say, poles and zeros of the system are not interlaced in the complex plane. The non-collocation may cause the stability problems, for example when a rigid-body-based control of the flexible structure is considered, or when the flexible-body-based control is applied and the location of nodes of the flexible modes change. Furthermore, the main concern is the first flexible mode, as its frequency is in a power bandwidth of the system. In the end-B of the rotor, owing to the modeling errors and variation of parameters, the location of the node of the first mode shape function may vary, and thus it can produce a positive or negative phase. On the other hand, the peak magnitude of the resonance is relatively low. Therefore, we will not try to actively control this mode at the end-B.

In Chapter 3, when modeling a rotor, we have stressed the gyroscopic coupling between the (x, z) and (y, z) planes. This coupling, for different rotational speeds, combined with the coupling resulting from the flexible modes, is presented in a magnitude Bode plot of the system transfer function from the first

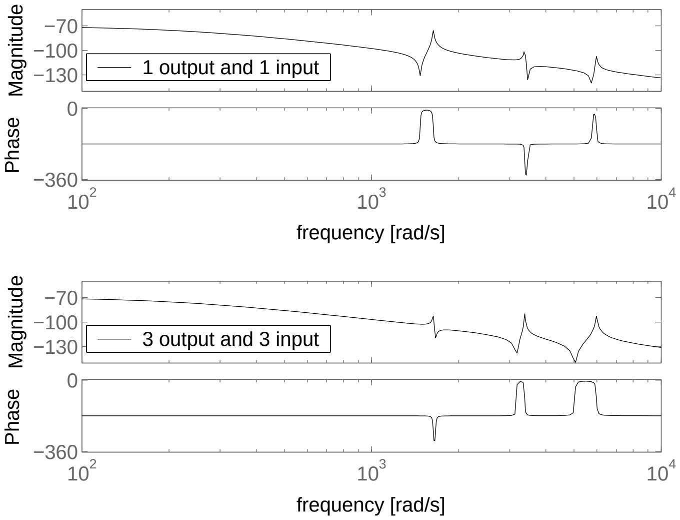

Figure 4.1: Bode diagram of the flexible rotor in AMBs, as derived in Chapter 3, at $\Omega = 0$. The magnitude is given in [dB] and the phase is in [deg].

input ($i_{\mathrm{c},x,\mathrm{A}}$) to the second output ($y_{\mathrm{A}}$), in Fig. 4.2. Even for the high rotational speed the coupling is not significant.

4.1.3 Objectives and control layout

Now, after introducing the control plant and its modeling, and after defining the threats of the rotor design (locations of sensors and actuators in relation to the bending mode shapes) we can state the general objectives for control design:

- compensating for the inherent instability of the magnetic bearings
- being able to lift up the rotor from the retainer bearing position to the operating point, and to follow the reference commands without the steady-state errors
- finding the controller that stabilizes the rigid body modes and the selected low-order flexible modes of the rotor without destabilizing the residual modes
- compensating for the actuator nonlinearities
- accounting for the variations of parameters (e.g., due to the aforementioned coupling and changes in eigenfrequencies with the rotational speed)
- achieving stable operation below critical speed and passing through the critical speeds if overcritical operation is required
- handling constant gravity force, mass unbalance and other disturbance forces, as well as the noise in the measurements

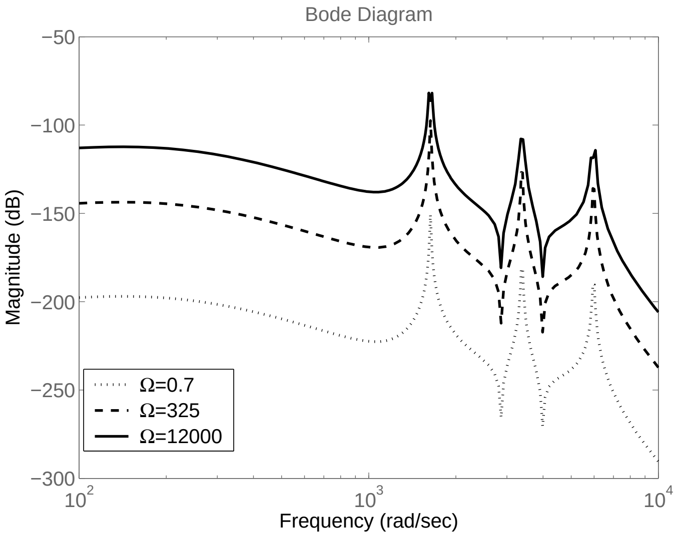

Figure 4.2: Comparison of the magnitude Bode plots of the system transfer function from first input ($i_{cx,\mathrm{A}}$) to second output (y_A), for different Ω in [rpm].

In addition, as one of the main objectives of this work is to utilize the high computational capabilities of the modern signal processing devices, high-order, high performance model-based controllers are examined. The inevitable question that arises is whether using such a complex control is justifiable and what are its advantages compared with low-order controllers. Another interesting issue is the practical implementation of such a complex control in real time, this however is addressed in Chapter 5.

Let us first examine, a priori, the features of a typical decentralized low-order controller, particularly, a PID-based controller:

- treats each pair of plant output and input as an independent subsystem, i.e., five decoupled SISO systems constitute the overall controller
- utilizes a low-order plant model and results in a low-order controller
- does not consider the gyroscopic effect, flexible modes, and plane coupling
- for highly gyroscopic systems, the unbalance response deteriorates with speed, e.g. according to Zhuravlyov (2000)
- employs direct output feedback
- provides the ease of application thanks to the low computational burden, and easily achieved high sampling rates
- requires manual tuning, often based on engineering judgment

The comparable features of the centralized, high-order controller, notably, LQ regulator (LQR) and the Kalman filter (LQ estimator) are:

- treats the plant as a single coupled MIMO system

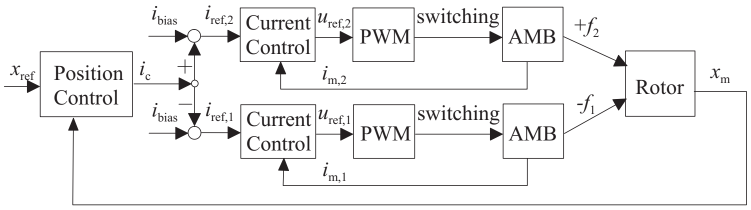

Figure 4.3: General control layout for a single DOF system

- utilizes a high-order plant model and results in a high-order controller
- requires an accurate and validated system model, i.e., high modeling effort
- employs state feedback and uses state estimation; non-measurable states have to be reconstructed by the controller
- faces difficulties in practical realization because of high computational burden, and sampling rate limited by the digital implementation
- uses automated procedures for the computation of optimal control gains, for the selected control layout

In addition, for the presented features, a high-performance controller would require some kind of adaptation to varying speed. In both the presented approaches, the controllers require a stability analysis. The decentralized controller uses the stability indices that are well-established in the control engineering. For SISO systems, these are: the gain and phase margins of the open-loop transfer function and the maximum peak magnitude of the sensitivity closed-loop transfer function. The design has to account for the bigger stability margins, required because of simplifying assumptions in the plant model. The centralized controller resorts to not so commonly used stability indices, such as maximal gains of the diagonal elements of the transfer matrix, and singular values. If only the more accurate plant model (or a suitable test setup) is available, also the multiple SISO controller should be tested like the MIMO system. Both controllers might require roll-off filters for high-frequency measurement signals due to the presence of the residual modes and noise. The mode-based controller that controls flexible modes trades in robustness for performance, when compared with the low-order PID controller.

As already mentioned in this work, we assume the cascaded control layout that consists of an inner and outer control loops. The currents in the actuators are controlled by the inner (internal, in regard to the external position control) current control loops. The displacements of the rotor from the central position are controlled by the outer (external, in regard to the internal current control) position control loop. The position controller provides the current controllers with the control currents (Fig. 4.3) to be followed as closely as possible. Therefore the inner current control loops have to have a higher bandwidth than the outer control loop. In the control system, a differential driving mode and a cascaded control scheme utilize fewer variables in the position controller, specifically, five control currents are used instead of ten reference currents, in ten electromagnets.

4.2 Current control loop

The principles of the current control are the same for the axial and radial bearings. A suitable background for the current control, namely the actuator dynamics, was described in subsection 3.3.3. The simple controller structure, as shown in Fig. 3.14, is sufficient for the inner current control. The controller consists of a proportional gain G_{P} and feedforward gain G_{F}, which produce the voltage reference used in the selected PWM scheme (section 2.3.2). The PWM results in an appropriate voltage applied to a coil, and more the coil current i is then generated according to the reference i_{ref}. Two reference currents for the opposite electromagnets are produced from one control current. The fast current feedback compensates variations in the coil inductance, and so the actuator is perceived as a linear one in respect of the dynamic inductance L_{dyn}. The feedforward gain compensates the effect of a resistive voltage drop Ri, non-idealities in the gate drivers, and the steady-state error due to PWM (e.g., caused by the digitization of the triangle carrier signals).

The control of the current is the control of the first order process with delay (Schneider, 1988). The control of such a processes is difficult when the time delay is long compared with the system time constant, or when the time delay varies. It is important to provide the internal current loop (3.49) robust, and insensitive to variations of parameters. As presented in Fig. 3.11, the variations of dynamic inductance L_{dyn} of the bearing are high. It is easier to judge the influence of these variations on (3.49) by taking derivatives with respect to plant dynamics, as

$$\frac{dG_{\mathrm{cl}}}{G_{\mathrm{cl}}} = \frac{1}{1 + G_{\mathrm{pl}} G_{\mathrm{P}}} \frac{dG_{\mathrm{pl}}}{G_{\mathrm{pl}}}, \tag{4.2}$$

where the G_{pl} is the transfer function of the plant. Therefore, the G_{cl} is relatively insensitive to variations in the process transfer function when $G_{\mathrm{pl}} G_{\mathrm{P}}$ is large, that is, the G_{P} is large and the modulation delay is short. As a matter of fact, in the system with reduced premagnetization current, the selection of the current feedback coefficient is a compromise between the fast control for current amplitudes below the bias, and the accuracy of the linearized model for the currents with higher amplitudes (used for the synthesis of the position control). The very high proportional gain creates a relatively more noisy bearing (because of the accuracy of measurements) with greater uncertainties (saturation of the actuator).

The switching frequency should be far above the control bandwidth. The selected PWM carrier frequency is 20 kHz (40 kHz switching rate). Also the premagnetization current was selected beforehand as $i_{\mathrm{bias}} = 2.5\,\mathrm{A}$. Assuming the first-order representation of the system (3.46), we can compute the current controller gains based on the required closed-loop time constant and resistance, as

$$G_{\mathrm{P}} = \frac{L}{\tau_{\mathrm{cl}}},\ G_{\mathrm{F}} = R, \tag{4.3}$$

where the time constant is determined by the expected rise time $\tau_{\mathrm{cl}} = t_{\mathrm{rise}} / \ln(9)$. This selection is somewhat arbitrary. One possible guidance is to compute the t_{rise}, using the current value between i_{bias} and i_{max}, with respect to the physical limits as in (3.51) or (3.50). This, however, results in the fast current control

Table 4.1: Bandwidth of the actuators, determined at the nominal air-gap, are summarized. The simulations for the radial and axial AMBs utilized the nonlinear models derived in subsection 3.3.3.

bandwidth [rad/s]	Radial AMB	Axial AMB
Assumed required position bandwidth	1634	–
ω_{cl} according to (3.49)	1845	1208
ω_{BW} for $i_{\max} = 5\,\mathrm{A}$ $^{(A)}$	3180, 1991	2440, 1272
ω_{BW} for $i_{\max} = 10\,\mathrm{A}^{(B)}$	1589, 1428, 1989	1220, –, 1041

$^{(A)}$ according to (3.51), and simulations

$^{(B)}$ according to (3.51), (3.54), and simulations

with the $\omega_{\mathrm{cl}} > \omega_{\mathrm{BW}}$, and the significant saturation in the control bandwidth. Instead, in the studied system, for the radial AMB, a good compromise is given by the selection of the gain based on the required bandwidth (with some safety margin), namely $G_{\mathrm{P}} = L{\cdot}1634{\cdot}1.1\,\mathrm{H/s}$. The axial AMB can be slower as only the rigid body modes are to be controlled and a wide bandwidth is not required. What is more, the narrower bandwidth prevents the actuator from exciting high frequency resonances, which may be associated with the axial bearing. Therefore, we select the bandwidth of the axial AMB current controller to be, for instance $\omega_{\mathrm{cl}} = \omega_{\mathrm{BW}} = 1208$ rad/s and the $G_{\mathrm{P}} = L \cdot 1208$ H/s.

The resulting dynamics of the actuators are summarized in Table 4.1. In the case of the radial AMB, we assume the bandwidth of the current control loop to be high enough, in order to actively control the first bending mode.

In the radial AMB with the proposed current control, for high signal amplitudes, the power bandwidth is slightly smaller than the controller bandwidth ($\omega_{\mathrm{BW}} < \omega_{\mathrm{cl}}$). The influence of the voltage saturation is small in the required control bandwidth, but the inductance, force-field nonlinearities, and hard nonlinearity due to the reduced premagnetization current are considerable. As a result, the force response in positive and negative direction, when not in the operating point, are not symmetrical. As an illustration, the frequency responses of the radial current closed-loop, for $x = 300\mu\mathrm{m}$, are presented in Fig. 4.4. The responses are plotted for the current amplitudes that are lower than the maximum current ($i_{\max} = 10\,\mathrm{A}$). The effect of the dynamic inductance could be compensated by applying the current- and displacement-dependent gain, in the control loop $G_{\mathrm{P}} = L_{\mathrm{dyn}}(x, i) \cdot 1/\tau$ (where $L_{\mathrm{dyn}}(x, i)$ is applied as a look-up table and piecewise linear interpolation). Such a compensation decreases the control system perturbations from the linear model. In particular, the phase is corrected to be equal to the one in the linear model. Albeit, the more significant is the error in the magnitude, which can be corrected by other methods (e.g., inverse nonlinearity as in Publication V). By visual inspection of the frequency responses of the compensated actuator in Fig. 4.5, it is apparent that the responses are improved, for negative and positive force ($x = 300\mu\mathrm{m}$ and $i < i_{\max}$).

The bandwidth of the radial AMBs, is high enough to actively control the first bending mode (determined in Chapter 3). However, in view of the coinciding location of the node of the first mode shape and the location of AMB (at the end-B of the rotor), this control is limited to the end-A. The control of the remaining high-frequency modes is not practical as the control system has

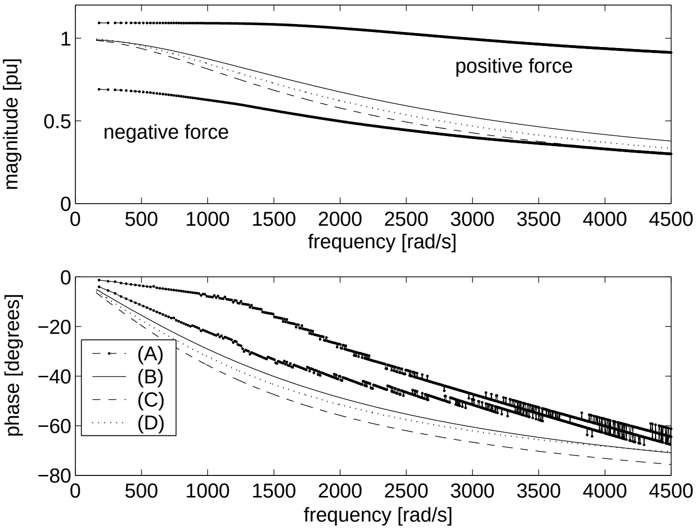

Figure 4.4: Frequency responses of the radial AMB model with the linear controller: (A) simulation of the nonlinear actuator model, (B) approximation based on (3.49), (C) approximation based on (3.54), (D) approximation based on (3.53).

limited sensing and actuation capabilities for these modes.

In the axial AMB, the power bandwidth is greater than or equal to the controller bandwidth ($\omega_{\mathrm{BW}} \geq \omega_{\mathrm{cl}}$) for maximum allowed signal amplitudes. The proposed current control is slower than the physical limit for $i_{\max} = 10\,\mathrm{A}$; and even though the reduced premagnetization current is used, the voltage saturation does not influence the closed-loop dynamics.

The comparison of the radial AMB actuator responses with different-order time-delay models is presented in Fig. 4.6. The applied current controller handles possible time-delay well enough, and therefore for the synthesis of a global position controller, in the approximation of the inner current control, the PWM delay could be neglected. On the one hand the accuracy of the control of flexible modes could be increased by applying high-order accurate model of the inner control loop, in the outer controller. On the other hand because of the variation of parameters, when the reduced premagnetization current is applied, the linear model accuracy is limited.

4.3 Force-field linearization

As already mentioned in Chapter 1, the major nonlinearity in the AMB control system is the force-field non-linear relation. A popular and convenient method for compensating actuators is that of inverse nonlinearities (INL).

4.3.1 Inverted nonlinear force field

In the INL method, to compensate the actuator nonlinearities, we introduce the force-field relation into the AMB controller as a look-up table and multivari-

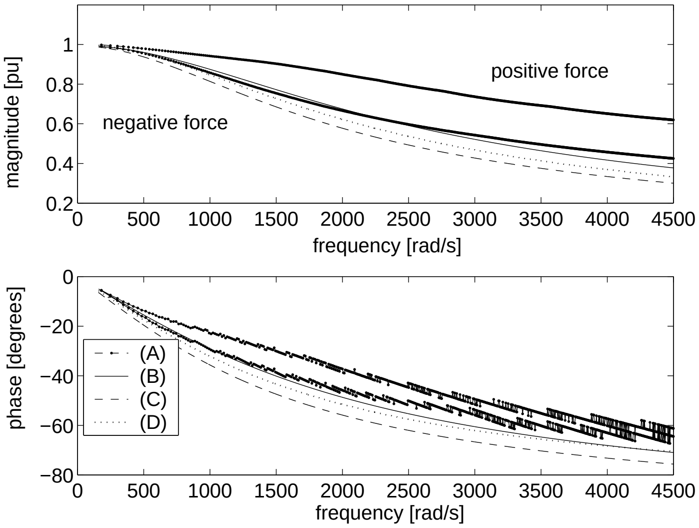

Figure 4.5: Frequency responses of the radial AMB model with the nonlinear controller (compensated L_{dyn} and the force field): (A) simulation, (B) approximation based on (3.49), (C) approximation based on (3.54), (D) approximation based on (3.53).

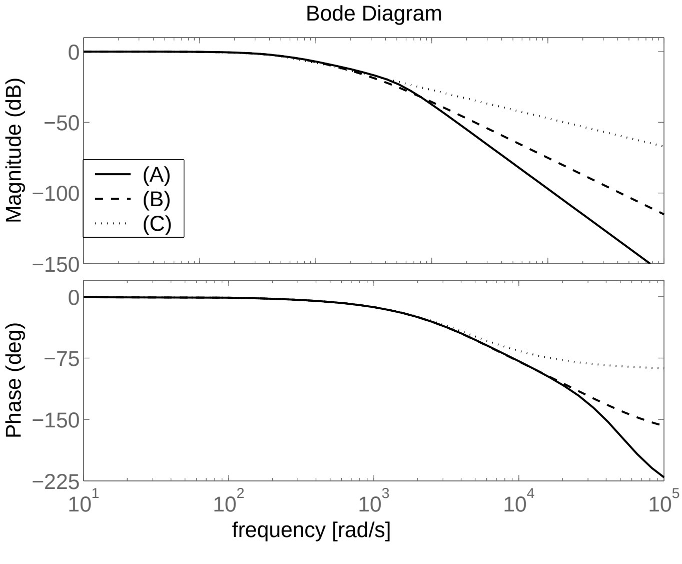

Figure 4.6: Bode diagrams of the closed-loop transfer function of the actuator for different approximations of the PWM delay (based on analytical model): (A) second-order delay, (B) first-order delay, (C) no delay. The maximal delay, which is twice as long as the average modulation delay, was used in the simulations. For the selected carrier frequency, the influence of the delay (in the control bandwidth) is insignificant.

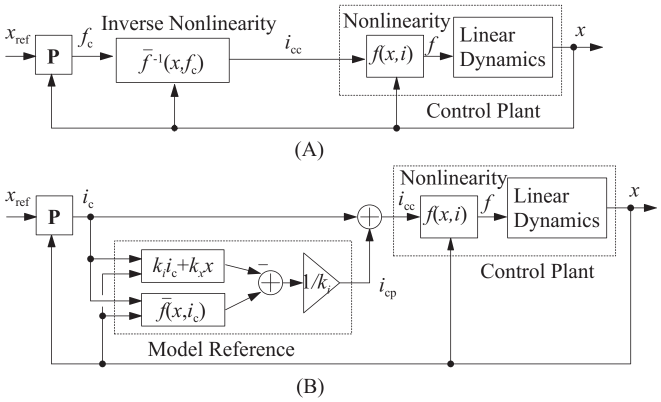

Figure 4.7: Principle of the INL compensation method (A), and the principle of the model reference method (B)

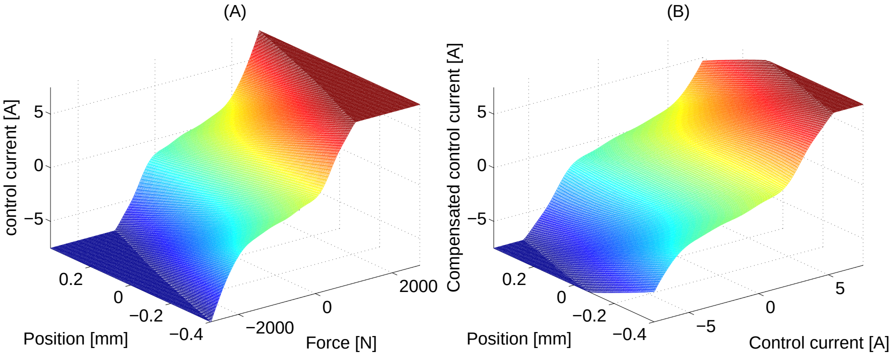

Figure 4.8: Inverted relation (A) of the force-current-displacement characteristics from Fig. 3.10 and the compensating surface (B), are presented. The surfaces were built for the radial AMB as in Table B.1.

able interpolation. The INL compensation principle is presented in Fig. 4.7A. Let us assume that we want to compensate the force generated by the pair of the opposite electromagnets. First, the inverted relation of the force-current-displacement characteristics (Fig. 4.8A) is determined and stored in the look-up table. The value of the control current can be obtained from the table of stored values with force and position as the table entries. The closest entry or other various types of interpolations can be used. When the compensation of the nonlinear actuator is directly incorporated into the controller, the control input becomes force instead of current, and the position stiffness is canceled out from the closed-loop system dynamics.

It is also possible to apply the compensation of the actuator as a single look-up table with the entries (x, i_c), such that there are no changes in the upper control. This is realized by first computing the force reference from (2.14), and second by combining the reference force with the inverted nonlinearity into one compensation surface shown in Fig. 4.8B.

In most cases, it is more convenient to compensate the force generated by the pair of the opposite electromagnets than to compensate the forces generated by the single electromagnet. Albeit, both approaches are equivalent. It is important to notice that force-field compensation is accurate for the static signals. As an example, it cannot fully compensate the actuator nonlinearities for high-frequency signals and high signal amplitudes, when only one electromagnet is active (Fig. 4.5), to say nothing of the saturation.

4.3.2 Model reference method

An alternative solution for the actuator linearization, which can directly utilize the force characteristics (nonlinearity do not has to be inverted) and it is applied parallel with the existing controller, is the approach named here as the model reference method. The intrinsic idea of this solution is a comparison between the linear and nonlinear reference approximations as shown in Fig. 4.7. In the studied case, the control current and rotor displacement are utilized in computation of the electromagnetic forces. The forces are calculated using both the linearized and interpolation-based nonlinear bearing models. The difference between these two forces is employed in a feedforward control manner as a compensation current. As to the force-field compensation in AMB, the practical realization can be reduced to a single look-up table as with the INL method.

The presented method can be shown to be equivalent to the INL method. In the application of the INL method to an AMB actuator, when using the conventional controller with the control output in the form of the control current, the compensated control current i_{cc} equals the control current plus the compensation current, that is $i_{\mathrm{cc}} = i_{\mathrm{c}} + i_{\mathrm{cp}}$. The compensation current can be expressed as

$$i_{\mathrm{cp}} = \frac{k_i - k_i^* \left(x,\, i_{\mathrm{cc}}\right)}{k_i^* \left(x,\, i_{\mathrm{cc}}\right)} i_{\mathrm{c}} + \frac{k_x - k_x^* \left(x,\, i_{\mathrm{cc}}\right)}{k_i^* \left(x,\, i_{\mathrm{cc}}\right)} x, \tag{4.4}$$

where k_i^* and k_x^* are the current stiffness and position stiffness dependent on the position and compensated control current (the values of the coefficients without the star are equal to the nominal values). When k_i^* in the denominator of Eq. (4.4) is replaced by the constant nominal current stiffness, the compensation current becomes equal to the compensation current from the model reference method with the feedforward gain equal to $1/k_i$.

In the case of the compensation based on a control current (compensation of the force generated by the pair of the electromagnets), the INL is more accurate than the model reference method. However, the model reference method is more generic and easier to apply.

The benefits and trade-offs of both compensation methods along with system responses with and without compensation can be found in Publication V. Figure 4.9 shows the position responses for the impulse external disturbance of the system with and without the INL compensation. The disturbance was equivalent to the point mass of about 3 kg falling on the rotor from the height of 12 cm. The advantage of the compensated control over the non-compensated one is apparent in smaller position deviation from the reference point but in expense of the slightly greater currents.

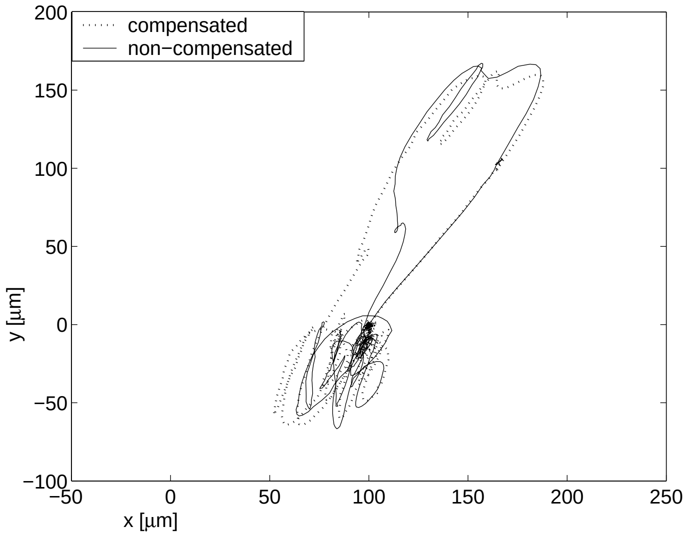

Figure 4.9: Position responses for the impulse external force of the compensated and non-compensated control systems

4.4 PID-based position control

In many AMB applications, under certain conditions (rigid rotor, not-reduced premagnetization current in bias linearization, and small interactions between control channels), an AMB rotor suspension might be considered as a linear decentralized plant. The PID-based control is a well-established and still commonly used control method in many industrial applications. As a result of this, PID-based controllers are typically utilized for the control of a multiple SISO AMB rotor suspension (Lösch 2002, Schweitzer et al. 2003, Polajzer et al. 2006, and many others). Therefore, in this work, it is used as a reference design for the developed LQ-model-based control.

In particular, the approach presented by Lösch (2002) and Polajzer et al. (2006) that results in a PID-like controller, with an additional first-order filter (or a lead compensator with an integral) is adopted. For the rotor considered in (3.1) and for ideal actuation, the plant is $G(s) = k_i/(ms^2 - k_x)$. Stabilization is achieved by the controller with the transfer function

$$G_{\mathrm{ld}}(s) = G_{\mathrm{P,ld}} \left(\frac{\tau_{\mathrm{ld}} s + 1}{a_{\mathrm{ld}} \tau_{\mathrm{ld}} s + 1} + \frac{a_{\mathrm{I}}}{s \tau_{\mathrm{I}}} \right), \; \tau_{\mathrm{ld}} = \frac{1}{\sqrt{a_{\mathrm{ld}}} \omega_{\mathrm{ld}}}, \tag{4.5}$$

where $G_{\mathrm{P,ld}}$, τ_{ld}, ω_{ld}, a_{I}, and τ_{I} denote the lead compensation gain, the time constant, the frequency of the maximum phase lift, the integral term gain scale, and the integral time constant. The parameter a_{ld} can be determined by the expected maximum phase lift ϕ of the compensator, that is $a_{\mathrm{ld}} = (1 - \sin(\phi))/(1 + \sin(\phi))$. The stability conditions, when assuming the lead compensation alone and using the Hurwitz criterion, can be derived as in A.6, and they are

$$0 < a_{\mathrm{ld}} < 1, \; G_{\mathrm{P,ld}} > \frac{k_x}{k_i}. \tag{4.6}$$

The gain $G_{\mathrm{P,ld}}$ can be determined, for the selected a_{ld}, ω_{ld} (e.g., according to guidance given by Lösch (2002), $a_{\mathrm{ld}} = 0.15$ and $\omega_{\mathrm{ld}} = 15 \cdot \sqrt{k_x/m}$), using the root locus. The a_{I} and τ_{I} are selected as the arbitrary parameters, and then the stability of the system is verified.

Furthermore, as shown by Polajzer et al. (2006), it is beneficial to use a cascade connection of PI and PD controllers. The major advantages of this control over the conventional PID are a high closed-loop damping and stiffness. In such a solution, stabilization is achieved by the cascade connection of the lead compensator (i.e., $G_{\mathrm{ld}}(s)$ similar as in (4.5) but without integral term $a_{\mathrm{I}} = 0$) and the PI controller $G_{\mathrm{pi}}(s)$, in the inner and outer position control loops, respectively. The transfer function of the PI controller is

$$G_{\mathrm{pi}}(s) = G_{\mathrm{P,pi}} \left(\frac{\tau_{\mathrm{I}} s + a_{\mathrm{P}}}{\tau_{\mathrm{I}} s} \right), \; \tau_{\mathrm{I}} > \tau_{\mathrm{ld}}, \tag{4.7}$$

where a_{P} and $G_{\mathrm{P,pi}}$ are the proportional term gain scale, and the overall PI term gain, respectively. In order to ensure reasonable damping of the conjugate-complex poles, resulting from the lead compensation, the added integral pole should be dominant, specifically the integral time constant should be selected to be greater but close to the lead compensator time constant. Then, the PI term gain can be chosen using the root locus.

4.5 SISO case LQ position control

In the design of the position control loop, we consider the LQR, the Kalman filter as an estimator, and numerical approach using Matlab. The analytical solutions for an optimal 1-DOF and 5-DOF AMB controllers is given by Zhuravlyov (2000), who also considers an optimal actuation, with respect to the ohmic losses, that results in the external linearization driving mode (only one electromagnet, from one pair, is working at the time).

The application of the LQ-control design to the AMB rotor system is presented in Publications IV and V. With this in mind, the presentation in this section is complementary to those previous results and it focuses on the aspects that extend the material presented in the publications.

4.5.1 Selection of optimal control layout

We are looking for a simple state-variable model and a LQ-method-based control, which would fulfill the objectives of subsection 4.1.3. In the whole procedure, we compute the optimal state feedback law, concatenate it with the Kalman filter for the plant state estimation, and obtain the output feedback controller.

For the multivariable, time-invariant, and time-continuous plant model (3.60), the estimator is formed as

$$\dot{\bar{\mathbf{x}}} = \boldsymbol{A}\bar{\mathbf{x}} + \boldsymbol{B}\mathbf{u} + \boldsymbol{L}\left(\mathbf{y} - \bar{\mathbf{y}}\right), \; \bar{\mathbf{y}} = \boldsymbol{C}\bar{\mathbf{x}}, \tag{4.8}$$

where $\bar{\mathbf{x}}$, $\bar{\mathbf{y}}$, and $\boldsymbol{L}$ are the estimate of the full state vector $\mathbf{x}$, the estimate of the output vector $\mathbf{y}$, and the proportional estimator gain matrix that provide satisfactory error characteristics, respectively. The estimator gain matrix is obtained from the steady-state solution of the Riccati equation. We decide to apply the full state estimation, as, in general, it provides good control behavior and filtering of the position measurements (Schweitzer et al., 2003). The state feedback control is then obtained as

$$\mathbf{u} = -\boldsymbol{K}\bar{\mathbf{x}}, \tag{4.9}$$

where $\boldsymbol{K}$, is the proportional state feedback gain matrix that is also obtained from the solution of the Riccati equation, based on the selection of the cost weights in the LQ criterion.

Since we want to eliminate the steady-state errors (they are caused by disturbances, external reference commands, and variations in the plant parameters), which may effectively decrease the system performance, we include an integral action in the controller. Initially, we examine two options for the integral action, namely an augmented state integral in the state feedback and a constant disturbance estimation. If the integral $\mathbf{x}_\mathrm{I}$ is present in the system, the computation of the gain state feedback matrix $\boldsymbol{K}$ and the integral feedback gain matrix $\boldsymbol{K}_\mathrm{I}$, may be based on the augmented plant model

$$\begin{bmatrix} \dot{\mathbf{x}}_\mathrm{I} \\ \dot{\mathbf{x}} \end{bmatrix} = \begin{bmatrix} \boldsymbol{A}_\mathrm{I} & \boldsymbol{C} \\ \mathbf{0} & \boldsymbol{A} \end{bmatrix} \begin{bmatrix} \mathbf{x}_\mathrm{I} \\ \mathbf{x} \end{bmatrix} + \begin{bmatrix} \mathbf{0} \\ \boldsymbol{B} \end{bmatrix} \mathbf{u}, \tag{4.10}$$

where $\boldsymbol{A}_\mathrm{I}$ defines the integral model dynamics. Similarly, if the constant disturbance estimate $\bar{\mathbf{x}}_\mathrm{dist}$ is utilized in the system, the computation of the proportional gain matrix $\boldsymbol{L}$ and the disturbance estimator gain matrix $\boldsymbol{L}_\mathrm{dist}$ may be based on the augmented plant model

$$\begin{bmatrix} \dot{\mathbf{x}} \\ \dot{\mathbf{x}}_\mathrm{dist} \end{bmatrix} = \begin{bmatrix} \boldsymbol{A} & \boldsymbol{B} \\ \mathbf{0} & \boldsymbol{A}_\mathrm{dist} \end{bmatrix} \begin{bmatrix} \mathbf{x} \\ \mathbf{x}_\mathrm{dist} \end{bmatrix} + \begin{bmatrix} \boldsymbol{B} \\ \mathbf{0} \end{bmatrix} \mathbf{u}, \tag{4.11}$$

where $\boldsymbol{A}_\mathrm{dist}$ defines the disturbance model dynamics. In this case, the $\boldsymbol{A}_\mathrm{I} = \boldsymbol{A}_\mathrm{dist} = \mathbf{0}$ in the implementation. However, in order to be able to obtain a required integration time constant we have to introduce the first order dynamics into the integral and disturbance models (e.g., $\boldsymbol{A}_\mathrm{I} = \boldsymbol{A}_\mathrm{dist} = 1/\tau_\mathrm{I}$, where τ_I is roughly the expected integration time constant). The $\mathbf{x}_\mathrm{I}$ and $-\bar{\mathbf{x}}_\mathrm{dist}$ are applied to the plant control input. The integrals of the error signals are

$$\dot{\mathbf{x}}_\mathrm{I} = \boldsymbol{K}_\mathrm{I} \left(\mathbf{x}_\mathrm{ref} - \mathbf{y} \right), \, \dot{\bar{\mathbf{x}}}_\mathrm{dist} = \boldsymbol{L}_\mathrm{dist} \left(\mathbf{y} - \bar{\mathbf{y}} \right), \tag{4.12}$$

where $\mathbf{x}_\mathrm{ref}$ is the reference input vector.

The classical state-space methods (Franklin et al., 1998, Åström and Wittenmark 1997) provide different alternatives, even for a simple control layout (location of a reference input, applying the integral or the disturbance estimate).

First, recalling the objectives form subsection 4.1.3, in regard to the servo problem, the most crucial point is the rotor lift up from the retainer bearings to the operating point. At these starting conditions, the nonlinearities are at highest and the rotor is initially bent. Otherwise, there are no special servo requirements for the system. Therefore, a straightforward reference input state command structure is selected. In the state command structure (Fig. 4.10), the same inputs are applied to the estimator and to the plant, thus minimizing estimation error. Another advantage of the state command reference input, over the typically applied one for the transfer functions – the output error command

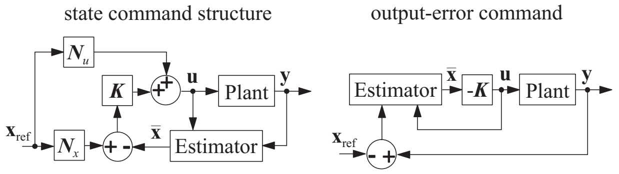

Figure 4.10: Reference input structures (Franklin et al., 1998)

scheme, is a faster response with the less control usage. The suitable matrices of the feedforward input $\boldsymbol{N}_u$ and the reference command input $\boldsymbol{N}_x$ are computed from the steady-state requirements for the system (Franklin et al., 1998), as

$$\begin{bmatrix} \boldsymbol{N}_x \\ \boldsymbol{N}_u \end{bmatrix} = \begin{bmatrix} \boldsymbol{A} & \boldsymbol{B} \\ \boldsymbol{C} & \mathbf{0} \end{bmatrix}^{-1} \begin{bmatrix} \mathbf{0} \\ \mathbf{I} \end{bmatrix}. \tag{4.13}$$

Second, a state-space control layout suitable for AMB application is selected. We briefly test four variants of the controller, which examine the different integral utilization. The considered state-space controller layouts are as follows (according to Fig. 4.11):

1. The integral control with a reference input state command structure, where integral replaces the $\boldsymbol{N}_u$, is employed; only the state estimation (no constant disturbance estimate: $\boldsymbol{L}_{\text{dist}} = \mathbf{0}$) is used.
2. The integral control $1/s \cdot \boldsymbol{K}_{\text{I}}$ is replaced by the $\boldsymbol{N}_u$, but the state estimator is complemented by the classical constant disturbance estimator (that applies the $\bar{\mathbf{x}}_{\text{dist}}$ to the plant input).
3. Both integral actions are present in the system (the integral control as a feedforward input and the constant disturbance estimator); no state command is present.
4. As in point 3, but the disturbance estimate vector is fed to the state estimator inputs instead of the plant inputs.

The results of a comparative simulation of the axial suspension, with the state-space controllers structured according to points 1-4, are presented in Fig. 4.12. The cost weights, disturbance properties, and error characteristics are the same for the synthesis of all the controllers. With the first variant, no steady-state errors are present; however, there are errors in the estimated states caused by the external disturbances. The response to the reference input is as fast as the maximum current limit is able to provide, and yet, there appears a slight overshoot (and the over current) due to the added integral pole. In fact, this can be tackled (in a SISO system) by adjusting the system zero to cancel the integrator pole s_{I}, as $\boldsymbol{N}_x = -\boldsymbol{K}_{\text{I}}/s_{\text{I}}$. With the second variant, the estimation error is very well minimized by the fast constant disturbance estimator; and in addition, the response to the step disturbance force is improved. During the step reference input, the control current is close to, but below, its maximal allowed value. In the third and fourth variants, the servo properties rely only on the integral placed at the reference input. With the third variant, the use

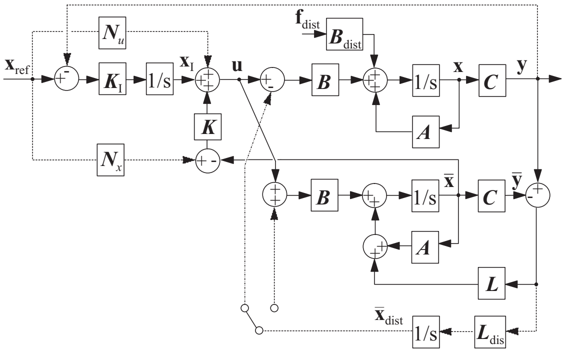

Figure 4.11: Generalized optimal state-space based controller layout is presented. The connections that differ according to the variants 1-4 are marked with dashed lines. The vector of disturbance forces $\mathbf{f}_{\text{dist}}$ enters the plant through the disturbance input matrix $\boldsymbol{B}_{\text{dist}}$ (external force applied directly to the rotor). The constant disturbance estimate is scaled so that it is given in amperes.

of the integrators (in the reference input and in the estimator) might result in the interference between two integral control actions in the system. This can be observed in the response to the step disturbance, that is, the overshoot appears, and when the integral time constant is even smaller, there might appear small oscillations. With the fourth variant, this behavior is improved.

The maximum tolerated force depicted in Fig. 4.12C is the minimum of the disturbance forces, which yield the maximum allowed displacement or the maximum control current. The physical force limit equals to the sum of the inertial force $(1/(ms^2 - k_x))^{-1}x_{\max}$ (the force necessary to vibrate the rotor mass) and the dynamic bearing force. The position bandwidth $\omega_{\text{BW}} = 295\,\text{rad/s}$; and it is the frequency at which the inertial force equals the maximum bearing force (Lantto, 1999).

On the one hand the systems with the integral action in the reference input are less sensitive to variations in a plant parameters (improving the servo properties), but on the other hand in the studied case, the servo properties are important only at the start-up. Considering the maximum tolerated disturbance force, all the tested schemes provide satisfactory disturbance rejection. In regard to these observations and by using the minimization of the estimation error for a main selection criteria, we select the second variant as the suitable and straightforward solution.

4.5.2 Selection of optimal weighting matrices

In the AMB control system, the physical limitations such as: maximum bearing forces, expected disturbance forces, displacements, currents, and voltages point at the formulation of the control strategy as an LQ optimization problem to minimize the values of control variables with minimum control effort. The LQ optimal control guarantees a desirable high-performance, stable control, and eases the design of MIMO systems by reducing the degrees of freedom in the design iterations. However, it requires an accurate plant model, accurate measurements, and estimation of non-measurable states. Building the accu-

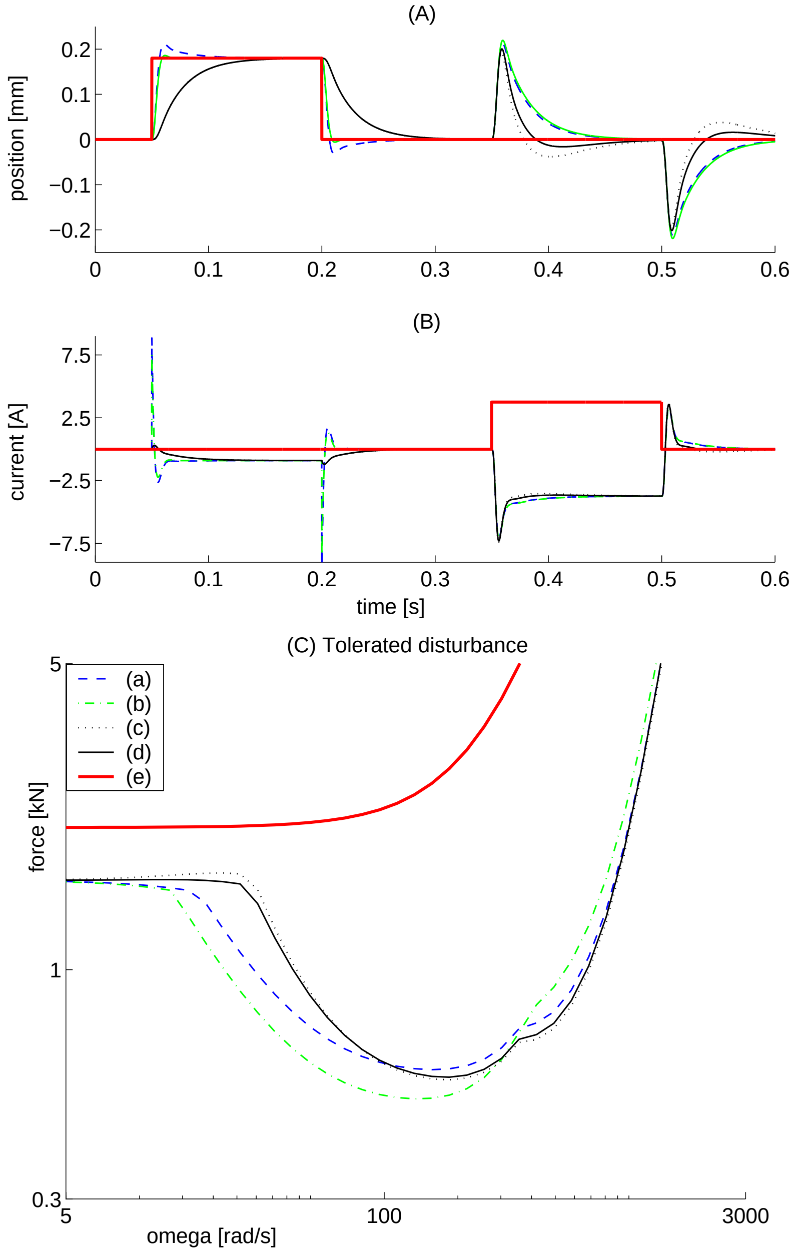

Figure 4.12: Comparative simulations of the axial suspension, with the state-space controllers structured according to points 1-4, are presented. In the top two illustrations (A-B), the step responses of the systems with different controllers, to the reference input and disturbance force are shown. In the bottom illustration (C), the maximal tolerable disturbance forces of the closed-loop systems, as functions of frequency, are plotted. The plots (a-d) correspond to the axial suspension with the controllers 1-4, respectively. The plots (e) correspond to the reference displacement, disturbance force scaled by the inverse of the current stiffness, and physical force limit, in the top, middle, and bottom illustration, respectively.

rate plant model is addressed in Chapter 3 and, fortunately, the Kalman filter provides the necessary estimates and filters noisy measurements based on the specified error characteristics of the system inputs and outputs.

Regarding the plant, we assume that the pair ($\boldsymbol{A}$, $\boldsymbol{B}$) is controllable and that the pair ($\boldsymbol{A}$, $\boldsymbol{C}$) is observable. For LQR used for AMBs, some authors (e.g. Lösch, 2002) point a drawback in the trial and error of design procedure, namely, the selection of weighting matrices. In fact, there are at least two practical design methods for LQ control, which address this issue: Bryson's rules presented for instance by Franklin et al. (1998), Lewis and Syrmos (1995), and the method based on the asymptotic modal properties of LQR given by Hiroe et al. (1993). Owing to the straightforward design and good results, Bryson's rules are selected for utilization in the optimal controller synthesis.

The procedure for designing the LQ controller is as follows. In the LQR, the state-feedback controller gain matrices $[\boldsymbol{K}_{\mathrm{I}}\, \boldsymbol{K}]$ minimize the quadratic integral performance index J_{q}, and the diagonal matrix $\boldsymbol{C}_{\mathrm{si}}$ selects which states should be kept under close regulation, as

$$J_{\mathrm{q}} = \int_0^{\infty} \left[\mathbf{x}^{\mathrm{T}}\boldsymbol{Q}\mathbf{x} + \mathbf{u}^{\mathrm{T}}\boldsymbol{R}\mathbf{u} + 2\mathbf{x}^{\mathrm{T}}\boldsymbol{N}\mathbf{u}\right] dt, \tag{4.14}$$

$$\boldsymbol{Q} = \boldsymbol{C}_{\mathrm{si}}^{\mathrm{T}}\bar{\boldsymbol{Q}}\boldsymbol{C}_{\mathrm{si}}, \tag{4.15}$$

where $\boldsymbol{Q}$, $\bar{\boldsymbol{Q}}$, $\boldsymbol{R}$, and $\boldsymbol{N}$ are the scaled and the unscaled state weighting matrix, control weighting matrix, and the weighting matrix responsible for the cross effect between the state and control, respectively. The weighting is arbitrary but the problem data must satisfy certain limiting conditions when solved with the Matlab (see The Math Works Inc. 1999).

Similarly, the optimal estimator gain matrices $[\boldsymbol{L}\, \boldsymbol{L}_{\mathrm{dist}}]^{\mathrm{T}}$ are determined by solving an algebraic Riccati equation based on the noise intensity matrix $\boldsymbol{R}_v$ of the sensors and the process input noise intensity matrix $\boldsymbol{R}_w$. These covariance matrices are formed based on the rms accuracy of the position measurements and control inputs. For the state estimator, the optimal solution of the Kalman filter is

$$\dot{\bar{\mathbf{x}}} = \mathbf{A}\bar{\mathbf{x}} + \mathbf{B}\mathbf{u} + \mathbf{L}\left(\mathbf{y} - \mathbf{C}\bar{\mathbf{x}} - \mathbf{D}\mathbf{u}\right). \tag{4.16}$$

The error characteristics of the position measurement are influenced by the accuracy of the sensors, their sensitivity to external electromagnetic interferences, the non-ideal rotor surface (runout), and presence of unmodeled dynamics. If $\boldsymbol{R}_v$ increases, the stability and peak disturbance force rejection decrease. The error characteristics of the control inputs differ considerably, depending on how well the system (and especially actuator) is linearized and modeled.

Let us consider the selection of the weighting matrices for design of the axial AMB controller. Now, assuming the layout variation as in subsection 4.5.1, the matrices are selected as follows. In the LQR, the states, which correspond to the position error integral, control current, position, and velocity are scaled by the square of their maximum allowed values as

$$\bar{\boldsymbol{Q}} = \mathrm{diag}\left[1/x^2{}_{\mathrm{max}},\, 1/i^2_{\mathrm{c,max}},\, 1/x^2_{\mathrm{max}},\, 1/v^2_{\mathrm{max}}\right], \tag{4.17}$$

and likewise the control effort is scaled as $\boldsymbol{R} = 1/i^2_{\mathrm{c,max}}$. The $\boldsymbol{N} = \mathbf{0}$. In the similar manner, in the LQ estimator, the initial covariance matrices are selected as $\boldsymbol{R}_v = (0.1 \cdot x_{\mathrm{max}})^2$, $\boldsymbol{R}_w = (0.5 \cdot i_{\mathrm{c,max}})^2$. These matrices are selected in such

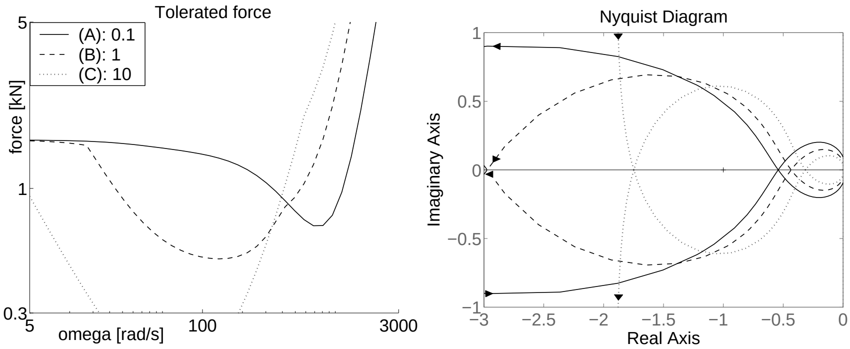

Figure 4.13: Selecting weight of the position state, e.g. for (A) $1/(0.1 \cdot x_{\max})^2$ the stiffness is at highest

a way that there are certain safety margins between the actual error characteristics (the rms accuracy of the position measurements and the rms accuracy of the control inputs), and the assumed stochastic properties (of the process and measurement noise), otherwise they are used as the design parameters. Furthermore, the integral state (if present), control current, and rotor position are kept under the close regulation ($\boldsymbol{C}_{\mathrm{si}} = [1\,1\,1\,0]$). Leaving the current control to the inner control loop ($\boldsymbol{C}_{\mathrm{si}} = [1\,0\,1\,0]$) would increase the system performance in terms of the tolerated disturbance force, but on the slight expense of the stability. The weighting of the state related to the displacement contributes mostly to the bearing stiffness (roughly 2-3 times as much as to the bearing damping), and the weighting of the state related to the velocity contributes mostly to the bearing damping (Fig 4.13 and 4.14). The smaller the allowed maximum position and velocity, the bigger the resulting stiffness and damping. The assumed maximum velocity, in the weight, equals to the velocity of the rotor that is accelerated from its central position to $x_{\max}$ when applying the maximum bearing force. Increasing the available control effort in $\boldsymbol{R}$, increases both the bearing stiffness and damping (4.15). In the case of the unbiased estimator, the gain computation is based on the augmented plant model, where the disturbance model is $\boldsymbol{A}_{\mathrm{dist}} = 1/\tau_{\mathrm{I}}$. If τ_{I} decreases, the peak-tolerated-force increases considerably (as a trade-off between low- and high-frequency forces), but in expense of the stability margins. The effect of the integral time constant is compared in Fig 4.16.

The poles of the estimator become faster when the ratio of $\boldsymbol{R}_w/\boldsymbol{R}_v$ increases. The most straightforward way to increase the stability margins of the LQ design is to increase the noise rms values in the process covariance matrix $\boldsymbol{R}_w$ (Fig 4.17). This way, the estimator poles are faster than the controller poles, but the system becomes more noise sensitive.

There exist a trade-off between low and high frequencies when selecting the weighting matrices in regard to the performance and tolerated disturbance forces. In most cases the weights that result in a control system that tolerates the disturbances at low frequencies at the same time decrease the tolerated disturbances at high frequencies. Low tolerated disturbances at high frequencies indicate high open-loop gains for frequencies above the crossover frequency and deficient robust stability margins.

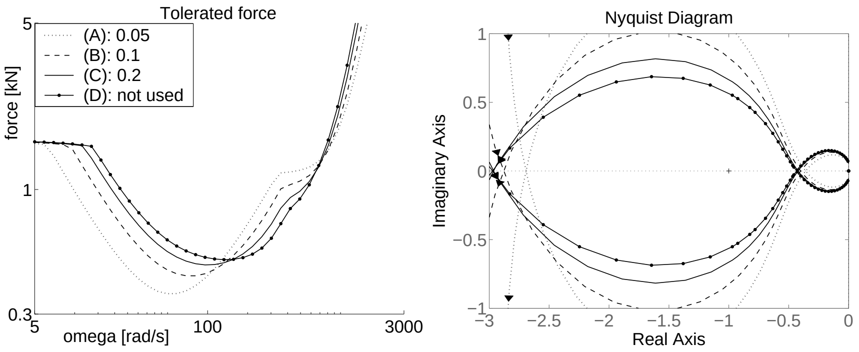

Figure 4.14: Selecting weight of the velocity state, e.g. for (A) $1/(0.05 \cdot v_{\max})^2$ the damping is at highest

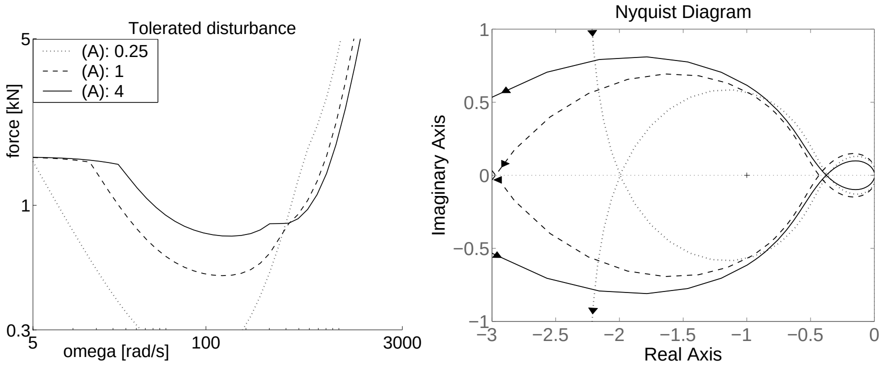

Figure 4.15: Selecting weight of the control effort, e.g. for (A) $\boldsymbol{R} = 1/(0.25 \cdot i_{\mathrm{c,max}})^2$ the stiffness and the damping are at lowest

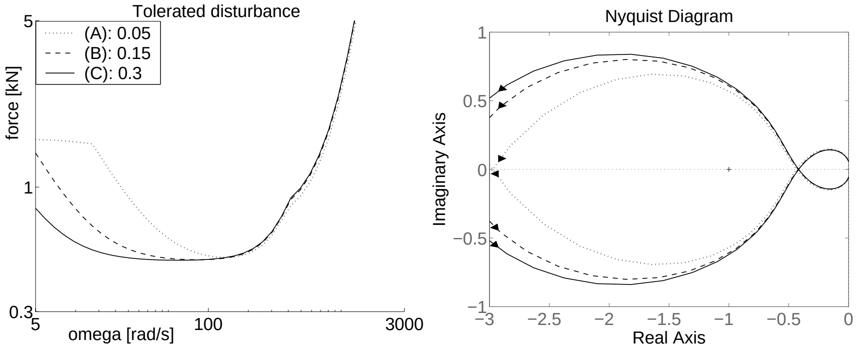

Figure 4.16: Selecting disturbance model, e.g. for (A) $\boldsymbol{A}_{\mathrm{dist}} = 1/(0.05)$

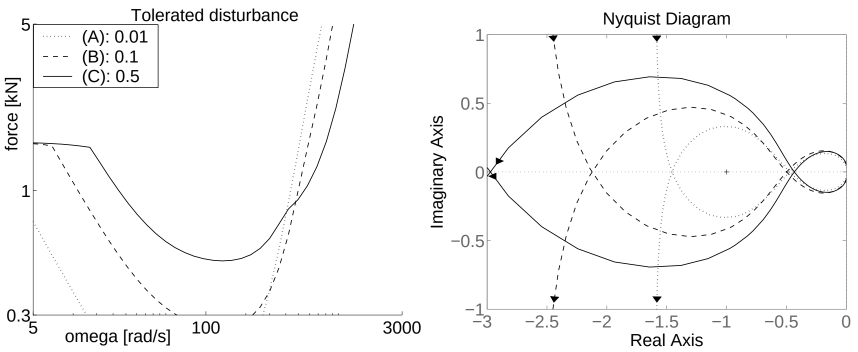

Figure 4.17: Selecting the covariance matrix, i.e. for (A) $\boldsymbol{R}_w = (0.01 \cdot i_{\mathrm{c,max}})^2$

Table 4.2: Parameters in the design of the axial LQ controller

$\boldsymbol{Q} = \mathrm{diag}\left[1/i^2_{\mathrm{c,max}},\ 1/x^2_{\mathrm{max}},\ 0\right],\ \boldsymbol{R} = 1/i^2_{\mathrm{c,max}},$
$\boldsymbol{C}_{\mathrm{si}} = [1\,1\,0],\ \boldsymbol{R}_w = (0.5 \cdot i_{\mathrm{c,max}})^2,\ \boldsymbol{R}_v = (0.1 \cdot x_{\mathrm{max}})^2,$
constant disturbance estimator $\boldsymbol{A}_{\mathrm{dist}} = 1/(0.3)^{(\mathrm{A})}$

$^{(\mathrm{A})}$ The $\boldsymbol{A}_{\mathrm{dist}} = 1/(0.05)$ in Fig. 4.12, 4.17, and 4.15.

Finally, after some iterations, the selected parameters of the axial controller are presented in Table 4.2. The control system tolerates a gain drop and increase by the factor of 0.29 (at 37 rad/s) and 2.4 (at 915 rad/s), respectively. The phase margin is 32°, at 383 rad/s.

In the case of the LQ control and considerable actuator delay, the actuator model with a approximated delay should be included in the plant model (increases the number of states in an estimator), otherwise it may reduce the stability margins and system performance. The reduced bias current adds not only the plant uncertainties owing to its changeable dynamics that are dependent on the signal amplitude and frequency, but also influences the achievable maximum tolerated disturbance force, as shown in Fig. 4.18A. In addition, in Fig. 4.18B, the stability of the axial suspension with the derived controller, as a function of k_x and k_i, is examined. Figure 4.18B is obtained by iterating over the values of k_x and k_i, and verifying the stability of the system in each iteration.

4.5.3 Comparison of LQ and PID controllers

In order to compare the LQ- and PID-based controllers, the tolerated disturbance force and the magnitude of the complementary output sensitivity function (measured position to reference signal, i.e. see A.7) of different control systems are examined in Fig. 4.19. The LQ controller has a smaller integral gain than the PID-based controllers; therefore it better tolerates high-frequency disturbances. We observe that, in the plot of the complementary sensitivity, the LQ control yields the optimal servo properties, while the PID gives overshoot and the PI/PD cascade has a limited bandwidth. Moreover, as presented in Fig. 4.20, the step response of the both PID-based control systems exhibit overcurrent. The parameters of the PID structure as in (4.5) and the PI/PD cascade struc-

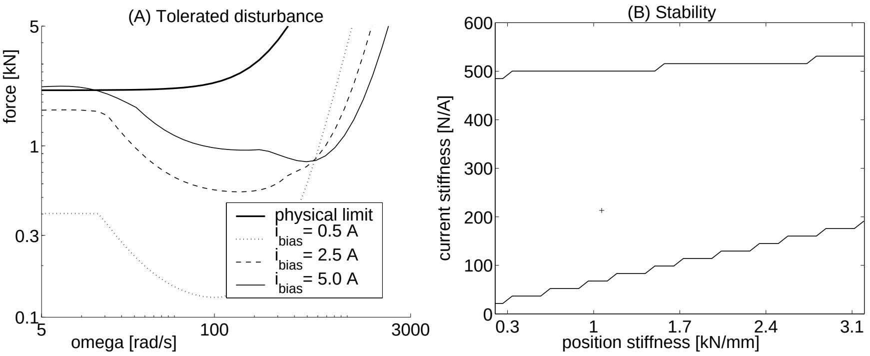

Figure 4.18: In the left-hand illustration, the influence of the bias current on the tolerated disturbance force of the closed-loop axial suspension is presented. In the right-hand illustration, the stability of the system in function of k_x and k_i is presented. The nominal values of the k_x and k_i are indicated with a plus sign, in the stable region.

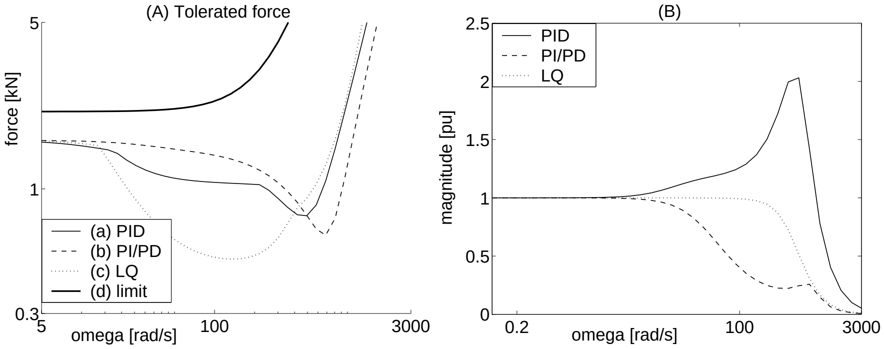

Figure 4.19: In the left-hand illustration, the tolerated disturbance force is presented. In the right-hand illustration, the output complementary sensitivity of the different control systems, is shown.

ture, used in the comparison, are gathered in Table 4.3. The LQ controller is a design based on the final selection of weights given in subsection 4.5.2.

4.6 MIMO case position control

In the described SISO feedback, the state regulator is in fact equivalent to a PD control, which introduces a mechanical stiffness (P-part) and differential damping (D-part) to the system. In a MIMO case, the regulator features not only the PD properties, but it also captures the inertial connections between the end-A/end-B, gyroscopic connections between the (x, z) and (y, z) planes. Furthermore, the presented design of an LQ regulator/estimator takes into account the flexible modes and their controllability. In addition, it somewhat automates the design replacing manual control pole placement with the proper weight selection.

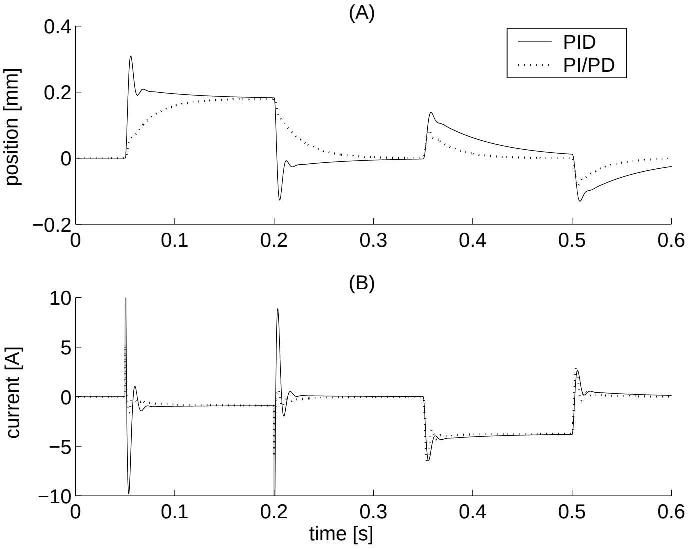

Figure 4.20: Position (subfigure A) and control current (subfigure B) responses, of two control systems, for the step position reference and disturbance force, are presented.

Table 4.3: Controller parameters

	PID	PI/PD
gain	$G_{\mathrm{P,ld}} = 3.4e4$	$G_{\mathrm{P,ld}} = 4.3e4$, $G_{\mathrm{P,pi}} = 0.1$
time constant	$\tau_{\mathrm{ld}} = 1/\left(\sqrt{a_{\mathrm{ld}}}\omega_{\mathrm{ld}}\right)$, $\tau_{\mathrm{I}} = 0.15$	$\tau_{\mathrm{ld}} = 1/\left(\sqrt{a_{\mathrm{ld}}}\omega_{\mathrm{ld}}\right)$, $\tau_{\mathrm{I}} = 3 \cdot \tau_{\mathrm{ld}}$
phase lift frequency	$\omega_{\mathrm{ld}} = 5 \cdot \sqrt{k_x/m} = 760\,\mathrm{rad/s}$	
gain scale	$a_{\mathrm{ld}} = 0.15$, $a_{\mathrm{I}} = 2$	$a_{\mathrm{ld}} = 0.15$, $a_{\mathrm{P}} = 4$

4.6.1 Selection of optimal weighting matrices

The selection of weighting matrices for the optimal controller of the radial suspension is analogical to the weighting in the design of the SISO axial controller, presented in 4.5.2. However, the additional weights for the controlled flexible modes are required. The first flexible mode is the only one that could be efficiently controlled. The extra weights may be added, in regard to the observations from 4.1.2, in such a way that an active control of the first flexible mode is performed only at the end-A. The proper selection of weights results in the higher feedback gains when regulating the flexible mode at the end-A, compared with the lower gains when regulating the mode at the end-B. The elements in the state weighting matrix $\boldsymbol{Q}$ and the cross effect weighting matrix $\boldsymbol{N}$, which correspond to the states of first flexible mode are equal zero, but the elements of $\boldsymbol{N}$, which correspond to the control currents $i_{\mathrm{c},x,\mathrm{A}}$, $i_{\mathrm{c},y,\mathrm{A}}$, at the end-A of the rotor. When in fact the plain weighting of the first flexible mode only in matrix $\boldsymbol{Q}$ seems to be working also sufficiently. The weighting is applied to the states in the per-unit quantities with the normalized flexible modes (see A.5).

As already mentioned, there are two popular methods for reducing the spillover problem. The first method includes the elimination of observation spillover (Balas, 1978); and it is based on prefiltering the sensor data with a low pass or comb filter (many narrow bandpass filters). Nonetheless, implementing such a filter without introducing high phase delays to the measurements might be impossible. The second popular method is based on the elimination of a control spillover by filtering of the control signals. The additional delays in the open loop decrease the performance in terms of the tolerated step disturbance forces. Instead of adding an additional filter, it is also possible to reduce the control spillover that causes excitation of residual modes, by selecting a sufficiently slow actuator. The actuator bandwidth is just enough for the control of the selected flexible modes, and at the same time, it does not decrease the accuracy of the linearized model for the currents with higher amplitudes (used for the synthesis of the position control, as presented in section 4.2). If the spillover is still a problem, a low pass filter can be added in order to increase the attenuation of the open-loop gain at high frequencies.

Figure 4.21 shows that the applied controller does not destabilize uncontrolled (not actively controlled) flexible modes, that is, the poles of these aforementioned lightly damped modes remain in the left-half s-plane. What is more, the responses to the step reference position and disturbance force, $f = 0.5 \cdot i_{\mathrm{c,max}} k_i$, are the same (Fig. 4.22) for the control systems, which include the plant with and without the residual modes. In Fig. 4.21, the sensitivity of the control systems with, and without, the actively damped first flexible mode are plotted using solid green line, and dotted red line, respectively. This sensitivity function contributes to the attenuation of the disturbance signal introduced at the position sensors; it's maximum value (peak gain of the closed-loop function) is used as an index representing the relative stability of a MIMO system (see e.g. Takahashi et al., 2007 and Li et al., 2006). As an illustration, in the same manner the index of the stability of a SISO system can be evaluated by the minimal distance (d_{min}) on the Nyquist plot of the open-loop transfer function (G_{ol}) from the critical point (i.e., $d_{\mathrm{min}} = 1 + G_{\mathrm{ol}}$), where the sensitivity function is $1/(1 + G_{\mathrm{ol}})$.

When considering the MIMO systems, it is not possible to determine an

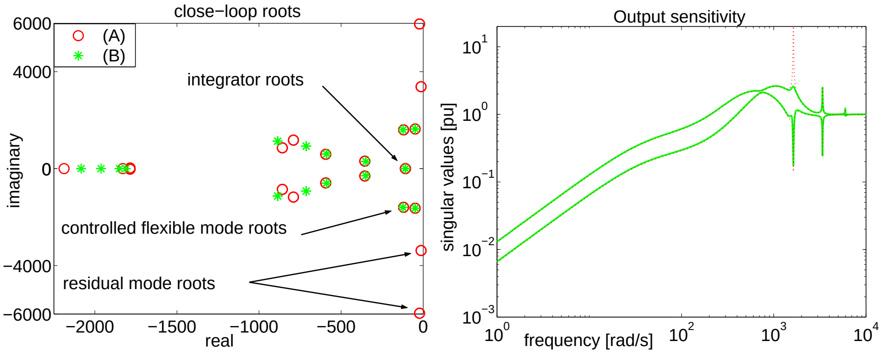

Figure 4.21: In the left-hand illustration, the closed-loop poles of control system that includes non-controlled flexible modes (A), and the control system regarded as in the control design (B), are shown. In the right-hand illustration, the singular-value plots of the sensitivity transfer function at the output of the plant that includes non-controlled flexible modes, are presented.

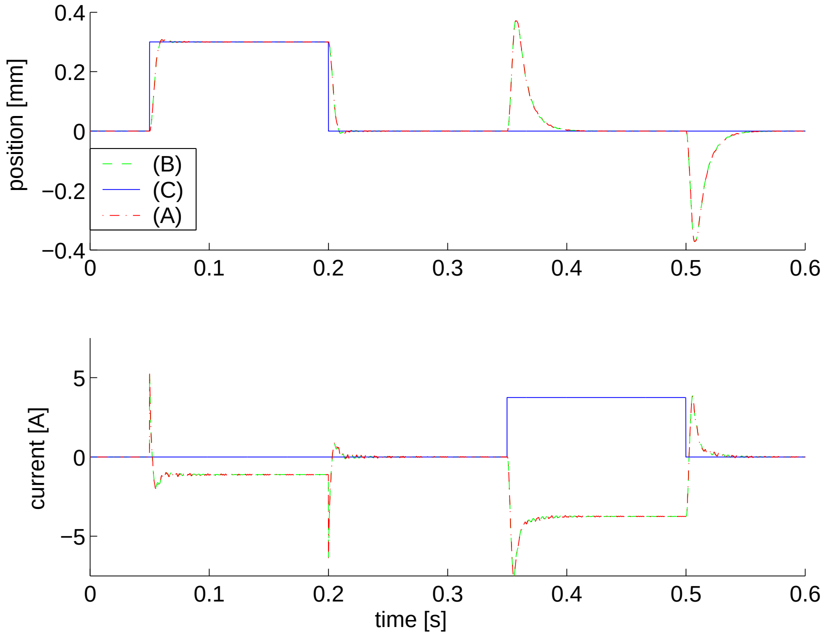

Figure 4.22: Responses of the control system that includes the plant with the non-controlled flexible modes (A), and the control system that includes the plant with only the first flexible mode (which is controlled) (B), to the step reference input and disturbance (C), are shown.

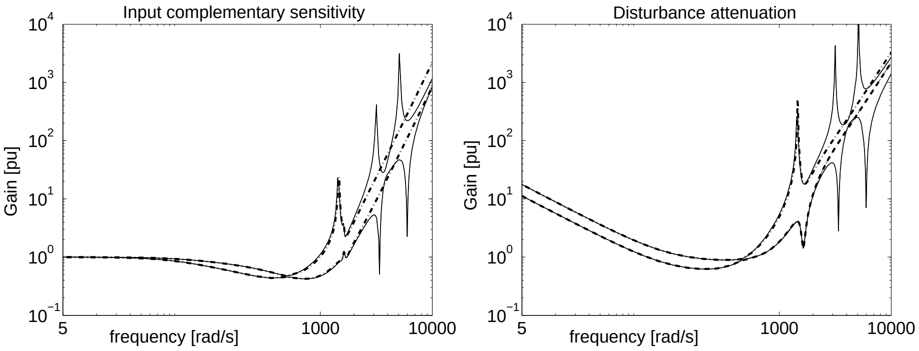

Figure 4.23: Plots of the singular values of the control system that includes the plant with the first flexible mode (bold dashed line) and with three flexible modes (solid line), are presented. The only actively controlled flexible mode is the first one.

unequivocal tolerated disturbance force over the frequency. However, the singular value plots of a MIMO system correspond to the Bode magnitude plot of a SISO one. Therefore, we may examine the singular values of the radial suspension, in the similar way as we used the Bode magnitude plot of the SISO axial suspension. In Fig. 4.23, the singular-value plots of the inverted complementary sensitivity, at the input (i.e. an inverted ratio of a control effort to disturbance) and the singular value plots of the inverted disturbance force attenuation (i.e. an inverted ratio of a position to input disturbance), of the MIMO radial suspension, are presented. The considerable peaks of the maximum singular values $\bar{\sigma}$ occur at the frequencies that are equal to the eigenfrequencies of the non-controlled flexible modes. These maximum singular values of the input complementary sensitivity (and of the disturbance force attenuation), are equal to the maximal gains of the system, in regard to the input disturbances. Hence the values of their inverse equal to the disturbance force magnitude in per-unit quantities, for the presented frequency range. As a result, the maximal tolerated disturbance force magnitude, at the given frequency, corresponds to the minimum from the two values at that frequency.

The summary of the closed-loop transfer functions of a MIMO control system is provided in Appendix A.2.

4.6.2 Unbalance force rejection control

In the magnetically borne rotor, which spins about a fixed axis, there are always some sinusoidal disturbance forces acting on the rotor. These forces are caused by the unbalance, which can be described as a discrepancy between the fixed axis of rotation (usually, the assumed axis of geometry of the rotor) and the principal inertia axis. Apart from an unbalance, all other discrepancies and imperfections, which make the system non-axisymmetrical, may cause additional harmonic disturbances. The resulting vibrational bearing forces are proportional to the square of the rotational speed.

The unbalance compensation in the AMB applications is referred to as an unbalance force rejection control (UFRC). In AMBs, the use of active control and the possibility of changing the stiffness and damping provide better capabilities to deal with the unbalance than in the traditional bearings. Control theory, rotor dynamics, and the literature on AMBs provide different UFRC methods. Basically, a compensation mechanism is synchronized with the rotational speed. It injects compensating harmonic signals, of proper amplitudes and phases, to the control system. In general, it is possible either to cancel the position vibrations (i.e. cancel the effect of the unbalance forces on the rotor position) or to cancel the magnetic force vibrations (i.e. cancel the effect of the unbalance forces on the control currents).

As an example, an adaptive feedforward compensation and discrete Fourier transform (DFT) are applied by Bleuler et al. (1994). Grochmal and Lynch (2006) and they sugest the reduced-order disturbance observer with the observer gains computed analytically (based on the desired location of eigenvalues) and scheduled according to the rotational speed. The interesting approach is presented by Lum et al. (1996), where the observer-based imbalance compensator performs an on-line identification of the physical characteristics of the imbalance and uses the result to tune the compensator. This last compensator technique workes under varying rotor speed. Many other compensation methods are also available. A short review of different compensation methods and references on them are given by Bleuler et al. (1994).

In this work, the observer-based UFRC is considered in two variants. In the first one, the position vibrations are canceled and the system can tolerate high sinusoidal unbalance forces while it maintains accurate rotor position. It results in low measured vibration amplitudes. In the second variant, the magnetic force vibrations are canceled and the rotor (considered as rigid) spins about its principal inertia axis without touching the safety bearings (assuming that the clearances are large enough to accommodate the unbalance). This results in minimal control currents. Both cases are designed as a periodic disturbance estimator that is combined with the constant disturbance estimator.

In the case of position vibration cancellation, two different design methods are employed and compared with respect to their robust stability, for the equivalent performance. For the better comparison, both the design methods are used in such a way that they result in the same closed-loop eigenvalues. The first design generalizes the LQ design of the full state estimator with the constant disturbance estimate, as in (4.11), to the one that includes a sinusoidal disturbance. The computation of the proportional gain matrix $\boldsymbol{L}$ and the disturbance estimator gain matrix $\boldsymbol{L}_{\mathrm{dist}}$ is based on the augmented plant model

$$\begin{bmatrix} \dot{\mathbf{x}} \\ \dot{\mathbf{x}}_{\mathrm{dist}} \end{bmatrix} = \begin{bmatrix} \boldsymbol{A} & \boldsymbol{B}\boldsymbol{C}_{\mathrm{dist}} \\ \mathbf{0} & \boldsymbol{A}'_{\mathrm{dist}} \end{bmatrix} \begin{bmatrix} \mathbf{x} \\ \mathbf{x}_{\mathrm{dist}} \end{bmatrix} + \begin{bmatrix} \boldsymbol{B} \\ \mathbf{0} \end{bmatrix} \mathbf{u}, \tag{4.18}$$

$$\mathbf{y} = [\boldsymbol{C},\, \mathbf{0}]\, \mathbf{x}. \tag{4.19}$$

where $\boldsymbol{C}_{\mathrm{dist}} = [\mathbf{I}, \mathbf{I}, \mathbf{0}]$ and the disturbance state matrix is

$$\boldsymbol{A}'_{\mathrm{dist}} = \begin{bmatrix} \boldsymbol{A}_{\mathrm{dist}} & \mathbf{0} & \mathbf{0} \\ \mathbf{0} & \mathbf{0} & \mathbf{I} \\ \mathbf{0} & \mathbf{I} \cdot \Omega^2 & \mathbf{I} \cdot 2\zeta\Omega \end{bmatrix}. \tag{4.20}$$

Similarly to the design of the constant disturbance model, also here the disturbance model is modified (perturb) in order to utilize Matlab's Control Toolbox.

The negative damping $\zeta = -0.05$ of a sinusoidal disturbance model is assumed. This perturbation is introduced in order to move the roots of the augmented plant model from the imaginary axis. In addition, ζ affects the resulting speed of the integration, for the sinusoidal disturbance estimate. Now, the augmented model used in the implementation applies the disturbance state matrix such as

$$\boldsymbol{A}'_{\text{dist}} = \begin{bmatrix} \boldsymbol{A}_{\text{dist}} & \mathbf{0} & \mathbf{0} \\ \mathbf{0} & \mathbf{0} & \mathbf{I} \\ \mathbf{0} & \mathbf{I}\cdot\Omega^2 & \mathbf{0} \end{bmatrix}. \tag{4.21}$$

The second design is based on the pole placement. It applies the closed-loop roots, which result from the Kalman filter design computed for the state estimates without the disturbances, plus the arbitrarily added integral poles.

Now, the state and disturbance estimate feedback matrix is $[\boldsymbol{K},\, \boldsymbol{K}_{\text{dist}}] = [\boldsymbol{K},\, \boldsymbol{C}_{\text{dist}}]$.

The unbalance responses of the simulated control system with and without the UFRC are presented in Fig. 4.24 and 4.25. The applied step disturbance force is $f = 0.2 \cdot i_{\text{c,max}} k_i \approx 402\,\text{N}$ and the applied couple unbalance[1] is equal to $500\,\text{g}\cdot\text{mm}$ that corresponds to the disturbance force amplitude equal to $137\,\text{N}$, at each radial bearing, for $\Omega = 5000\,\text{rpm}$.

The resulting closed-loop poles are the same for both aforementioned design methods, when the plant model without the residual modes is applied. However, the closed-loop pole patterns for the designed controllers and the plant that included the residual modes (Fig. 4.25) are different for both controllers; namely for the pole placement design of integrators, the residual modes are less damped (about six times) than for the optimal design. This difference can also be noticed when comparing the singular value plots of the output sensitivity transfer functions for both controllers (4.26). The singular values plot of the output sensitivity transfer function corresponds to the disturbance attenuation performance in the measured signal, and it is equivalent to the sensitivity of the SISO case, which indicates the robust stability.

In the case of magnetic force cancellation, the computation of $\boldsymbol{L}$ and $\boldsymbol{L}_{\text{dist}}$ and the feedback are the same as for the disturbance force cancellation, but the augmented plant models used in the design and implementation have the output equation such as $\mathbf{y} = [\boldsymbol{C},\, \mathbf{0}, \mathbf{I}, \mathbf{0}]\,\mathbf{x}$ and $\bar{\mathbf{y}} = [\boldsymbol{C},\, \mathbf{0}, \mathbf{I}, \mathbf{0}]\,\bar{\mathbf{x}}$, respectively. This eliminates the oscillating component from the error signal.

The experimental evaluations of UFRC for the position vibration cancellation and for the magnetic force cancellation are presented in Fig. 4.27 and in Fig. 4.28, respectively. In fact, the rotor was not rotating; however, the effect of couple unbalance was generated through the currents.

4.6.3 Comparison of LQ and PID controllers

As long as a rigid rotor (for slow rotation) is considered, it is possible to apply the decentralized control (four SISO controllers) to support the rotor radially in x and y directions. The low-order PID controllers may be easily designed manually in a similar fashion as the one for the axial suspension (see section

---

[1] couple unbalance – assuming no static unbalance, the remaining forces in each plane (in opposite sides of the center of rotor mass) act in opposite directions and are equal in magnitude (i.e. the central principal axis intersects the rotor axis at the center of gravity)

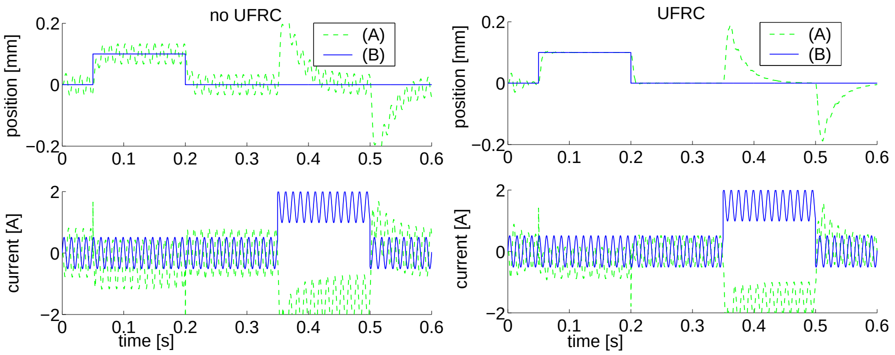

Figure 4.24: System without UFRC and the system with UFRC that cancels the unbalance forces are presented under the couple unbalance. The (A) stands for the measured position x_{A} and control current $i_{\mathrm{c},x,\mathrm{A}}$; the (B) is the reference position and the scaled disturbance force f_{dist}/k_i.

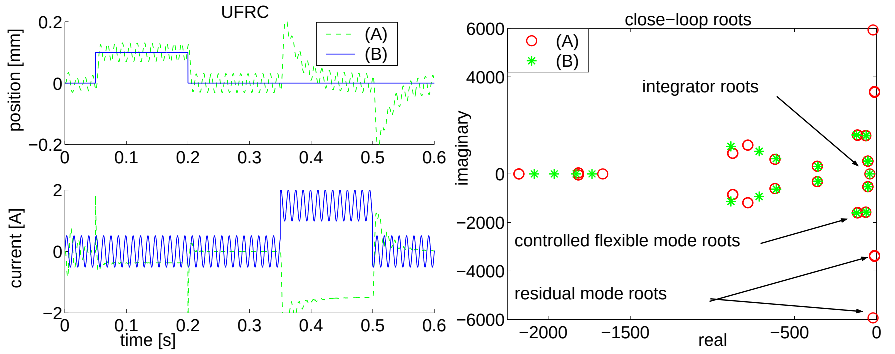

Figure 4.25: In the left-hand illustrations, the system responses with UFRC for canceling the magnetic force vibrations (therefore minimizing control currents), are presented. The measured position x_{A} and control current $i_{\mathrm{c},x,\mathrm{A}}$ are indicated by (A). The reference position $x_{\mathrm{ref,A}}$ and the scaled disturbance force f_{dist}/k_i are indicated by (B). In the right-hand illustration, the closed-loop roots of the system used in the control design (B) and the control system that includes non-controlled flexible modes (A) in the plant, are shown.

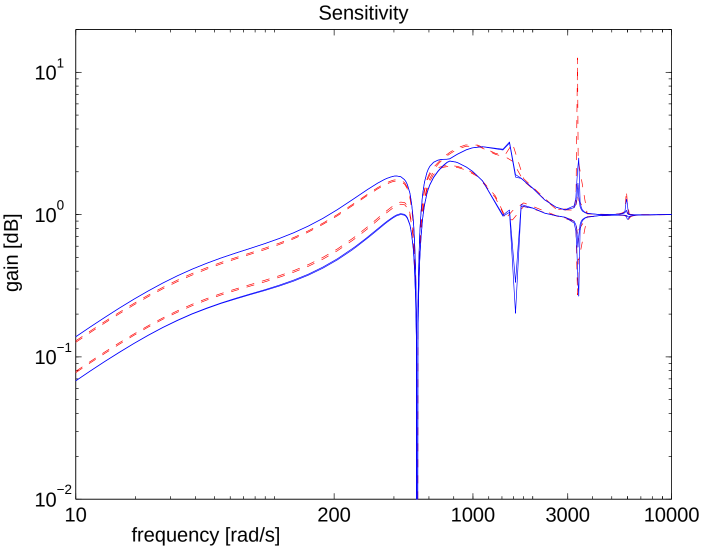

Figure 4.26: Singular values plot of the output sensitivity function for the systems with UFRC, are presented. The blue plot corresponds to the system design based on the optimal gain selection and the red plot corresponds to the system design based on the pole placement.

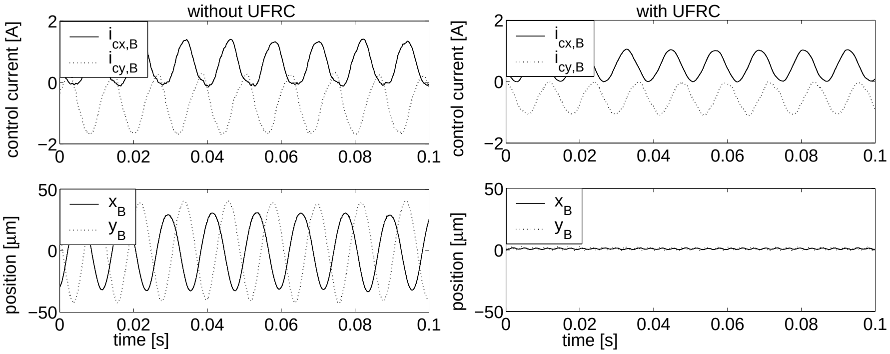

Figure 4.27: Measured responses of the control system without and with UFRC for the unbalance force cancellation, when the couple unbalance is $500\,\mathrm{g}\cdot\mathrm{mm}$ for $\Omega = 5000\,\mathrm{rpm}$.

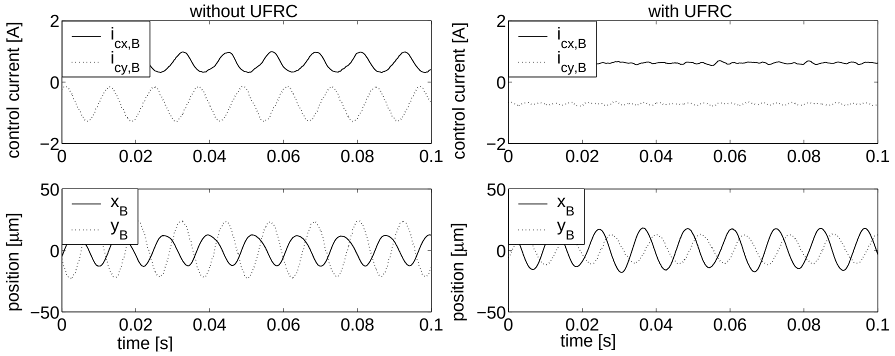

Figure 4.28: Measured responses of the control system without and with UFRC for the magnetic force cancellation, when the couple unbalance is 250 g · mm for $\Omega = 5000\,\mathrm{rpm}$.

4.4). However, for the rotor model that includes the flexible modes, the obtained PID controllers are unstable, and they have to be improved.

Let us consider a lead compensator in Eq. (4.5). We include the bending modes in the design. Now, we include the first bending mode into the SISO plant model. We assume that it does not affect the end-B of the rotor (as the node of the bending mode is very close to the actuator node). Next, we build the approximated plant model for the end-A as

$$G(s) = \frac{k_i}{m_\mathrm{A} s^2 - k_x} + \frac{k_i d_1}{m_1 s^2 + d_{\mathrm{M},1} s - k_{\mathrm{M},1}}, \tag{4.22}$$

where m_A, m_1, $d_{\mathrm{M},1}$, $k_{\mathrm{M},1}$, and d_1 are the rotor mass supported at the end-A, modal mass of the first bending mode, modal damping, modal stiffness, and the first modal influence factor at the end-A (Lantto, 1999), respectively. In this case, the influence factor may be roughly approximated by the distance between the actuator node and the node of the first bending mode. Other parameters are obtained from the FEM model. Now, we can use the approximated model in the controller design.

We modify the old control by adjusting the frequency of the maximum phase in order to obtain the sufficient stability margins, for each loop at a time. After some iteration with the controller parameters (decreasing the proportional gains, slightly increasing the current control bandwidth, and selecting the $\omega_\mathrm{ld} = 0.7 \cdot 2\pi \cdot 260\,\mathrm{rad/s}$), when taking the values according to Table 4.3, as the starting point, we obtain the stable decentralized controller. In further iterations, the resulting multiple SISO, overall controller is tested for stability with the plant model that includes the first three bending modes.

The step responses of the closed-loop system (with a lead compensator), and the comparison of the unbalance responses of the decentralized PID control with the centralized LQ position control, for different rotational speeds, are shown in Fig. 4.29.

For the PID control of the radial suspension, the step responses are not as good as for the LQ control, even though the PID-based control assumes a 40% wider actuator bandwidth than the LQ control. When looking at the unbalance

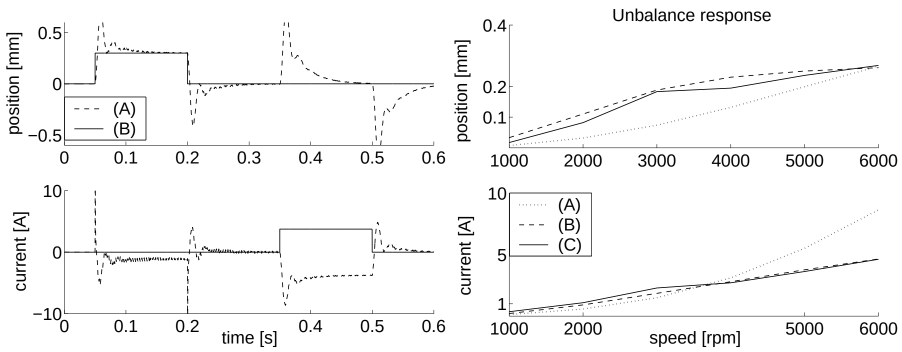

Figure 4.29: On the left, the step position and disturbance responses for PID radial suspension. On the right, the comparison of the centralized LQ position control with high stiffness (A), low stiffness (B), and the decentralized PID control (C), for different rotational speeds, in simulations, is presented.

responses, the behavior for lower frequencies is also not too good because of the low stiffness (required for stability).

For the LQ MIMO control, which is able to provide higher gains (and better damping) without loosing the stability, the gyroscopic effect is taken into account. In consequence, the optimal control solution vary with the rotational speed. The LQ control can be tuned, and remain stable, to have good unbalance rejection both at low or high frequencies. The low stiffness control design may be obtained by, for example, increasing the available maximum displacement in the weighting matrix $\bar{\boldsymbol{Q}}$. It occurs that the effect of gyroscopic coupling is relatively weak, when comparing the centralized LQ controller with UFRC and the decentralized one with UFRC, the unbalance responses are the same for the under-critical operation.

Moreover, for both control systems (PID- and LQ-based), the variations of rotational speed result in relatively insignificant changes of the closed-loop poles and zeros (Fig 4.30). In Fig 4.30, only the poles and zeros, which have positive or zero imaginary parts, and which are close to the imaginary axis, are shown.

Figure 4.31 presents the start-up of the rotor when a centralized LQ controller with the actively controlled first flexible mode and the constant disturbance estimator was employed. Since the estimator has no knowledge about the initial states, it is started together with the measurements before the integral action is enabled to work as a filter with zero control currents. It is sufficient to enable only the estimation of the rigid body modes during this initial phase. In Fig. 4.32, the start-up of the rotor when PID controller is applied, is shown.

The measured responses of the LQ controller and PID controller to the step disturbance force introduced through the AMB at the end-B of the rotor ($f_{\mathrm{dist}} = k_i i_{\mathrm{c},y,\mathrm{B}}$, where $i_{\mathrm{c},y,\mathrm{B}} = 2\mathrm{A}$) are presented in Fig. 4.33 and 4.34, respectively. Figure 4.35 shows the control currents of the LQ controller when the step disturbance is applied.

To sum up, in the studied rotor the relative polar inertia is very small and therefore the gyroscopic effect has small influence on the responses of the multiple SISO and MIMO control. The differences in the unbalance responses for different controllers (without UFRC) result from the gain (low-stiffness vs. high-

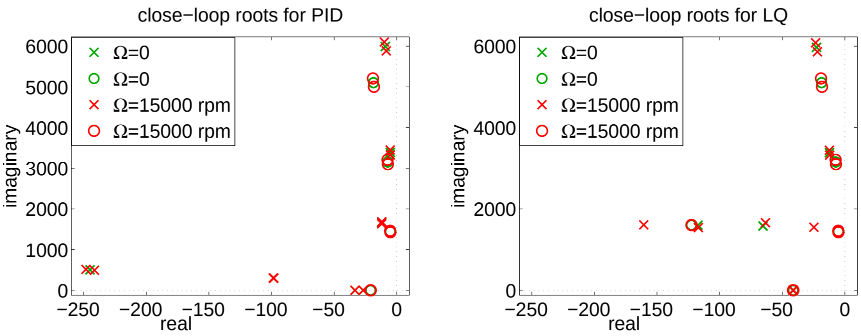

Figure 4.30: In the left-hand illustration, the pole-zero map of the closed-loop system with the PID controller, and in the right-hand illustration, the pole-zero map of the closed-loop system with the LQ controller are presented. The poles are plotted as x's and the zeros are plotted as o's.

stiffness solution). It is not possible to obtain optimal solution for all the frequency ranges, and hence the control design is a compromise between low and high frequencies.

4.7 Discrete-time control

In the digital control, the controllers resulting from the continuous-time design have to be discretized. Alternatively, the whole design process has to be carried out in the discrete-time. The conversion from the continuous-time to the sampled system is only an approximation. The quality of this approximation depends on the utilized method (used for obtaining the discrete realization of a system) and the sampling period T.

Different methods for obtaining a discrete realization, including discrete equivalent (e.g. backward rectangular method, bilinear transformation, zero-order-hold, forward rectangular) and methods based on a numerical solution of ordinary differential equations (e.g. Euler's method, fourth-order Runge-Kutta method), are discussed in Publication III. In addition, the publication considers that some methods introduce a kind of state transformation, which might increase the computational burden, distort the numerical condition of the controller (or plant), and distort the state representation and its physical meaning.

In a similar way as in the continuous-time, the design of the AMB controller can be carried out directly in the discrete-time, now on the discretized plant matrices $\boldsymbol{A}$, $\boldsymbol{B}$, and $\boldsymbol{C}$. In the design of the position control loop we consider LQ methods. In order to obtain the output feedback controller, we compute the optimal state feedback law and concatenate it with the Kalman filter for the plant and disturbance state estimation. The discrete-time estimator is formed as

$$\bar{\mathbf{x}}_{k+1|k} = \boldsymbol{A}\bar{\mathbf{x}}_{k|k-1} + \boldsymbol{B}\mathbf{u}_k + \boldsymbol{L}_{\mathrm{fb}}\left(\mathbf{y}_k - \boldsymbol{C}\bar{\mathbf{x}}_{k|k-1}\right), \tag{4.23}$$

$$\bar{\mathbf{x}}_{k|k} = \bar{\mathbf{x}}_{k|k-1} + \boldsymbol{L}_{\mathrm{ff}}\left(\mathbf{y}_k - \boldsymbol{C}\bar{\mathbf{x}}_{k|k-1}\right), \tag{4.24}$$

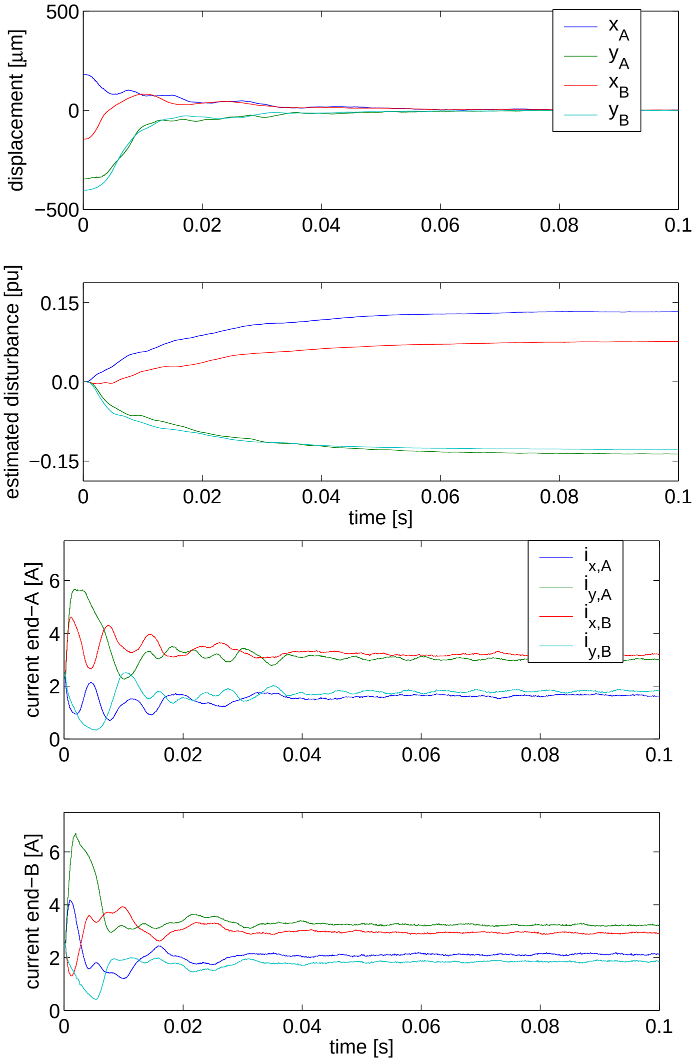

Figure 4.31: Start-up of the rotor (radial suspension) when centralized LQ controller was employed.

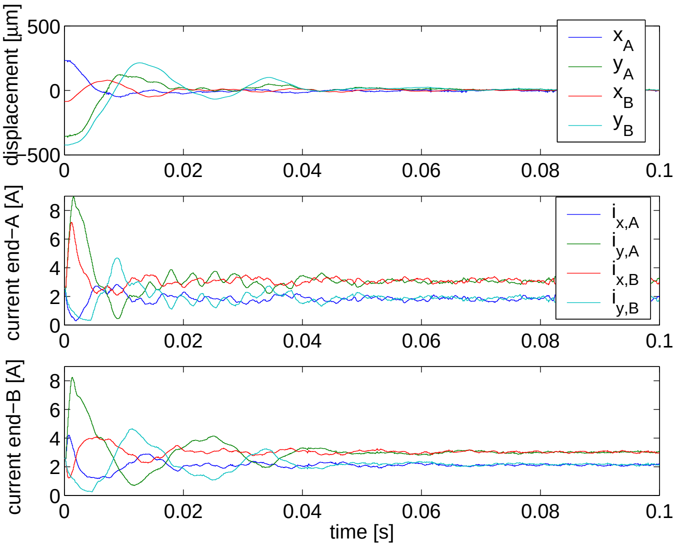

Figure 4.32: Start-up of the rotor when decentralized PID controller was employed

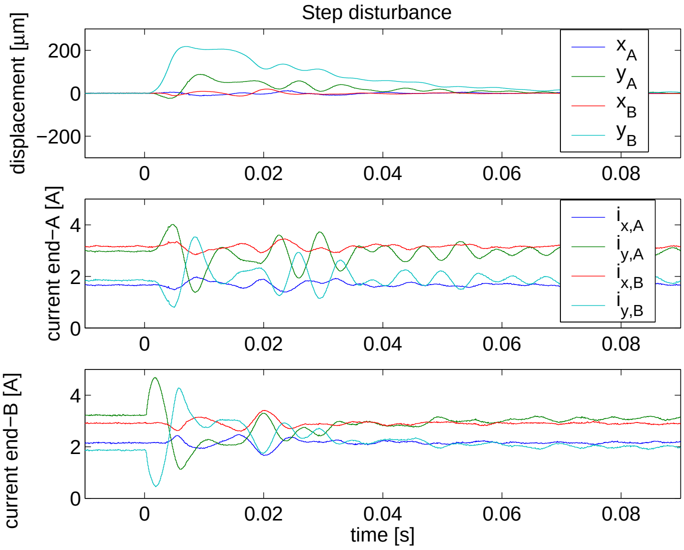

Figure 4.33: Responses of the LQ controller to the step disturbance

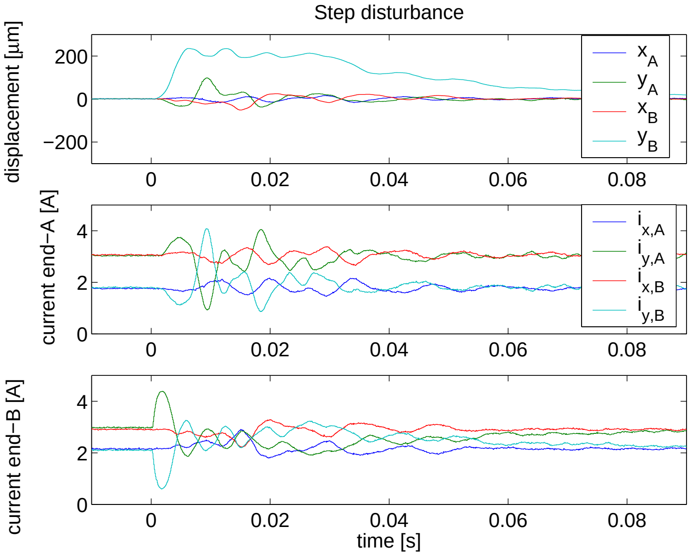

Figure 4.34: Responses of the PID controller to the step disturbance

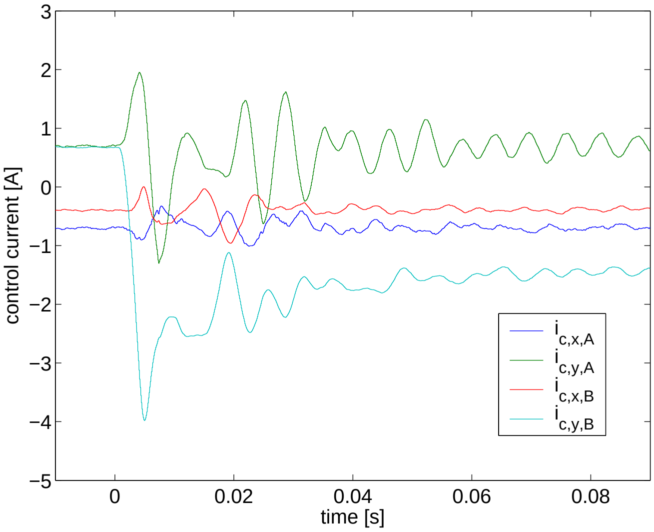

Figure 4.35: Control current of the LQ controller during step disturbance

where $\bar{\mathbf{x}}_{k|k}$ and $\bar{\mathbf{x}}_{k|k-1}$ are the vector of state estimates at a time instant k based on data up to the time instant k (current state estimate), and the vector of state estimates at the time instant k based on data up to the time instant $k-1$ (predictor state estimate), respectively. The estimator feedback (predictor estimator gain) matrix $\boldsymbol{L}_{\mathrm{fb}}$ is obtained from the solution of the Riccati equation (Franklin et al., 1998), by the selection of the cost weights. The feedforward (current estimator gain or innovation gain) matrix $\boldsymbol{L}_{\mathrm{ff}} = \boldsymbol{A}^{-1}\boldsymbol{L}_{\mathrm{fb}}$ (if $\boldsymbol{A}$ is not singular). The state feedback control is then obtained from the current state estimate output as

$$\mathbf{u}_k = -\boldsymbol{K}\bar{\mathbf{x}}_{k|k}, \tag{4.25}$$

where the state feedback matrix $\boldsymbol{K}$ is obtained from the solution of the Riccati equation, by the selection of the cost weights in the LQ criterion. The selection of the cost weight matrix is similar as in the continuous-time design, but the disturbance model is $\boldsymbol{A}_{\mathrm{dist}} = e^{T_{\mathrm{s}} \cdot 1/\tau_{\mathrm{I}}}$.

As is shown in Fig. 4.6, the modulation delay (equal to half of the modulation period $T_{\mathrm{d}} = 0.5 \cdot 1/f_{\mathrm{carr}} = 25\,\mu\mathrm{s}$), is insignificant for the inner control loop. When applying the dSPACE as a control platform, the sampling time of the inner control loop is $T_{\mathrm{s}} = 50\,\mu\mathrm{s}$ and the outer position control loop is $T_{\mathrm{s}} = 100\,\mu\mathrm{s}$, respectively. In this case, the applied sampling rate is about 40 times faster than the bandwidth of the current control loop. Therefore, for the presented system, a discretized continuous-time design and a discrete-time design (emulation by equivalent cost with the equivalent cost weight matrices computed as presented by Franklin et al. 1998) yield almost the same closed-loop control systems, which result in the same Bode responses (Fig. 4.36) in the required bandwidth. However, in the discrete design we can easily introduce the additional degree of freedom to the design procedure.

The Pincer procedure (Franklin et al., 1998) provides additional option in computing the state feedback control, in regard to the minimal settling time of the regulated states. In this procedure, the designer selects the settling time t_{s}, within which all the regulated states are required to settle to less than the defined margin (e.g., 0.01 of the maximum steady-state value). Next, the discretized plant matrices are scaled by the parameter ϑ based on the selected settling time, sampling time, and margin ($\vartheta = [0.01]^{-T_{\mathrm{s}}/t_{\mathrm{s}}} \geq 1$). The scaled matrices $\vartheta\boldsymbol{A}$ and $\vartheta\boldsymbol{B}$ are used in the computation of the state feedback of the LQR. Consequently, it is ensured that the closed-loop poles are inside the circle of radius $1/\vartheta$. By increasing ϑ we can increase the tolerated disturbance forces in low- and medium-frequency regions, in the expense of the tolerated disturbance forces in the high-frequency region (for the previously selected optimal weighting matrices, Fig. 4.37). For $\vartheta > 1$, the system stability does not change considerably, but an overcurrent appears during a response to a step reference.

4.8 Numerical conditioning

In the digital implementation, in order to make the subsequent state-space computation viable, a numerical conditioning is required. Basically, before the implementation, it is necessary to scale (transform) the system states and variables to be appropriate for the utilized hardware number format and computation accuracy. This aspect is discussed in Publication II and Publication III. As a

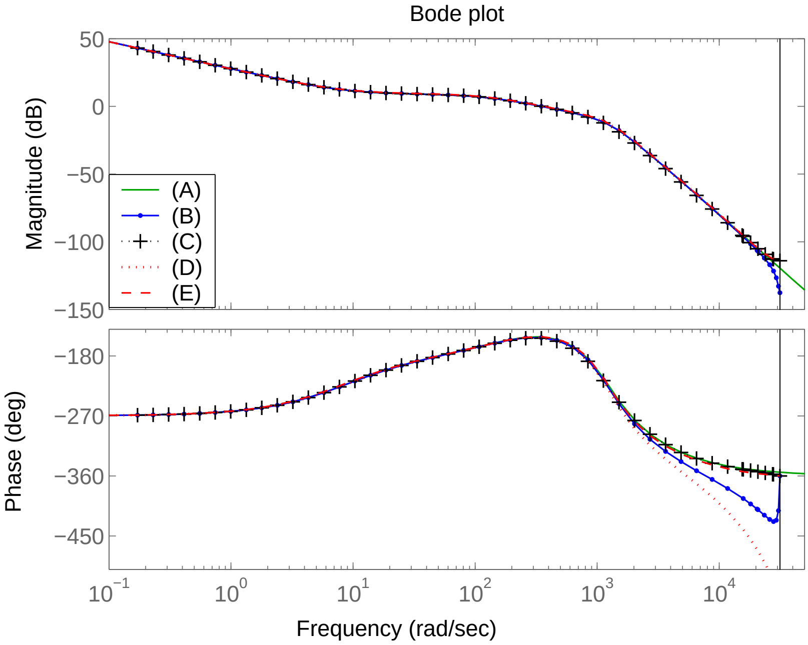

Figure 4.36: Bode plots of the continuous-time open-loop SISO system (A), its zero-order hold equivalent (B), backward rectangular equivalent controller and zero-order hold plant (C), open-loop based on a discrete-time design with a predictor estimator (D), and the discrete-time design with a current estimator (E), are presented.

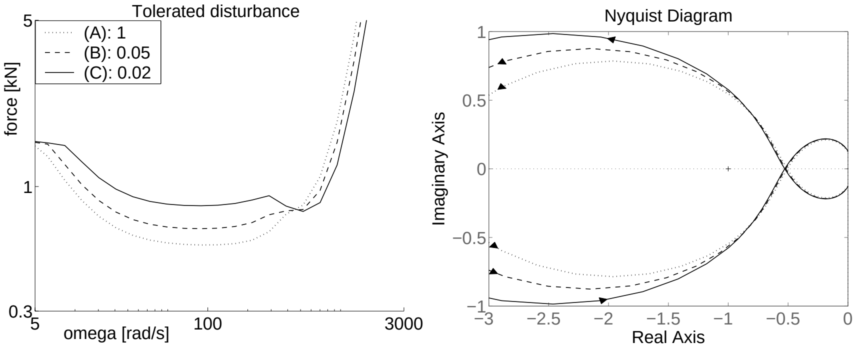

Figure 4.37: Tolerated disturbance force and Nyquist diagrams of the SISO case for different settling time t_s in the Pincer procedure, i.e. for (A) $t_s = 1$ and so forth

matter of fact, it might be recommended to transform the plant model even before carrying out the design process, as it, in general, should lead to more accurate results. As an example, the state-space plant model for the axial (radial) suspension, in physical quantities, has a condition number[2] equal to 2.65e4 (2.67e6), compared with the condition number equal to 17 (66) for the plant in per-unit quantities. Although, in Matlab, which uses numerically optimized design functions, the per-unit scaled model and the model in physical quantities yielded the same control design results for the presented LQ design procedure, in regard to the closed-loop system eigenvalues.

4.9 Adaptive control

For highly gyroscopic systems, in order to avoid a loss of performance or even instability when the rotational speed changes, the controller should be adaptive and dependent on the rotational speed. The variations in the plant's parameters (due to the rotational speed) may be predicted when the system model is well defined. In such a case, the control gains in the regulator and the estimator could be scheduled. In order to accomplish this goal, the plant is linearized in several operating points and the optimal controllers for these points are obtained. The control have to be robustly stable for overlapping areas of points close to the design equilibrium points. The robust stability and performance may be verified by multivariable frequency analysis techniques.

Apart from the scheduling of the regulator and estimator gains, the $\boldsymbol{A}$ matrix of the estimator may be divided into the Ω dependent and constant matrices. Using a rotational speed as a measured parameter and performing an on-line discretization (e.g., simplified ZOH as described in Publication II and III), a somewhat smother transitions between the operating points is achieved. Nevertheless, in the weakly gyroscopic systems, such as the prototype, a simple gain scheduling (or even the control design for zero rotational speed) would be sufficient. In the case of the UFRC, the algorithm requires accurate speed measurements (up to 1-3 %) in order to work efficiently. If an effective UFRC in a wider speed range is required, the gain scheduling with many operating points is necessary.

4.10 Robustness

Typically, in order to provide the system stability over the wide range of operating conditions, fixed gain controllers have to be tuned with wide stability margins. Numerous control strategies, which apply robust techniques for the AMB control are known from the literature (Lantto, 1999), and (Nonami and Ito, 1996). However, such a preparation for the worst-case conditions decreases the system performance. In addition to that, the performance for local controllers may also be limited by the non-collocation of the actuators and sensors.

By applying the nonlinearity compensation techniques, presented in section 4.3, the large uncertainty of the AMB actuator can be reduced. Nevertheless, not all nonlinear effects of the actuator could be compensated accurately.

---

[2] The condition number of matrix $\boldsymbol{A}$ equals to the ratio of the largest singular value of $\boldsymbol{A}$ to the smallest one. A large condition number indicate a almost singular matrix.

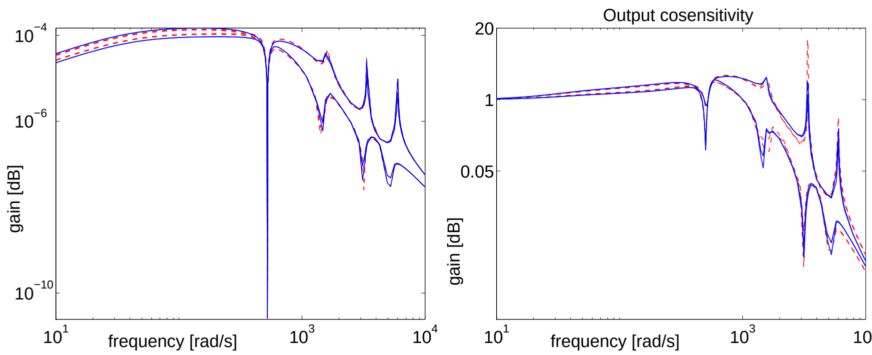

Figure 4.38: In the left-hand illustration, the singular values Bode plots of the transfer function matrix from the disturbance signal introduced at the output of the plant to the control effort of the controller (with UFRC) is presented. In the right-hand illustration, the complementary sensitivity at the plant output, for the system with UFRC, are presented. The blue plots correspond to the system design based on the optimal gain selection and the red plots correspond to the system design based on the pole placement.

The eddy currents, magnetic cross-connections, hysteresis in the magnetic circuit, and sensor nonlinearities still cause considerable uncertainties.

For the MIMO case, gain/phase margins and Nyquist plots of one-loop-at-a-time ignore the cross coupling.

In the case when the plant discrepancies are small in the model, we can design a high-gain, high-performance feedback controller. On the one hand, high gains may attenuate the effects of model discrepancies and reduce the sensitivity of the control system to plant noise. On the other hand, the discrepancy may be such that the sign of the gain changes (e.g., uncertainty in the location of a node of the flexible mode shape in regard to the actuator node). For example, this takes place when the end coupling is removed from the end-B of the rotor (the mode shape of the flexible mode and its associated critical speed change) and as a result controllers that actively damp the fist flexible mode become unstable. In such a situations it may be risky to utilize large feedback gains. In particular, the plant model discrepancies and the actuator bandwidth are limiting factors in the active control of flexible modes.

For the control system with the UFRC, the controller with the Kalman filter proved less sensitive to the multiplicative plant perturbation than the controller with the estimator obtained by pole placement method (4.38). In other words, the former one can tolerate greater multiplicative uncertainty before becoming unstable.

4.11 Summary

The chapter focuses on the control of the magnetic suspension system. The objectives from subsection 4.1.3 are fulfilled. However, not all a priori conclusions from this section are confirmed. For one thing, the study of the unbalance responses of the test rotor prove that there are no significant difference in performance for increased rotational speed, when testing the centralized and decentralized controllers. These observations are contrary to the results presented in the literature (e.g., Zhuravlyov, 2000). Admittedly, the tested rotor is only slightly gyroscopic.

In the current control, a fast tracking of the reference input and disturbance rejection require large current control gains. If the full capabilities of the actuator are to be utilized, the maximal current and voltages lead to the considerable nonlinearities. What is more, in a very demanding control system with high bandwidth requirements and with reduced premagnetization current, the limited force slew rate and actuator saturation should not be ignored in modeling and design.

The described force-field linearization at the output of the outer position control together with the linearization of the inductance in the internal current control loop provide better agreement between the linear actuator model and the dynamics of the actuator. A more constant linear stiffness than for non-compensated actuator is obtained in the control bandwidth. Notwithstanding, the benefits of the linearization, the compensation of the dynamic inductance seams to be not necessary. The presented study assumes that nonlinearities are modeled correctly and that eddy currents and hysteresis effects could be neglected. A study of the relationship of the magnetic force to the coil current, which considers the eddy current effects, owing to both the rotor rotation and variation of the dynamic control current is given by Sun et al. (2006). The position controller with a hysteresis compensation for AMBs is presented by Volkert et al. (2006).

In the position control, because of the limited actuator bandwidth, only a control of the first flexible mode could be considered. When in fact, the node of the first mode shape is close to the actuator, at the end-B of the rotor. As a result, two control strategies for the LQ centralized control are applied. The first one includes only the control of the rigid body modes and the second, in addition to the rigid body modes, comprises also the first bending mode, but the rotor is controlled only at the end-A. The controllers may employ the constant and sinusoidal disturbance estimators (UFRC). In the design of the control with the disturbance estimate, the use of Eq. (4.10), (4.11), and (4.18) might be numerically sensitive, and it should be carried out with care. Nevertheless, in the studied application these applied methods provide satisfactory results, and they occur to be better than the pole placement method. Overall, a centralized (i.e. LQ-based), adaptive (e.g., with gain scheduling), and nonlinear (actuator compensation) controller provides better performance than local, non-adaptive, and linear controllers.

Considering the discrete design and control, the discrete-time realization of the controller obtained by applying a continuous-time design with the use of a suitable discrete equivalent (e.g. backward rectangular or bilinear) yields the same results as the controller based on a discrete design (that used the equivalent weighting matrices) with a current estimate.

To sum up, in this chapter, the control designs presented in the appended publications were refined and extended. In particular, the explanation of the current and predictor state estimates provided in Publication V, was clarified in section 4.7.

Chapter 5

FPGA-based control platform

This chapter provides an introduction to FPGAs, tools for a design development, and design and testing methodology. The chapter summarizes and concludes the use of FPGAs as a control platform for magnetic suspension systems. The details of the FPGA-based implementation (i.e, utilized resources and validation results) are presented in the appended publications.

5.1 Tools and design methodology

The first step on a way to the practical realization of the embedded controller is building the software part of the prototyping platform. The software includes: interfaces to hardware, communication between different processing units, user interfaces, arithmetic units, and other low-level software components. Afterwards, the control equations have to be prepared for the digital implementation, that is, they are prepared for a specific number representation and discretized. The evaluation of the necessary bit widths in the fixed or floating-point number formats may be performed in Matlab. The different possibilities for the discrete realization of the continuous-time equations are presented in Publication III. Finally, the actual coding of the control may start.

The design of the control software was carried out using bottom-top methodology presented in Fig. 5.1. This choice of methodology resulted from the fact that at first, the control hardware and prototyping platform were built and after that the control design was carried out. After completion of two bottom layers from Fig. 5.1, the remaining control algorithms were coded and evaluated using the Virtex-II Pro – dSPACE platform. The purpose of the dSPACE was to serve as a user-friendly environment for testing different control concepts on a fly, to use the Simulink, and Matlab for automated rapid generation of the control software.

As for the programming languages utilized for designing an FPGA software, traditionally HDLs, such as VHDL or Verilog are utilized. During the past few years, there have been appearing C-based design flows, compilers, and integrated development environment (IDE) for FPGAs, such as for example Mentor Graphics' Catapult$^{\text{TM}}$ C synthesis tool, Celoxica's Handle-C IDE, and SystemC library. The high-level design flows can also be based on a block graphical design. A well-known example is Xilinx's System Generator$^{\text{TM}}$ for Simulink. The

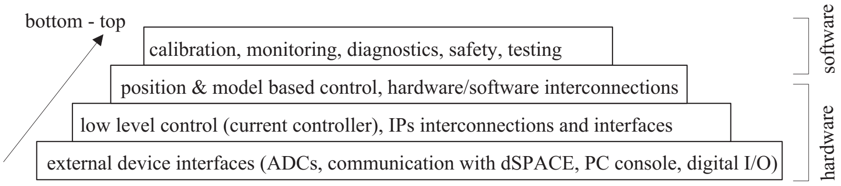

Figure 5.1: Design of control software was carried out using bottom-top methodology.

author believes that an FPGA design can benefit from the high-level design methodologies and approach to the DSP design in the near future. Nevertheless, in the described work a typical HDL-based design was still applied for FPGAs.

The HDL design methodology comprised of dividing a design into small parts, HDL coding, behavioral simulations, more detailed (e.g. post place and root) simulations, testing with a logic analyzer, and finally testing of a complete design (in-system testing). In addition to that, different validation techniques and the FPGA-based emulation are considered in the final sections. In this work, the programmable hardware coding was carried out in VHDL, in Xilinx's ISE 6.1 and ISE 7.1. The software for the PowerPC processors was written in C, using the Embedded Development Kit (EDK). Testing was performed with Mentor Graphics' Model-Sim HDL simulator.

In order to improve the maintainability of the software and to ease the design iterations, documenting of the HDL project might be carried out in UML notation (see e.g. Goma, 2000). As an illustration may be given the usage of sequence diagrams for depicting a data flow in the embedded controller (in Publication I).

5.2 Digital arithmetic functions

The digital control of active magnetic bearings requires a lot of arithmetic operations. When using FPGAs to implement the controller, the programmer often has to implement some of the arithmetic operations by himself. In this section, the implementation of the selected arithmetic operations, which are used and may be useful in the application-specific (embedded) AMB control system, is considered.

5.2.1 Interpolation

In general, instead of using one high-order polynomial for representing some complex function, different polynomials of lower degree can be fitted through a subset of breakpoints, and the final function value can be interpolated between these breakpoints. If breakpoints are close enough, a linear interpolation is sufficiently accurate. A generic implementation of a linear piecewise interpolation of a one argument function consists of a look-up table that stores the function values and a multiply-add unit. The implementations of interpolation methods for multivariable functions are less common and they are considered less frequently in hardware than in software.

Regarding simple methods suitable for the VHDL implementation of the nonlinear force field, the piecewise interpolation algorithms are classified into two groups.

The first one is the piecewise interpolation by sum of areas. In the algorithm, two arguments are used to obtain four closest entry values of the function from the look-up table. The integer part of the normalized arguments is utilized to access the look-up table, and the remaining fractional parts are used in the computation of the aforementioned areas. Four corner function values from the look-up table are multiplied by the opposite square areas. The interpolated function value equals to a sum of these multiplications. The resulting function is continuous and well scalable for fixed-point implementation.

The second algorithm is a piecewise interpolation with low-order polynomials. This method requires preparing the look-up table with coefficients of piecewise interpolated N-order single variable polynomials. Generalizing the linear piecewise interpolation, polynomials can be fitted for either ones of two argument values. The result is calculated by a sum of closest entry polynomials evaluated for one of the input variables, scaled proportional to the distance between the second input argument and its two closest breakpoints. When polynomials of two variables are used, the interpolated function value is obtained from the surface equation. The surface coefficients are read directly from the look-up table.

The selected look-up table based on the interpolation methods and their comparison are presented in Publication V. The methods are suitable for the application of the nonlinearity compensation as in AMB controller. The VHDL implementations of the algorithms can be found in Publication II and III. The implementations are generic and may be utilized also for other purposes than modeling of the AMB force field. For example, they could be used for modeling the saturating inductance surfaces in sophisticated electric motor controllers.

5.2.2 Matrix operations

The linear part of the plant's dynamics may be implemented as a custom-built arithmetic unit (AU). Such an application-tailored AU has the advantage over the commercial ready made ones; it provides a compromise between the utilized resources, speed, and accuracy of the number format. The implementation details of the different versions of the arithmetic unit for computing state-variable form are given in Publication II and III. The required arithmetic operations include two matrix times vector multiplications and addition of two matrices. The aforementioned AU can be utilized for optimized hardware implementation of the plant-emulator or the state observer. Apart from that, Publication II considers possible improvements to the hardware architecture of the AU. Especially, an AU with parallel multiply-accumulate (MAC) units for real and complex-numbered state-space models is proposed to further decrease the overall latency.

5.2.3 Floating-point arithmetics

The use of floating point arithmetics in the implementation of a flexible rotor controller (or emulator) would improve the computational accuracy of the algorithms. Nevertheless, it still could be more efficient to use the fixed-point, very long registers for storing the accumulated variables and to use an k-bit adder with a sufficiently large k. As an alternative, in order to increase the computational accuracy when utilizing the floating-point number format, the equations in the state-variable form may be formed in such a way that first, all small components are summed and then, the previous value of a state variables are added. As a result, the state equation becomes

$$\bar{\mathbf{x}}_{k+1|k} = (\boldsymbol{A} - \mathbf{I})\,\bar{\mathbf{x}}_{k|k-1} + \bar{\mathbf{x}}_{k|k-1} + \boldsymbol{B}\mathbf{u}_k, \tag{5.1}$$

where $\boldsymbol{A}$ is the discrete equivalent of the continuous-time state matrix. The term $(\boldsymbol{A} - \mathbf{I})\,\bar{\mathbf{x}}_{k|k-1}$ is computed first, then $\boldsymbol{B}\mathbf{u}_k$ is added, and finally $\bar{\mathbf{x}}_{k|k-1}$ is added as the last term. The advantage of (5.1) is clear when looking at the equations of the discrete equivalent matrices in Publication III for the simplified ZOH or forward rectangular.

The floating-point operations such as addition and multiplication could be either employed as a ready-made IP from commercial libraries, or they could be custom made. As an example a custom-tailored floating-point arithmetics was utilized by Jastrzębski et al. (2004b). A simple-datapath floating-point addition, where a critical path included two shifters, one for the alignment of operands and another for normalization of the result, were used. More complex schemes, such as two-path adder that includes only one variable position shifter in each path, as presented by Ercegovac and Lang (2004), could also be fully custom coded.

5.3 Magnetic bearing controller

In digital implementations, the final performance of the controller is typically decreased by an ADC delay, computational delay, modulation delay, system approximation with difference equations, and finite numerical accuracy caused by digitization and number representation. FPGAs, owing to their unusual data throughput and flexible parallel computing capabilities, offer minimization of computation delay and possibility to increase numerical accuracy when compared with any standard DSP. With FPGA realizations, the high-order of the controller does not limit the performance owing to its computational cost. In FPGAs, the internal architecture of the devices combined with the significant number of I/Os enables system integration at a single chip level instead of at a board level. This way, by including all the computational intelligence, ADC handling, and PWM on a single chip, the overall input to output delay, as well as the system integration can be improved. In fact, the maximal sampling frequencies are determined by the ADC performance and required sampling to bandwidth ratio, not by the computation time.

5.3.1 Hardware-software partitioning and data flow

The lower-level control and basic functionality such as the inner current control loop, PWM, interfaces to external devices and on-chip interconnections are best suited to be implemented in the programmable logic. The upper-level control, such as outer position control loop, monitoring, diagnostics, calibration, and safety algorithms do not necessarily require very fast execution rates. Therefore, they are better suited for the implementation as software, in the PowerPCs or in a soft processor core. But, if necessary, it is also possible to implement part of them (e.g. the critical safety part of the position control) as hardware functions in an HDL.

Regarding the data flow organization, when writing the control software for an actuator, one of the goals is to minimize the time-lag of the current controller in relation to the reference and measured currents. The timings of the reference current signals depend on the timings of the position ADCs and the applied position control. A data flow that is typical for DSPs and decoupled bearing control (see e.g. Schweitzer et al., 2003) is not the optimal one in the case of an FPGA-based implementation. With FPGAs, it is possible to achieve very short time delays, even for the centralized position control, and therefore simultaneous sampling of all position ADC channels and parallel communication are beneficial.

The different examples of the data flowcharts in AMB control are presented in Publication I. Regarding this, also a sequence diagrams for decentralized and centralized data flows are given in the publication.

5.3.2 Integrated actuator controller

In general, the accurate controllers of the actuators and PWM are often implemented in FPGAs or ASICs. The integrated actuator controller for an AMB rotor system is presented in Publication V. The major advantages of this design include the variable carrier frequency and the integration of the nonlinearity compensation. In addition, the high accuracy of the carrier signals (rate of comparisons) in the carrier-based PWM improves the modulation and accurate following of the current reference. The VHDL design utilizes a pipelined data flow and optimized fixed-point arithmetics. The operational principle is as follows. Firstly, the control currents are compensated according to the compensation surface in the interpolation block. Secondly, each compensated control current is changed into two positive reference currents (biasing). Thirdly, based on the reference and measured currents, ten voltage references are computed by the current controllers and passed to the modulator logic. Finally, the voltages in the modulator buffer are updated twice at the selected carrier frequency. The modulator logic comprises of two carrier counters and twenty comparators, which utilize the common carrier signal. The time resolution of the modulation is 10 ns, but the relative resolution of the comparators varies with the variable carrier frequency.

The overall input-to-output delay is minimized if the update rate of the inputs is synchronized with the update rate of the reference voltages in the modulator. In the prototyping platform, the selected carrier signal frequency was 20kHz, however, the VHDL design provided the variable carrier signal frequency in the range of 5-20kHz.

5.3.3 Upper control algorithms and interconnections

Concerning the outer position control loop implemented in the FPGA, the state-space equations can easily be implemented with the aforementioned IP for state-variable form (matrix-vector multiplication and matrix addition). Moreover, such an implementation strategy is flexible as it enables implementation of both centralized and decentralized position controllers, using the same AU structure.

The process of coding matrix parameters into the memory blocks of the Virtex II Pro is automated by the Matlab script.

It is important to notice that the required number of fractional bits in the utilized number format in the accumulator of the MAC unit grows with the number of included flexible modes. In addition, the number of required bits increases when the discretization time decreases. Under those circumstances, too short discretization times may not be practical and would require very long registers for the digital integrators. The required number formats for the implementation of state variable form in the FPGA can be found in Publication III. For the realization in dSPACE, the floating-point 32-bit number format proved sufficient for the implementation of the state observer of the rigid body rotor plus one flexible mode when the equations were in per-unit quantities.

The major operation frequency of the control design in Virtex II Pro was 100 MHz. However, the whole HDL design utilizes multiple clock domains: two different 100 MHz clock domains, 64 MHz, 16 MHz, and 4 MHz. Data and control signals are exchanged between different clock domains by means of synchronizers, FIFOs, and double-port RAM blocks. In the controller or emulator, the most significant input-to-output delay is introduced by the computation of state-variable form. Nevertheless, in the FPGA, when considering the implementation of the state-variable form based on the flexible rotor model, with four modes in xz- and four in yz-direction, the input-to-output delay equals to about 1000 clock cycles (10 μs).

This research did not involve an in-system testing of the implemented upper control loop in the FPGA. Owing to EMI, the operation of the custom ADC board was unreliable for higher DC link voltages. The AMB controllers presented in Chapter 4, were implemented using dSPACE and experimentally tested using FPGA-dSPACE-PC prototyping platform. In the prototyping platform the Virtex II Pro and the dSPACE are connected via Spartan II FPGA. The interconnections in the prototyping platform are discussed in Publication I.

5.3.4 Design testing, verification, and monitoring

When validating the control electronics and control software, the testing of programmable hardware parts of the embedded controller is especially difficult. The variety of problems may appear, including: hardware design issues, errors in signal conditioning (e.g. amplification, filtering, and conversion of measured signals), software coding errors, timing issues, problems with synchronization of different control units, and errors in data transfers. Increasing complexity of the control designs along with the growing size of the required FPGA brings the controller verification to even greater difficulty level. The testing of the FPGA design with the simulators becomes slow and not reliable enough for large amounts of signals and testing. The testing with the logic analyzer is also limited by the number of I/Os, and by the electromagnetic interferences which are inevitable when close to the power switches. Yet another possibility are commercial debugging tools. For example, Xilinx provides its own embedded logic analyzer, namely ChipScope Pro. This tool allows a real-time debugging at the operating system speed. However, it is not sufficient for real-time monitoring. Yet another interesting testing solution is combining a Matlab Simulinks environment and ModelSim, as shown by Rauma et al. (2003).

In the testing of a control application, the main concern is tracing of the selected internal signals, such as control states. This can be achieved by using remaining resources of the FPGA to implement internal logic analyzer that first, records on demand the state of certain signals (buses or registers), and second, sends the recorded data to the host computer. In addition, by using more than one configuration file (e.g., stored on a flash memory card), some extra testing features, which normally do not fit into the FPGA chip, may be utilized in different implementations.

A feasible solution for realization of an internal data acquisition is the embedded processor that collects the data and then sends it to the host PC for further analysis. In particular, a solution, which is straightforward and efficient in terms of the utilized resources (for the PowerPC processor in Xilinx's FPGA) is to access internal logic signals through the shared double-port memory-block. One side of the block interfaces to the control logic and the other one to the On-Chip Memory (OCM) bus of the embedded processor. The bus connects to the PowerPC processor, which uses a Processor's Local Bus (PLB) to communicate with the peripherals (e.g. Ethernet IP, external SDRAM interface). In the case of recording longer time intervals, data are captured and sent to the external memory, and then they can be transferred to the host PC via the Ethernet. On the host PC, a client user interface program allows the access to the gathered data. The details of the solution can be found in Publication VI.

5.3.5 FPGA-based emulation

An intermediate step between the software simulations and the in-system validation is the FPGA-based emulation. The emulation of the plant is especially useful in situations when the controlled system is not easily available for testing or when it is a source of errors itself. The emulator may be used for the validation of the whole control system or its particular components.

In general, the AMB rotor emulator comprises two IP cores: the nonlinear force-field interpolation IP core and the arithmetic unit for computing state-variable form IP core. The emulator can take into account the noncollocation of the sensors and actuators. The real-time FPGA-based emulator of the plant with a rigid rotor model is presented in Publication II and with a flexible rotor model in Publication III.

5.4 Summary

When considering the pure computational power that is necessary in the time-crucial portions of the control algorithm, the use of an FPGA can improve the control system performance compared with a typical (only DSP-based) control platform. Despite this fact, a powerful floating-point DSP and a medium-size FPGA assembled on a single board seem to provide an almost even solution compared with a single large FPGA chip. Therefore, in most control applications, the choice between these two alternatives depends more on the designer's preferences and available tools than on the price or performance.

In FPGAs, the internal architecture can be freely configured and optimized to produce parallel multiply-accumulate units, in which the number and bit-length of the word are only limited by the available resources (typically hardware multipliers and internal DSP blocks). Similarly to the growing size of memories, also the size of FPGAs is constantly growing. Now, the size of the internal memory blocks of larger FPGAs seems to be more than enough for the embedded applications. These internal FPGA memory blocks and registers are crucial to efficient parallel data flow in the control application. As the memories are placed between the DSP blocks, there is not much latency when accessing them, hence there is no bottleneck in FPGA, which would limit the performance, as in a standard microcontroller. In addition to that, as a result of the negligible computational delay, the simultaneous sampling of all ADC channels is possible. Such a simultaneous sampling is best suited for the centralized model-based controller implementation in FPGA.

Unfortunately, there are not only advantages in the use of FPGAs in embedded AMB applications. First of all, design environments and a realization of programmable hardware-software co-design in FPGAs require more effort and are more time-consuming than in the case of DSPs. In addition, the realization of a flexible, high-level user interface (that is an inevitable prerequisite, e.g. for debugging, monitoring, calibration, etc.) is more difficult to obtain (both to purchase or to make) on FPGAs than on DSPs. Therefore, the tasks that are not time critical – system monitoring, calibration, debugging, and communication, are best suited to be carried out in a DSP or even a more general microcontroller that is placed outside or inside an FPGA chip.

To sum up, the research on the presented subject was only possible owing to the recent developments in high-scale signal processing devices, namely FPGAs. This study proves that FPGAs are a viable alternative to the DSP control platforms. With the emerging more matured tools and high-level design methods, the FPGAs constitute a better target (more flexible and with greater capabilities) for complex control algorithms than DSPs.

Chapter 6

Conclusions

The thesis is concluded by a summary of the main objectives of the work, contributions, and their significance. The outlook for future research work is given.

6.1 Summary

In the work, the major objectives stated in Chapter 1 were met. The use of FPGAs as an implementation target for the real-time high performance AMB rotor controller was presented. The working solution of the FPGA-dSPACE-PC based prototyping platform was built, tested and validated in laboratory conditions. The complex model-based and nonlinear control algorithms, which can benefit form a flexible FPGA control platform were studied.

6.1.1 Control design

In regard to the control structure, the design of the model-based controller employed LQ methods for high-performance control, in terms of precise reference following and disturbance force rejection. Moreover, the model-based AMB controller took into account the bending modes of the rotor, their controllability, and nonlinearities of the actuator.

The LQ design guided by the physical quantities gave an advantage over a pole placement method. The utilized method (Bryson's rules complemented by the suitably augmented plant models) for selecting the optimal weighting matrices automated the control design procedure. The applied methods were proved appropriate for the studied application.

The employment of the force-field compensation (Publication IV and V) decreased the uncertainty of the actuator and, hence the performance and the stability of the control system were improved. Nevertheless, the efficiency of the compensation methods is limited by the accuracy of the numerical data. As an alternative to a typically applied inverse nonlinearity, used in a force-field compensation, a new model reference method was proposed.

In the SISO system, the LQ control proved to be better for the servo problem than the PID and PD/PI control. In spite of this, for the plant models neglecting the mechanical resonances, lower-order controllers are faster than observer-based controllers and provide better (faster) responses to step disturbance. In the

MIMO case, it was shown that the centralized LQ control is superior to the conventional PID-based control in terms of performance, stability margins, and automated design. In the studied rotor, the gyroscopic effect had no significant influence on the unbalance responses of the multiple SISO and MIMO control.

The gyroscopic effect was relatively weak, and therefore a centralized control did not provide a significant advantage over a decentralized one, with respect to closed-loop performance. Nevertheless, using the centralized LQ-based controller improves stability margins.

As an option, the controller could include an additional disturbance-observer-based unbalance compensation, for canceling the magnetic force vibrations or for canceling vibration in the measured positions. The principles behind such an compensation of unbalance are well known, however the use of such a compensation method in AMB application is not widely reported.

For the obtained controller, robust stability and performance were analyzed. Finally, conditioning of the mathematical model and comparison of design methods for discrete-time control (different discretized time-continuous designs with a time-discrete design) were briefly discussed (more discussion was given in Publication III).

6.1.2 FPGA-based implementation

One of the practical outcomes of the presented work was the FPGA-dSPACE-PC prototyping platform. The FPGA implementation included PWM of twenty carrier-based modulated signals for power switches in the amplifiers, communication and synchronization with dSPACE that is used for rapid prototyping and control design, connection to a PC, connection via Virtex's BRAMs to the on-chip PowerPC (used for a real-time monitoring and debugging), and the frame for data flow of the outer-loop position controller.

Additionally, the FPGA emulator for the AMB rotor system was implemented in VHDL and tested in ModelSim simulator (Publications II and III). Furthermore, the controller and emulator included the generic IPs of piecewise interpolation-based model of the AMB force field (Publication II and V) and the rotor model in state-variable form, implemented in VHDL. The FPGA emulation allowed a built-in-chip testing of the FPGA controller.

The utilized application-specific communication architecture of System-on-a-chip (SoC) design was sufficient for the AMB controller (Publication I). The proper per-unit scaling allowed a relatively compact fixed-point implementation of the state-variable form in VHDL. Furthermore, the presented work enabled a design of the single chip solution for an AMB controller.

In summary, this study proved that both the inner-current control and the outer-position one are suitable to be implemented in a single FPGA. With the use of large FPGAs, the complexity of the controller and the required computational power are no longer a limiting factor, in regard to achieved performance. As a consequence, the AMB control system can benefit from the utilization of FPGAs.

6.2 Outlook

The outlook for the control algorithms, which efficiently utilize the FPGAs in AMB control is bright. Computationally heavy control algorithms can be implemented without fear for the limited computational power, number of I/Os or inaccurate number formats as might be a case with DSPs. With its flexible architectures, the modern and large FPGAs could accommodate very complex controllers. However, too high complexity may lead to error-prone design that is difficult to debug, modify and maintain.

As regards to the AMB prototype, control electronics and control algorithms, the recommendations for future work, from the point of view of the presented thesis (considered as a starting point), are as follows.

- The laboratory tests of the AMB rotor system should be continued.
- The unbalance compensation should be tested experimentally, after installation of a speed sensor.
- The employment of robust control methods, their computational complexity requirements and benefits over LQ methods should be examined.
- The automated system identification and, based on it, automated MIMO-adaptive nonlinear controller design could be applied.
- The improvements in position sensors are required; the design of custom, more affordable, accurately positioned and calibrated sensors could considerably reduce the costs of control electronics and rise the quality of a feedback signal.

As to the suggestions for future research work, which involves FPGA-based AMB controllers, the accent should fall on the following topics.

- In the implementation with the use of FPGA, the high-level C-based languages, other high-level design environments, and ready-made IP libraries for hardware-software co-design could alleviate the growing complexity and workload in SoC design, releasing the researcher and control engineer from tedious VHDL coding.
- The custom-built in-chip interconnections and buses between IPs could be replaced with more generic structures (e.g. bus structure such as presented by Rauma et al., 2005). For SoC, which are more complex than the studied prototype, a network-on-a-chip (NoC) could be considered. The NoC, that might consist of multiple point-to-point data links connected by switches (routers), applies communication methods similar to telecommunications networks for connecting processor cores, memories, and IP blocks.
- Further evaluations of the single-chip-embedded FPGA-based AMB controller should be carried out. In order to achieve more additional experimental results, an improved user interface, integrated debugging interface, and monitoring are required.
- The application of floating-point arithmetic in the IP for a state-variable form realization would increase the accuracy of the solution. The AU for

the state-variable form with Ω as a parameter and the real-time discretization could be implemented.

- The development of a kind of an IDE application to provide facilities to software engineer for automated design of complex model-based controllers on a single FPGA could be considered. Such an IDE would possibly combine the MATLAB control toolboxes (for control design) with a programming environment (for automated code generation) for a hardware-software controller implementation in FPGA.

Bibliography

B. Aeschlimann (2002). *Control Aspects of High Precision Active Magnetic Bearings.* EPFL, Lausanne, Switzerland. Diss., No. 2489.

M. Ahrens, et al. (1996). 'Performance of a magnetically suspended flywheel energy storage device'. *IEEE Transactions on Control Systems Technology* **4** (5): pp. 494–502.

M. Antila (1998). *Electromechanical Properties of Radial Active Magnetic Bearings.* Helsinki University of Technology, Finland. Diss., EI 92.

A. Arkkio, et al. (2004). 'Electromechanical Interactions in Electrical Machines'. Lecture series 14, Helsinki University of Technology, Otaniemi, Finland.

K. J. Åström and B. Wiettenmark (1997). *Computer-Controlled Systems.* Prentice-Hall Inc., Upper Saddle River, New Jersey 07458.

G. Balas, et al. (2007). *Robust Control Toolbox 3 User's Guide.* San Diego, California, USA.

M. J. Balas (1978). 'Feedback Control of Flexible Systems'. *IEEE Transactions on Automatic Control* **23** (4): pp. 673–679.

J. Beams and F. Holmes (1941). 'Suspension of rotatable bodies'. U.S. Patent No. 2256937.

F. Betschon (2000). *Design Principles of Integrated Magnetic Bearings.* Swiss Federal Institute of Technology, Zurich, Switzerland. Diss. ETH Nr. 13643.

H. Bleuler (1984). *Decentralized Control of Magnetic Rotor Bearing Systems.* Swiss Federal Institute of Technology Zurich, Switzerland. Diss. ETH Nr. 7573.

H. Bleuler, et al. (1994). 'Application of Digital Signal Processors for Industrial Magnetic Bearings'. *Transactions on Control Systems Technology* **2** (4): pp. 280–289.

J. Boehm, et al. (1993). 'Sensors for magnetic bearings'. *IEEE Transactions on Magnetics* **29** (6, Part 2): pp. 2962–2964.

M. Brunet (1988). 'Practical Applications of the Active Magnetic Bearings to the Industrial World'. In *Proceedings of the first International Symposium on Magnetic Bearings*, pp. 224–244, Zurich, Switzerland.

M. Brunet (2007). 'S2M Change of Control'. Retrived Oct 2007, Available: http://www.s2m.fr/E/1-COMPANY/news-SKF.html.

D. Buell, et al. (2007). 'Guest Editors' Introduction: High-Performance Reconfigurable Computing'. *Computer* **40** (3): pp. 23–27.

W. J. Chen and E. J. Gunter (2005). *Introduction to Dynamics of Rotor-Bearing Systems*. Trafford Publishing, Victoria, Canada, Charlottesville.

L. Cristaldi, et al. (2001). 'A linearization method for commercial Hall-effect current transducers'. *IEEE Transactions on Instrumentation and Measurement* **50** (5): pp. 1149–1153.

M. Dussaux (1990). 'The Industrial Applications of the Active Magnetic Bearings Technology'. In *Proceedings of the second International Symposium on Magnetic Bearings*, pp. 33–38, Tokyo, Japan.

S. Earnshaw (1842). 'On the nature of the molecular forces which regulate the constitution of the luminferous ether'. *Transactions of the Cambridge Philosophical Society* **7**: pp. 97–112.

M. D. Ercegovac and T. Lang (2004). *Digital Arithmetic*. Morgan Kaufmann, USA.

Foster-Miller, Inc. (2007). 'Maglifter'. Retrived Oct 2007, Available: http://www.foster-miller.com/projectexamples/t_electromagnetics_electric_machines/maglifter.htm.

G. F. Franklin, et al. (1998). *Digital Control of Dynamic Systems*. Addison Wesley, third edn.

G. Genta (2005). *Dynamics of Rotating Systems*. Springer, New York, USA.

G. Genta, et al. (1993). 'Active Magnetic Bearing Control Loop Modeling for a Finite Element Rotordynamics Code'. In *Proceedings of the Second International Symposium on Magnetic Suspension Technology*, pp. 319–333, Seattle, Agosto.

P.-H. Giang, et al. (1988). 'An Enhancement of the TMS32010 Digital Signal Processor in a NS32016 Microcomputer System'. In *IEEE Proceedings of the Region 5 Conference: Spanning the Peaks of Electrotechnology*, pp. 126–128, Colorado Springs, CO, USA.

M. Glaser and D. Sandagol (2006). 'Automatic Initial Levitation with Active Magnetic Bearings'. In *Proceedings of the Tenth International Symposium on Magnetic Bearings*, vol. CD-proceedings, Martigny, Switzerland.

H. Goma (2000). *Designing Concurrent, Distributed, and Real-Time Applications with UML*. Addison-Wesley, USA.

W. Grega and A. Piłat (2005). 'Comparison of Linear Control Methods for an AMB System'. *International Journal of Applied Mathematics and Computer Science* **15** (2): pp. 245–255.

T. Grochmal and A. Lynch (2006). ‘Vibration compensation and precision tracking of a rotating shaft by nonlinear state feedback’. In *Proceedings of the Tenth International Symposium on Magnetic Bearings*, vol. CD-proceedings, Martigny, Switzerland.

H. Habermann and G. Liard (1979). ‘Practical Magnetic Bearings’. *IEEE Spectrum* **16** (9): 26 p.

T. Hiroe, et al. (1993). ‘A new method for selecting weighting matrices of LQ regulators and its application to an industrial turbine’. In *IEEE Proceedings of the 32nd Conference on Decision and Control*, vol. 4, pp. 3333–3334.

K.-J. Hoffmann, et al. (1998). ‘Integrated Active Magnetic Bearings’. In P. E. Allaire (ed.), *Proceedings of the Sixth International Symposium on Magnetic Bearings*, pp. 256–265. Technomic Publ. Lancaster/Basel.

J. Holtz (1992). ‘Pulsewidth Modulation - a Survey’. *IEEE Transactions on Industrial Electronics* **39** (5): pp. 410–420.

M. Humphrey, et al. (1999). ‘Experiences using RT-Linux to implement a controller for a high speed magnetic bearing system’. In *IEEE Proceedings of the Real-Time Technology and Applications Symposium*, pp. 121–130.

R. Jastrzębski, et al. (2004b). ‘Real-time Emulation of Induction Motor in FPGA using Floating Point Representation’. In *Proceedings of the Thirteenth IASTED International Conference on Applied Simulation and Modelling*, pp. 226–231, Rhodes, Greece.

R. Jastrzębski, et al. (2004a). ‘FPGA Based Platform for Real-Time Testing of Fast Induction Motor Controllers’. In *Proceedings of the Eleventh International Conference on Mixed Design of Integrated Circuits and Systems*, pp. 491–496, Szczecin, Poland.

R. Jastrzębski, et al. (2003). ‘Implementation and Simulation of Fast Inverter Control Algorithms with the use of FPGA Circuit’. In *Proceedings of the 2003 Nanotechnology Conference and Trade Show*, vol. 2, pp. 238–241, San Francisco, USA.

A. Kärkkäinen, et al. (2006). ‘Transient Simulation of AMB Supported Electric Motor during Rotor Drop on Retainer Bearings’. In *Proceedings of the Tenth International Symposium on Magnetic Bearings*, vol. CD-proceedings, Martigny, Switzerland.

A. Katoh and T. Masuzawa (2006). ‘Optimized design for a hybrid magnetic bearing for the artificial heart’. In *Proceedings of the Tenth International Symposium on Magnetic Bearings*, vol. CD-proceedings, Martigny, Switzerland.

H. Kemper (1937). ‘Overhead suspension railway with wheelless vehicles employing magnetic suspension from iron rails’. German Patent No. 643316, 644302.

C. R. Knospe and E. G. Collins (1996). ‘Introduction to the Special Issue on Magnetic Bearing Control’. *IEEE Transactions on Control Systems Technology* **4** (5): pp. 481–483.

C. R. Knospe, et al. (1997). 'Multitasking DSP Implementation of Adaptive Magnetic Bearing Control'. *IEEE Transactions on Control Systems Technology* **5** (2): pp. 230–238.

F. Krach, et al. (2003). 'FPGA-Based Implementation of Digital Control for a Magnetic Bearing'. In *IEEE Proceedings of the American Control Conference*, vol. 2, pp. 1080–1085.

P. C. Krause and O. Wasynczuk (1989). *Electromechanical Motion Devices.* McGraw-Hill Book Co., New York, USA.

E. Lantto (1997). 'Finite Element Model for Elastic Rotating Shaft'. Tech. Rep. EI 88, Helsinki University of Technology, Finland.

E. Lantto (1999). *Robust Control of Magnetic Bearings in Subcritical Machines.* Helsinki University of Technology, Finland. EI 94.

J. Larjola (ed.) (1988). *Proceedings of the Conference on High Speed Technology*, Lappeenranta, Finland. Lappeenranta University of Technology.

R. Larsonneur (1990). *Design and Control of Active Magnetic Bearing Systems for High Speed Rotation.* Swiss Federal Institute of Technology Zurich, Switzerland. Diss. ETH Nr. 9140.

F. Lewis and V. Syrmos (1995). *Optimal Control, 2^{nd} ed.* John Wiley and Sons, New York, USA.

G. Li, et al. (2006). 'A Note on ISO AMB-Rotor System Stability Margin'. In *Proceedings of the Tenth International Symposium on Magnetic Bearings*, vol. CD-proceedings, Martigny, Switzerland.

F. Lösch (2002). *Identification and Automated Controller Design for Active Magnetic Bearing Systems.* Swiss Federal Institute of Technology Zurich, Switzerland. Diss. ETH Nr. 14474.

K.-Y. Lum, et al. (1996). 'Adaptive Autocentering Control for an Active Magnetic Bearing Supporting a Rotor with Unknown Mass Imbalance'. *IEEE Transactions on Control Systems Technology* **4** (5): pp. 587–597.

R. Małecki (1996). 'Fatherland of a cart: Europe or the Middle East [Ojczyzna Wozu: Europa czy Bliski Wschód]'. *Wiedza i Życie, in Polish* **[Online]**. Retrived Feb 2007, Available: http://archiwum.wiz.pl/1996/96083600.asp.

N. Mohan, et al. (1995). *Power Electronics: Converters, Applications and Design, 2^{nd} ed.* John Wiley and Sons, New York, USA.

J. Nerg, et al. (2005). 'Modelling the Force versus Current Characteristics, Linearized Parameters and Dynamic Inductance of Radial Active Magnetic Bearings Using Different Numerical Calculation Methods'. *WSEAS Transactions on Circuits and Systems* **4** (6): pp. 551–559.

K. Nonami and T. Ito (1996). 'μ synthesis of flexible rotor-magnetic bearing systems'. *IEEE Transactions on Control Systems Technology* **4** (5): pp. 503–512.

C. Oberbeck and H. Ulbrich (2002). 'Investigations in a Software-based Design of Linear Electromagnetic Actuators'. In *Proceedings of the Eight International Symposium on Magnetic Bearings*, pp. 157–162, Mito, Japan.

A. Piłat (2002). *Control of magnetic levitation systems* [*Sterowanie układami magnetycznej lewitacji*]. AGH - University of Science and Technology, Cracow, Poland, in Polish.

B. Polajzer, et al. (2006). 'Decentralized PI/PD position control for active magnetic bearings'. *Electrical Engineering* **89** (1): pp. 53–59.

B. Polajzer, et al. (2004). 'Impact of magnetic nonlinearities and cross-coupling effects on properties of radial active magnetic bearings'. *IEEE Transactions on Magnetism* **40** (2, Part 2): pp. 798–801.

R. Pöllänen, et al. (2005). 'Reluctance network method based dynamic model of radial active magnetic bearings'. In *Proceedings of the IEEE International Conference on Magnetics*, pp. 1429–1430, Nagoya, Japan.

R. Pöllänen, et al. (2006). 'Transient Thermal Model for Radial Active Magnetic Bearing'. In *Proceedings of the Tenth International Symposium on Magnetic Bearings*, vol. CD-proceedings, Martigny, Switzerland.

W. Popoli (2000). 'Spindle Bearing Basics the key to spindle performance'. *Manufacturing Engineering* **125** (5). Retrived Mar 2007, Available: http://www.sme.org.

K. Rauma (2006). *FPGA-based Control Design for Power Electronic Applications.* Lappeenranta University of Technology, Finland.

K. Rauma, et al. (2005). 'New Bus Structure for Programmable Logic Devices Controlling Power Electronics'. In *IEEE Proceedings of the Power Electronics Specialists Conference*, pp. 2705–2708, Recife, Brazil.

K. Rauma, et al. (2003). 'Simulation and Verification of HDL based Design in Simulink'. In *IASTED Proceedings of the International Conference on Applied Simulation and Modelling*, pp. 472–477, Marbella, Spain.

M. Ren, et al. (2006). 'Zero Bias H_∞ Control of Flexible Rotor Magnetic Bearing Flywheel System with Gyroscopic Effect Using Singular Value Decomposition'. In *Proceedings of the Tenth International Symposium on Magnetic Bearings*, vol. CD-proceedings, Martigny, Switzerland.

D. M. Schneider (1988). 'Control of processes with time delays'. *IEEE Transactions on Industry Applications* **24** (2): pp. 186–191.

P. Schroder, et al. (1998). 'Online genetic auto-tuning of mixed H2/H8 optimal magnetic bearing controllers'. In *IEEE Proceedings of the International Conference on Control*, vol. 2, pp. 1123–1128.

T. Schuhmann, et al. (2006). 'Adaptive Linear and Extended Kalman Filter applied to AMB with Collocated Position Measuring'. In *Proceedings of the Tenth International Symposium on Magnetic Bearings.* CD-proceedings.

A. Schulz, et al. (2006). 'A Reliability Analysis of Switching Amplifier Concepts for Active Magnetic Bearings'. In *IEEE Proceedings of the International Conference on Industrial Technology*, vol. CD-proceedings, Mumbai, India.

G. Schweitzer, et al. (2003). *Active Magnetic Bearings.* Authors Working Group, reprint, Zurich.

G. Schweitzer and R. Lange (1976). 'Characteristics of a Magnetic Rotor Bearing for Active Vibration Control'. In *Proceedings of the First International Conference on Vibrations in Rotating Machinery*, no. C239/76, p. 301.

SKF (2003). *Eddy Probe Systems.* San Diego, California, USA. Retrived Feb 2007, Available online: http://www.skf.com/files/266262.pdf.

N. Skricka and R. Markert (2002). 'Improvements in the Integration of Active Magnetic Bearings'. *Control Engineering Practice* **10** (8): pp. 917–922.

J.-J. E. Slotine and W. Li (1991). *Applied Nonlinear Control.* Prentice Hall, Englewood Cliffs, New Jersey.

Y. Sun, et al. (2006). 'Magnetic Force of Radial Magnetic Bearing Considering Eddy Currents Effect'. In *Proceedings of the Tenth International Symposium on Magnetic Bearings*, vol. CD-proceedings, Martigny, Switzerland.

Y. Suyuan, et al. (2006). 'Application and Research of the AMB in the Nuclear Power Plant of HTR'. In *Proceedings of the Tenth International Symposium on Magnetic Bearings*, vol. CD-proceedings, Martigny, Switzerland.

N. Takahashi, et al. (2007). 'An Evaluation of Stability Indices Using Sensitivity Functions for Active Magnetic Bearing Supported High-Speed Rotor'. *Transactions of the ASME, Journal of Vibration and Acoustics* **129**: pp. 230–238.

The Math Works Inc. (1999). *Control System Toolbox User's Guide, Version 4.2.* San Diego, California, USA.

A. Turing (1936). 'On Computable Numbers, With an Application to the Entscheidungsproblem'. In *Proceedings of the London Mathematical Society*, vol. 42 of *2*, pp. 173–198.

R. Volkert, et al. (2006). 'Position Controller with Hysteresis Compensation for Magnetic Bearings'. In *Proceedings of the Tenth International Symposium on Magnetic Bearings*, vol. CD-proceedings, Martigny, Switzerland.

B. Wagner (1988). 'Active Magnetic Bearings, Theory'. In *Proceedings of the Conference on High Speed Technology*, pp. 117–128, Lappeenranta, Finland.

J. Wassermann, et al. (2003). 'Active Magnetic Bearings of High Reliability'. In *IEEE Proceedings of the International Conference on Industrial Technology*, vol. 1, pp. 194–197, Maribor, Slovenia.

P. Wurmsdobler (1997). *State Space Adaptive Control for a Rigid Rotor Suspended in Active Magnetic Bearings.* Vienna University of Technology, Vienna, Austria.

Xilinx, Inc. (1994-2007). 'How Xilinx Began'. Retrived Mar 2007, Available: http://www.xilinx.com/company/history.htm.

T. Yamamoto and Y. Ishida (2001). *Linear and nonlinear rotordynamics a modern treatment with applications*. John Wiley and Sons, New York, USA.

J. Zhang and N. Karrer (1995). 'IGBT Power Amplifiers for Active Magnetic Bearings of High Speed Milling Spindles'. In *IEEE Proceedings of the International Conference on Industrial Electronics, Control, and Instrumentation*, vol. 1, pp. 596–601.

Y. N. Zhuravlyov (2000). 'On LQ-Control of Magnetic Bearing'. *IEEE Transactions on Control Systems Technology* **8** (2): pp. 344–350.

Y. N. Zhuravlyov, et al. (1994). 'Inverse problems of magnetic bearing dynamics'. In *Proceedings of the fourth International Symposium on Magnetic Bearings*, pp. 79–84, Zurich, Switzerland.

Appendix A

Derivations and algorithms

A.1 Electromagnetic force

The equation for the magnetic force (2.7) can be obtained from a principle of virtual work (Antila, 1998) and (Arkkio et al., 2004). The virtual mechanical work done by the system W_{me}, the energy of electromagnetic field W_{fe}, and the total energy of the windings are used in the energy balance of a generalized electromechanical system with N circuit equations as

$$\sum_{j=1}^{N} i_j d\psi_j = dW_{\mathrm{fe}} + dW_{\mathrm{me}} = dW_{\mathrm{fe}} + \mathbf{f} \cdot d\mathbf{l}, \tag{A.1}$$

where i_j, ψ_j and $d\mathbf{l}$ are the currents of the circuits, flux linkages of the circuits and the virtual displacement. Considering the displacement and the acting force in x direction, and defining the vector containing all the currents in the system as $\mathbf{i}$, the energy and flux linkage differences can be written as

$$dW_{fe} = \sum_{j=1}^{N} \frac{\partial W_{\mathrm{fe}}(\mathbf{i}, x)}{\partial i_j} di_j + \frac{\partial W_{\mathrm{fe}}(\mathbf{i}, x)}{\partial x} dx, \tag{A.2}$$

$$d\psi_j = \sum_{j=1}^{N} \frac{\partial \psi_j(\mathbf{i}, x)}{\partial i_j} di_j + \frac{\partial \psi_j(\mathbf{i}, x)}{\partial x} dx. \tag{A.3}$$

Now, we assume the currents as free variables such that $\mathbf{i}$ =constant. Substituting differences in Eq. (A.1) and noticing that $\mathbf{i}$ and x are independent from each other, the force equation is obtained as the partial derivative of a co-energy with respect to virtual movement

$$f(\mathbf{i}, x) = \sum_{j=1}^{N} i_j \frac{\partial \psi_j(\mathbf{i}, x)}{\partial x} - \frac{\partial W_{\mathrm{fe}}(\mathbf{i}, x)}{\partial x} = \frac{\partial W_{\mathrm{ce}}(\mathbf{i}, x)}{\partial x}, \tag{A.4}$$

where the electromagnetic co-energy is defined as

$$W_{\mathrm{ce}} = \sum_{j=1}^{N} i_j \psi_j - W_{\mathrm{fe}}(\mathbf{i}, x). \tag{A.5}$$

A.2 Magnetic energy in RNM

The electromagnetic energy stored in the RNM equals to the sum of the magnetic energies stored in the M branches of the model as

$$W_{\mathrm{fe}} = \int\limits_{V} \int\limits_{0}^{\mathbf{B}} \mathbf{H} d\mathbf{B} dV = \sum_{j=1}^{M} V_j \int\limits_{0}^{\Phi_j} \frac{B_j}{\mu_0 \mu_j S_j} d\Phi_j, \tag{A.6}$$

where $B_j = \Phi_j / S_j$ and $V_j = S_j l_j$. Now, using general volume reluctances (3.37) we obtain

$$W_{\mathrm{fe}} = \sum_{j=1}^{M} \int\limits_{0}^{\Phi_j} \Phi_j \Re_j d\Phi_j = \sum_{j=1}^{M} \frac{1}{2} \Phi_j \Re_j \Phi_j, \tag{A.7}$$

which in the matrix notation becomes

$$W_{\mathrm{fe}} = \frac{1}{2} \mathbf{\Phi}_{\mathrm{m}}^{\mathrm{T}} \mathbf{\Re} \mathbf{\Phi}_{\mathrm{m}}. \tag{A.8}$$

A.3 Calibration of position sensors

Measuring the rotor position in xy coordinates

In the prototype, there are two differential position sensors at one end of the rotor (end-A) and three single-channel position sensors at the other end of the rotor (end-B), according to Fig. 3.6. Assuming the origin of the coordinate system in the center of the stator and placing the differential sensors on the x and y axes of the system results in the direct measurements of the rotor center at the end-A. The single-channel sensors are equally placed in the stator frame every 120° at the end-B (Fig. A.1). Therefore, obtaining the rotor center (x_{m}, y_{m}) at the end-B requires utilizing the geometry properties of the circle (rotor circumference) circumscribed around the triangle formed by three measured points ($x_{k\mathrm{m}}$, $y_{k\mathrm{m}}$).

We draw the straight lines from the sensors to the center of the stator; they are the sensing lines, indicated by dashed lines in Fig. A.1. The three points of the intersections between the sensing lines and the rotor circumference (we call them measured points) are

$$(x_{1\mathrm{m}}, y_{1\mathrm{m}}) = (r - l_{\mathrm{air1}}, 0), \tag{A.9}$$

$$(x_{2\mathrm{m}}, y_{2\mathrm{m}}) = \left(-\frac{1}{2}(r - l_{\mathrm{air2}}), \frac{\sqrt{3}}{2}(r - l_{\mathrm{air2}})\right), \tag{A.10}$$

$$(x_{3\mathrm{m}}, y_{3\mathrm{m}}) = \left(-\frac{1}{2}(r - l_{\mathrm{air3}}), -\frac{\sqrt{3}}{2}(r - l_{\mathrm{air3}})\right), \tag{A.11}$$

where the l_{air1}, l_{air2}, l_{air3}, r are measured air-gaps and the radius of the rotor. After some transformations, the measured center of the rotor in the xy coordinates is given by

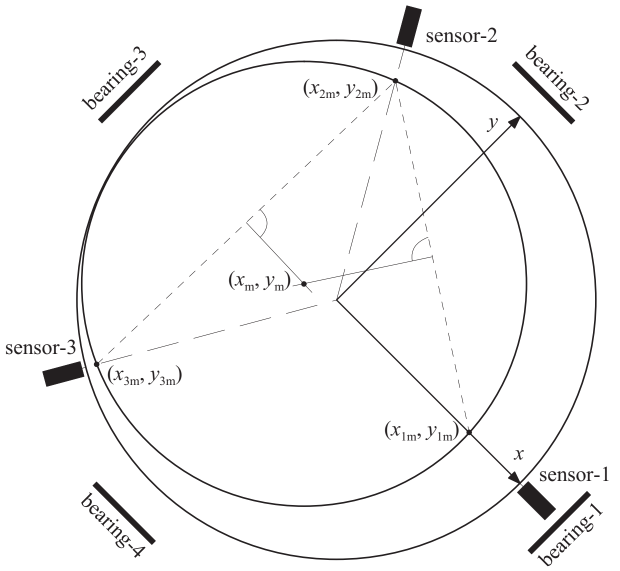

Figure A.1: Single-channel sensors are equally placed in the stator frame, at the end-B of the rotor, at every 120°. The coordinates of the rotor center $(x_\mathrm{m}, y_\mathrm{m})$ can be obtained from the geometry properties of the circle.

$$x_\mathrm{m} = \frac{a_1 a_2 \left(y_{2\mathrm{m}} - y_{3\mathrm{m}}\right) + a_2 \left(x_{2\mathrm{m}} + x_{1\mathrm{m}}\right) - a_1 \left(x_{1m} + x_{3\mathrm{m}}\right)}{2\left(a_2 - a_1\right)}, \tag{A.12}$$

$$y_\mathrm{m} = \frac{a_2 \left(y_{1\mathrm{m}} - y_{3\mathrm{m}}\right) - a_1 \left(y_{2\mathrm{m}} + y_{1\mathrm{m}}\right) + \left(x_{3m} - x_{2\mathrm{m}}\right)}{2\left(a_2 - a_1\right)}, \tag{A.13}$$

where the coefficients a_1 and a_2 are

$$a_1 = \frac{\left(y_{1\mathrm{m}} - y_{2\mathrm{m}}\right)}{\left(x_{1\mathrm{m}} - x_{2\mathrm{m}}\right)},\ a_2 = \frac{\left(y_{3\mathrm{m}} - y_{1\mathrm{m}}\right)}{\left(x_{3\mathrm{m}} - x_{1\mathrm{m}}\right)}. \tag{A.14}$$

Errors in the measured rotor position

Let us examine the effects of four error sources on the measured rotor position. Assuming the three single-channel sensors, the first and second examined errors are gain and offset errors. The third is an error in the position of the sensor in the stator frame (deviation from 120° equal distribution of the sensors, α angle measured in degrees). The fourth is the inaccurate direction of the tip of the sensor (angle δ between the ideal sensing line and the actual sensing line), as presented in Fig. A.2.

In order to determine how these errors influence the calculated position of the rotor, we compare the obtained air-gaps from the ideally placed sensors with the air-gaps of the deviated sensors. The influence of different error types on the calculated center of the rotor is presented in Fig. A.3.

When considering the accuracy of the measured rotor position, the least important but nonlinear relation exhibits the error in the angle δ. The calculated

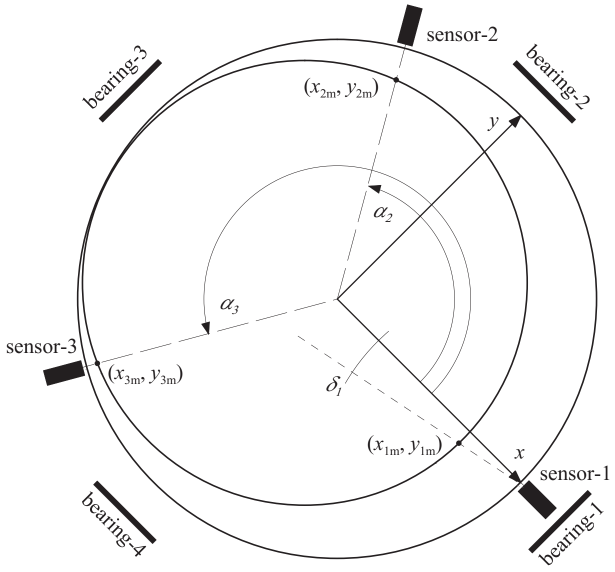

Figure A.2: Two types of errors in the position of the sensors are depicted, i.e., an error in the direction of the tip of the first sensor δ_1 and discrepancy in 120° distribution of the sensors two and three (α_2, α_3), in the stator frame.

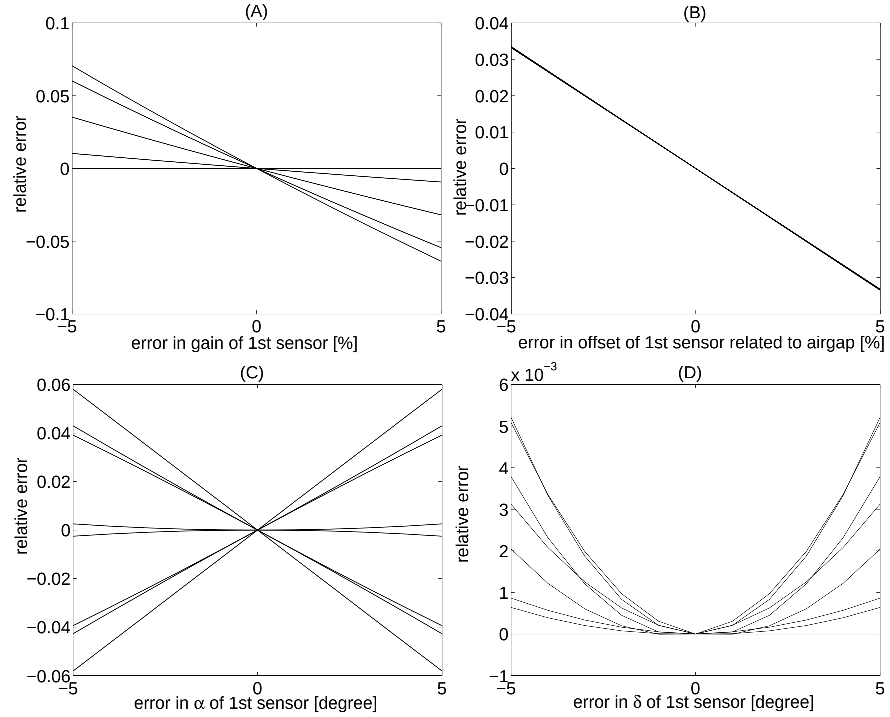

Figure A.3: Relative errors in the measured position of the rotor (in relation to the average air-gap) are presented. The results correspond to the errors in measured x_{m} for 8 different rotor positions at the end-B.

xy position of the rotor depends mostly on the gain, then on the offset, and finally on the accuracy of sensor orientation α. The errors in the gain and offset can be compensated by first-order polynomial approximation.

Calculating the gain and offset

The gain and offset scaling could be based on the measured air-gaps, the expected air-gaps that are computed according to the dimensions of the test rotor from Table A.1 (e.g. for four different rotor positions) and by least squares approximation. The following procedure is proposed for calculating the gain and offset values:

1. By using the open-loop biasing currents, the center line of the rotor is moved to four different positions $(x,\, y)$: $(l_{\text{bias}},\, 0)$, $(0,\, l_{\text{bias}})$, $(-l_{\text{bias}},\, 0)$, $(0,\, -l_{\text{bias}})$, where l_{bias} is the clearance, between the safety bearings and the rotor.

2. At each position, the measured air-gaps are stored in the table. The rotor is moved as to make $0.5k$ circles according to the clock direction and $0.5k$ circles in the counter clock direction, where k is integer and $k \geq 2$.

3. The expected ideal air-gaps are calculated assuming no errors in the measurements and position of the sensors.

4. The measured air-gaps and the corresponding calculated ideal ones (expected) are stored in two vectors $\mathbf{x}$ and $\mathbf{y}$, respectively. Using the least squares approximation, the gains and offsets are computed for each sensor individually. The equations suitable for the implementation are listed below.

    (a) Let us define the measured position function for a single sensor as: $x_{\text{m}} = F(x) = \theta_1 x + \theta_0$, where the θ_1, and θ_2 are the gain and offset. Then, we can calculate the Jacobean matrix $\boldsymbol{J}$ of the sensor function for each measurement k as

    $$\boldsymbol{J} = \begin{bmatrix} \frac{\partial F_1}{\partial \theta_1} & \frac{\partial F_1}{\partial \theta_0} \\ \ldots & \ldots \\ \frac{\partial F_k}{\partial \theta_1} & \frac{\partial F_k}{\partial \theta_0} \end{bmatrix} = \begin{bmatrix} x_1 & 1 \\ \ldots & \ldots \\ x_k & 1 \end{bmatrix}. \tag{A.15}$$

    (b) Next, we can select the weighting matrix $\boldsymbol{W}$ to be the identity matrix and select the residual vector as $\mathbf{y}$. Assuming that the $\boldsymbol{\theta} = [\theta_1,\, \theta_0]$ is identifiable and that $\boldsymbol{J}^{\mathrm{T}}\boldsymbol{J}$ is non-singular, we can write (e.g. according to Franklin et al., 1998) the explicit solution

    $$\boldsymbol{\theta} = \left(\boldsymbol{J}^{\mathrm{T}}\boldsymbol{J}\right)^{-1} \boldsymbol{J}^{\mathrm{T}}\boldsymbol{W}\mathbf{y}. \tag{A.16}$$

    (c) This computation is necessary for each sensor.

The presented procedure is straightforward. However, there can be certain difficulties in the utilization of the method and calibration of the position sensors. In particular:

Table A.1: Dimensions of the test rotor according to naming convention of Fig. 3.6.

Selected specification	Rotor end-A (2 sensors) / end-B (3 sensors)
Rotor diameters at sensor sleeves [mm]	110 / 70
Diameters of safety bearings [mm]	74.4 / 54.4
Rotor diameters at safety bearings [mm]	75 / 55

- The sensors may be inaccurately positioned resulting in errors in α and δ.
- The resulting vectors of magnetic forces (generated by the opposite radial electromagnets) and the x and y coordinates are misaligned.
- Measured displacement may exceed the measuring range.
- The safety bearings and magnetic bearings are positioned in a non-concentric way. The z-axes of symmetry are biased.
- Owing to non-uniform clearance and friction, the rotor cannot be positioned accurately when using the open-loop bias currents. The radii of the retainer bearings are not known precisely.
- There are errors in measurements because of a run-out of the rotor (discrepancy in the rotor shape).

As an alternative, it may be practical and easier to calibrate the sensors according to the currents in the coils (or control currents or estimated constant disturbances), in the closed-loop system. The method utilizes the gravity force vector that is assumed to be directed between the x and y axes of the rotor coordinates. The magnetic forces, in steady-state, are proportional to control currents and displacements, and therefore offsets of the sensors are adjusted to minimize differences between corresponding measured currents of the bearings that act in x and y axes (for slowly rotating rotor). In this method, the gains of the position sensors are assumed to be known. After such a calibration, for the zero displacement of the rotor, the rotor position is correlated with the operating point (only the force component, resulting from the current stiffness, is present). Next, we should measure the clearances under the closed-loop control. Finally, the rotor reference position would be given such that there are equal clearances to the touch-down bearings, in positive and negative xy directions.

A.4 Describing function for actuator saturation

The effect of the actuator saturation due to the limited DC link voltage u_{DC} can be modeled using a describing function method. For an input $u_{\mathrm{in}} = a\sin(\omega t)$, it is assumed that the output can be expressed as a Fourier series $u_{\mathrm{out}} = a_0 + \sum_{k=1}^{k=\infty} \left(a_k \cos(k\omega t) + b_k \sin(k\omega t)\right)$. The describing function of the nonlinear element is defined as "the complex ratio of the fundamental component of the nonlinear element by the input sinusoid" (Slotine and Li, 1991), that is $\Gamma(a) = \sqrt{a_1^2 + b_1^2}/a\,\angle\tan^{-1}(a_1/b_1)$. In particular, the AMB actuator saturation is a hard, memoryless nonlinearity, which is an odd function ($F(-u_{\text{in}}) = -F(u_{\text{in}})$). It can be expressed as

$$F(u_{\text{in}}) = \begin{cases} +u_{\text{DC}}, & \text{for}\, u_{\text{in}} > u_{\text{DC}} \\ u_{\text{in}}, & \text{for}\, |u_{\text{in}}| \leq u_{\text{DC}} \\ -u_{\text{DC}}, & \text{for}\, u_{\text{in}} \leq -u_{\text{DC}} \end{cases} \tag{A.17}$$

and the output Fourier series consists of sine coefficients, which depend on the input amplitude only. Therefore, the saturation describing function is $\Gamma(a) = b_1/a\,\angle 0$, where

$$b_1 = \frac{1}{\pi}\int_0^{\omega t = 2\pi} F(u_{\text{in}}) \sin(\omega t)\, d(\omega t) = \frac{4}{\pi}\int_0^{\pi/2} F(u_{\text{in}}) \sin(\omega t)\, d(\omega t). \tag{A.18}$$

Breaking the equation into two parts at the saturation point $\omega t_{\text{s}} = \sin^{-1}(u_{\text{DC}}/a)$ yields

$$b_1 = \frac{4}{\pi}\int_0^{\omega t_s} a \sin^2(\omega t)\, d(\omega t) + \frac{4}{\pi}\int_{\omega t_s}^{\pi/2} u_{\text{DC}} \sin(\omega t)\, d(\omega t). \tag{A.19}$$

Using trigonometric relationships $2\sin^2 \omega t = 1 - \cos(2\omega t)$, and $\sin(2\omega t) = 2\sin(\omega t)\cos(\omega t)$ and integrating yields

$$b_1 = \frac{2a}{\pi}\left(\omega t_{\text{s}} + \frac{u_{\text{DC}}}{a}\sqrt{1 - \left(\frac{u_{\text{DC}}}{a}\right)^2}\right). \tag{A.20}$$

The describing function becomes

$$\Gamma(a) = \left\{ \begin{array}{cl} \frac{2}{\pi}\sin^{-1}\left(\frac{u_{\text{DC}}}{a}\right) + \frac{2u_{\text{DC}}}{\pi a} \cdot \sqrt{1 - \left(\frac{u_{\text{DC}}}{a}\right)^2} & \text{for}\, a > u_{\text{DC}} \\ 1 & \text{for}\, a \leq u_{\text{DC}} \end{array} \right\}, \tag{A.21}$$

where $a = u_{\text{ref}}$ is assumed, here, to be the amplitude of the sinusoidal input of the power amplifier.

A.5 Per-unit quantities

In electrical engineering, a per-unit (pu) system is a dimensionless relative value system, which expresses all system quantities as fractions of their corresponding defined base quantities. First, the fundamental base physical quantities and their values are selected. Second, the base values of all other quantities used in the system are defined as relations of the fundamental base values. Finally, all system values are expressed as fractions of such-defined base values.

There are two main reasons to use the per-unit quantities:

- The same quantities have similar values when comparing the similar machines, regardless of their physical size or power ratings.

- In the computing systems with finite-number-representations, especially fixed point representations, the per-unit systems are better suited for accurate calculations. This applies both globally to the whole system, where all the values can fit into the specific finite-number-format and locally, e.g. realizations of specific digital arithmetic functions become much easier for normalized values. In other words, the sensitivity of the solution of a digital system to errors in the data is smaller for the system employing per-unit quantities.

In the AMB system, the following quantities are selected as the fundamental physical quantities: force f, displacement of the rotor from the central position x, current of the electromagnet i, and mass of the rotor m. The fundamental base values are selected as equal to their maximum attainable values. All other base values are derived using the fundamental base values, such as

$$k_{x,\mathrm{base}} = \tfrac{f_{\mathrm{base}}}{x_{\mathrm{base}}}, \quad k_{i,\mathrm{base}} = \tfrac{f_{\mathrm{base}}}{i_{\mathrm{base}}}, \quad \Omega_{\mathrm{base}} = \sqrt{\tfrac{k_{x,\mathrm{base}}}{m_{\mathrm{base}}}}, \tag{A.22}$$

$$I_{\mathrm{m,base}} = f_{\mathrm{base}} \frac{x_{\mathrm{base}}}{\Omega^2_{\mathrm{base}}} = m_{\mathrm{base}} x^2_{\mathrm{base}}. \tag{A.23}$$

As a consequence, all values in the per-unit system are normalized, for instance the rotor mass $m^{\mathrm{pu}} = m/m_{\mathrm{base}} = 1\,\mathrm{pu}$, the nominal air-gap length $l_0^{\mathrm{pu}} = l_0/x_{\mathrm{base}} = 1\,\mathrm{pu}$, etc.

Now, the rigid rotor continuous-time, per-unit valued state-space model is

$$\begin{aligned} \dot{\mathbf{x}}^{\mathrm{pu}} &= \Omega_{\mathrm{base}} \begin{bmatrix} \mathbf{0} & \mathbf{I} \\ (\boldsymbol{M}^{\mathrm{pu}})^{-1}\boldsymbol{K}_x^{\mathrm{pu}} & -(\boldsymbol{M}^{\mathrm{pu}})^{-1}\boldsymbol{G}^{\mathrm{pu}} \end{bmatrix} \mathbf{x}^{\mathrm{pu}} + \\ &\quad + \Omega_{\mathrm{base}} \begin{bmatrix} \mathbf{0} \\ (\boldsymbol{M}^{\mathrm{pu}})^{-1}\boldsymbol{K}_i^{\mathrm{pu}} \end{bmatrix} \mathbf{u}^{\mathrm{pu}}. \end{aligned} \tag{A.24}$$

Also the gains of the controller obtained for the model with physical quantities can be normalized. The state-space direct control feedback gain and integral control gain matrices for the rigid rotor in per-unit quantities are

$$\boldsymbol{K}^{\mathrm{pu}} = \boldsymbol{K} \begin{bmatrix} \mathbf{I} \\ \Omega_{\mathrm{base}}\mathbf{I} \end{bmatrix} \tfrac{x_{\mathrm{base}}}{i_{\mathrm{base}}}, \quad \boldsymbol{K}_{\mathrm{I}}^{\mathrm{pu}} = \boldsymbol{K}_{\mathrm{I}} \tfrac{x_{\mathrm{base}}}{i_{\mathrm{base}}}. \tag{A.25}$$

Equation (A.24) is normalized with Ω_{base} because of the normalization of the time derivatives. By the same token, in Eq. (A.25) the part of the matrix $\boldsymbol{K}$ that relates to the velocities is also normalized.

Normalizing each quantity individually is transparent and works well with simple analytical models. However, in the case of complex state-space models, like those generated by the FEM programs, identifying physical quantities behind all the values is problematic. Also in the AMB system with a flexible rotor that type of normalization is laborious.

An alternative way of obtaining the per-unit state-space system is a state transmutation, namely a similarity transformation. Now, the general continuous-time state-space model can be transformed as

$$\begin{aligned} \dot{\mathbf{x}}^{\mathrm{pu}} &= \boldsymbol{T}\boldsymbol{A}\boldsymbol{T}^{-1}\mathbf{x}^{\mathrm{pu}} + \boldsymbol{T}\boldsymbol{B}\boldsymbol{T}_u^{-1}\mathbf{u}^{\mathrm{pu}}, \\ \mathbf{y}^{\mathrm{pu}} &= \boldsymbol{T}_y\boldsymbol{C}\boldsymbol{T}^{-1}\mathbf{x}^{\mathrm{pu}} + \boldsymbol{T}_y\boldsymbol{D}\boldsymbol{T}_u^{-1}\mathbf{u}^{\mathrm{pu}}, \end{aligned} \tag{A.26}$$

where $\boldsymbol{T}$, $\boldsymbol{T}_u$, $\boldsymbol{T}_y$ are the state, input, and output variables diagonal transformation matrices, respectively. The diagonal elements of the scaling matrices are chosen as equal to inverse of the maximum attainable value of each of the state, input, and output variables. In other words, they are normalized by the selected corresponding base values, and $\Omega_{\mathrm{base}}$where applicable.

On the subject of the states, which represent the amplitudes of the flexible rotor modes, they do not have a clear physical meaning. Furthermore, the per-unit scaling is based on the physical quantities and therefore the mode shape functions in the flexible rotor model have to be normalized somewhat. They are scaled (before the per-unit scaling is applied) so that the maximum rotor deformation (from its centerline) equals 1 m.

Finally, the per-unit quantities are useful not only in a digital implementation (with fixed-point representation) of a control system but also because they may improve reliable computations in control synthesis and transformations of linear time-invariant (LTI) models. A documentation of the Control System Toolbox (Matlab 1999), suggests that well-scaled (conditioned) models are a prerequisite for obtaining an accurate results. Indeed, in Matlab, the automatic diagonal scaling has been employed, including a function to calculate eigenvalues (eig). Matrices of control systems in state-space form, with per-unit quantities, are well conditioned with respect to inversion and, in general, constitute reliable models for subsequent computations. By contrast, popular canonical realizations, such as Matlab canon, controllability staircase form (ctrbf), or observability staircase form (obsvf) produce mathematically elegant models but might be badly scaled and sensitive to perturbations of the data (e.g. eigenvalues and eigenvectors of a matrix in companion canonical form could be sensitive to perturbations). Therefore, they are not recommended to be used in control design, and also definitely not recommended to be used in the digital implementations of state-space computations. However, they can be safely used and are practical in analysis.

A.6 Stability conditions of the lead compensator

The open-loop transfer function that consists of 1-DOF system (3.1) and lead compensator is

$$G_{\mathrm{ol}} = G_{\mathrm{P,ld}} \frac{(\tau_{\mathrm{ld}} s + 1) k_i}{(a_{\mathrm{ld}} \tau_{\mathrm{ld}} s + 1)(m s^2 - k_x)}. \tag{A.27}$$

Now, the characteristic equation of the closed-loop transfer function $G_{\mathrm{cl}} = G_{\mathrm{ol}}/(1 + G_{\mathrm{ol}})$ yields

$$P_{\mathrm{p}}(s) = a_3 s^3 + a_2 s^2 + a_1 s + a_0, \tag{A.28}$$

where the Hurwitz coefficients $a_3 = m a_{\mathrm{ld}} \tau_{\mathrm{ld}}$, $a_2 = m$, $a_1 = G_{\mathrm{P,ld}} k_i \tau_{\mathrm{ld}} - k_x a_{\mathrm{ld}} \tau_{\mathrm{ld}}$, and $a_0 = G_{\mathrm{P,ld}} k_i - k_x$ must be positive. For the third-order system, the Hurwitz conditions are

$$\Lambda_1 = a_2 > 0, \tag{A.29}$$

$$\Lambda_2 = \begin{vmatrix} a_2 & a_3 \\ a_0 & a_1 \end{vmatrix} > 0, \tag{A.30}$$

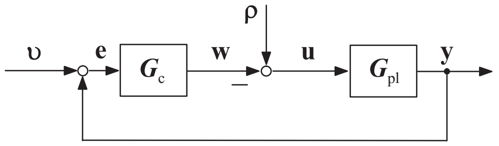

Figure A.4: General control system, where $\boldsymbol{\rho}$, $\mathbf{u}$, $\mathbf{y}$, $\boldsymbol{\upsilon}$, $\mathbf{e}$, $\mathbf{w}$ may be perceived as the input disturbance, plant input, plant output, output disturbance (or reference signal), measured plant output (or error signal), and control signal (control effort) vectors, respectively.

Table A.2: Closed-loop transfer functions (function matrices) of the feedback control system

Description	Equation
Input sensitivity$^{(A)}$ $(\mathbf{u} \leftarrow \boldsymbol{\rho})$	$(\mathbf{I} + \boldsymbol{G}_c\boldsymbol{G}_{pl})^{-1}$
Output sensitivity$^{(B)}$ $(\mathbf{e} \leftarrow \boldsymbol{\upsilon})$	$(\mathbf{I} + \boldsymbol{G}_{pl}\boldsymbol{G}_c)^{-1}$
Input complementary sensitivity$^{(A)}$ $(\mathbf{w} \leftarrow \boldsymbol{\rho})$	$\boldsymbol{G}_c\boldsymbol{G}_{pl}(\mathbf{I} + \boldsymbol{G}_c\boldsymbol{G}_{pl})^{-1}$
Output complementary sensitivity$^{(B)}$$(\mathbf{y} \leftarrow \boldsymbol{\upsilon})$	$\boldsymbol{G}_{pl}\boldsymbol{G}_c(\mathbf{I} + \boldsymbol{G}_{pl}\boldsymbol{G}_c)^{-1}$
No common name $(\mathbf{u} \leftarrow \boldsymbol{\upsilon})$	$\boldsymbol{G}_c(\mathbf{I} + \boldsymbol{G}_{pl}\boldsymbol{G}_c)^{-1}$

$^{(A)}$ at the input of the plant; $^{(B)}$ at the output of the plant

$$\Lambda_3 = \begin{vmatrix} a_2 & a_3 & 0 \\ a_0 & a_1 & a_2 \\ 0 & 0 & a_0 \end{vmatrix} = a_0\Lambda_2 > 0, \tag{A.31}$$

where Λ_k denote the Hurwitz determinants. From these conditions it follows that the feedback system is asymptotically stable if

$$0 < a_{\mathrm{ld}} < 1,\, G_{\mathrm{P,ld}} > \frac{k_x}{k_i}. \tag{A.32}$$

A.7 Closed-loop transfer functions

Throughout the dissertation, the closed-loop transfer functions of SISO and transfer function matrices of MIMO systems are used. The schematic of the general system is presented in Fig. A.4, and the closed-loop transfer functions (function matrices) of the control system are summarized in Table A.2. In the transfer functions (function matrices) of the plant-controller feedback loop, $\boldsymbol{G}_c$ and $\boldsymbol{G}_{pl}$ are the controller (compensator in the feedback path, without a reference path) and plant, respectively.

In multivariable control feedback systems, it is possible to quantify the performance and stability margins of these systems by using the singular values of the closed-loop transfer function matrices, as suggested by Lewis and Syrmos (1995) or Balas et al. (2007). The singular values plot of the output sensitivity function corresponds to the disturbance attenuation performance in measured signal, and a specification of disturbance attenuation can be written as

$$\bar{\sigma}\left((\mathbf{I} + \boldsymbol{G}_{pl}\boldsymbol{G}_c)^{-1}\right) \le \left|W_1^{-1}(\omega)\right|, \tag{A.33}$$

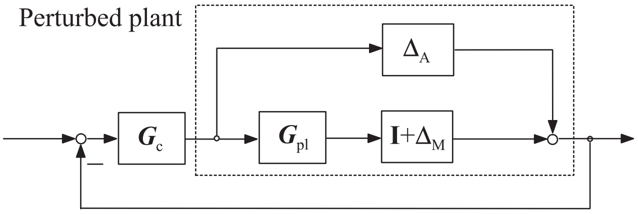

Figure A.5: Multiplicative and additive plant perturbations (Balas et al., 2007)

where $\left|W_1^{-1}(\omega)\right|$ is the disturbance attenuation factor. The singular values plot of the transfer function matrix from the input $\boldsymbol{v}$ to the output $\mathbf{u}$ may be perceived as a general margin of the stability in regard to additive plant perturbations Δ_{A}. The singular values plot of the output complementary sensitivity function may be perceived as a general margin of the stability in regard to multiplicative plant perturbations Δ_{M}. These stability margins of MIMO control system can be written as

$$\bar{\sigma}\left(\boldsymbol{G}_{\mathrm{c}}\left(\mathbf{I}+\boldsymbol{G}_{\mathrm{pl}}\boldsymbol{G}_{\mathrm{c}}\right)^{-1}\right) \leq \left|W_2^{-1}(\omega)\right|, \tag{A.34}$$

$$\bar{\sigma}\left(\boldsymbol{G}_{\mathrm{pl}}\boldsymbol{G}_{\mathrm{c}}\left(\mathbf{I}+\boldsymbol{G}_{\mathrm{pl}}\boldsymbol{G}_{\mathrm{c}}\right)^{-1}\right) \leq \left|W_3^{-1}(\omega)\right|, \tag{A.35}$$

where $|W_2(\omega)|$ and $|W_3(\omega)|$ are the additive plant discrepancy bound and the multiplicative plant discrepancy bound, respectively. The $|W_2(\omega)| = \bar{\sigma}\left(\Delta_{\mathrm{A}}(\omega)\right)$ and $|W_3(\omega)| = \bar{\sigma}\left(\Delta_{\mathrm{M}}(\omega)\right)$. The multiplicative and additive plant perturbations (uncertainties) are explained in Fig. A.5.

The smaller are the maximum singular values in Eq. (A.34) and (A.35), the greater will be the minimum destabilizing additive and multiplicative perturbation, respectively.

The input complementary sensitivity is used in the computation of the maximum tolerated disturbance force (e.g. Fig. 4.12C), which may be perceived as a measure of the disturbance force attenuation performance.

Appendix B

Details of the prototype platform

B.1 Prototype dimensions

As to the listed parameters of the radial (B.1) and axial (B.2) AMBs, the inductance, current stiffness, and position stiffness are linearized in the operating point, that is, the rotor (B.3) is assumed to be in the central position and there is only a bias current applied to the coils. In the case of the axial bearing, the stator inner and outer radius correspond to the dimensions of the pole located radially closer to the shaft. The dimensions of the other pole are scaled in such a way that both poles have the same pole face area.

Table B.1: Main dimensions and parameters of the radial magnetic bearings

Stator diameter [mm]	180	Turns per magnet	180
Core length [mm]	60	Resistance [Ω]	0.43
Width of the stator teeth [mm]	18	Inductance [H]	0.042
Slot to slot diameter [mm]	144	Current stiffness [$\frac{N}{A}$]	268
Shaft diameter [mm]	60	Position stiffness [$\frac{N}{mm}$]	992
Rotor outer diameter [mm]	89.8	DC link voltage [V]	250
Nominal air-gap length [mm]	0.6	Bias current [A]	2.5
Mechanical air-gap length [mm]	0.5	Maximum current [A]	10

Table B.2: Main dimensions and parameters of the axial magnetic bearing

Stator outer radius [mm]	36	Resistance [Ω]	0.52
Stator inner radius [mm]	27.5	Inductance [H]	0.045
Nominal air-gap length [mm]	0.5	Current stiffness [$\frac{N}{A}$]	213
Mechanical air-gap length [mm]	0.3	Position stiffness [$\frac{N}{mm}$]	1065
Thickness of disk [mm]	8.9	Bias current [A]	2.5
Number of turns per magnet	100	Maximum current [A]	10
DC link voltage [V]	250		

Table B.3: Main parameters of the studied rotor

Shaft mass, rotor mass [kg]	36.5, 46.2
Transversal moment of inertia [kg·m^2]	4.80
Polar moment of inertia [kg·m^2]	0.041
Location of radial bearings in z direction$^{(A)}$ d_A, d_B [m]	0.388, 0.352

$^{(A)}$ measured from the center of mass

B.2 Specification of control electronics

This appendix contains the selected specification for the control electronics in the AMB rotor prototype system. Brief specifications for current and position sensors, ADCs, processing units, and other control electronics are also included.

Current and position sensors specification

As the current sensors, closed-loop Hall-effect LEM compensated transducers (LA 25-NP) are used. Their selected specification is summarized in Table B.4.

Table B.4: LEM current sensors LA 25-NP

selected specification	
measuring range [A]	0–36
output range (at the input to ADC) [V]	0–3.75
accuracy at i_{PN}=25 A [%]	±0.5
linearity [%]	0.2
response time [μs]	1
frequency bandwidth (-1 dB) [kHz]	0–150

In the prototype, as the displacement sensors, eddy current type sensors are used. Their selected specification is summarized in Table B.5 and B.6. For measuring the radial displacements, the MICRO-EPSILON's three single-channel position sensors (DT3701 U1-A-C3), and two differential sensors (DT3703 U3-A-C3), are used. One single-channel CMSS 68 sensor, by SKF, is used for measuring the axial displacement.

Table B.5: Single-channel position sensors (DT3701 U1-A-C3), and differential sensors (DT3703 U3-A-C3)

selected specification	U1(U3)
measuring range [mm]	0.1–1 (0.3–1.5)
output range (from driver) [V]	0–2.5
dynamic resolution at 1 kHz [nm]	1.5 (2.25)
linearity [%]	±6 (±5)
frequency bandwidth (-3 dB) [kHz]	10
measurement target	Al

Table B.6: Single-channel CMSS 68 sensor, by SKF

selected specification	
measuring range [mm]	0.2–2.5
output range (from driver) [V]	0– -18
dynamic resolution at 1 kHz [nm]	–
linearity [%]	±1.1
frequency bandwidth (-3 dB) [kHz]	10
measurement target	Fe

Specification of the ADC boards

There are three DS2001 ADC boards connected to the dSPACE and one custom-built ADC board connected to FPGA-based control platform (three AD7856, multiplexed ADCs). Their selected specification is summarized in Table B.7.

Table B.7: Specification of the ADC boards

selected specification	DS2001	custom-built
number of ADC channels per board	5	18
resolution	16-bit	14-bit
conversion time [μs]	5.0	>5.3
input range [V]	±5 or ±10	0 to +5
organization of inputs	parallel	8 multiplexed
cut off frequency, current (position)	–	14kHz (3kHz)

Components of the dSPACE and FPGA-based platforms

The dSPACE platform comprises the DS4003 Digital I/O board (96 TTL I/Os), DS1005-09 PowerPC board (PowerPC 750FX running at 800MHz, 512 KB level 2 cache, 128 MB SDRAM), DS2001 ADC boards and PC. The FPGAs in the system are: the Spartan-II and Virtex-II Pro Fabricated in 0.13 μm, 1.5V process technology. The utilized Virtex-II Pro (xc2vp30) incorporates two embedded PowerPC 32-bit reduced instruction set computer (RISC) processors, 136 18-bit hardware multipliers, 2448 Kb Block RAM, 30816 logic cells and 644 I/O pads.

ACTA UNIVERSITATIS LAPPEENRANTAENSIS

244. AARNIO, TEIJA. Challenges in packaging waste management: A case study in the fast food industry. 2006. Diss.

245. PANAPANAAN, VIRGILIO M. Exploration of the social dimension of corporate responsibility in a welfare state. 2006. Diss.

246. HEINOLA, JANNE-MATTI. Relative permittivity and loss tangent measurements of PWB materials using ring resonator structures. 2006. Diss.

247. SALMELA, NINA. Washing and dewatering of different starches in pressure filters. 2006. Diss.

248. SISSONEN, HELI. Information sharing in R&D collaboration – context-dependency and means of governance. 2006. Diss.

249. PURANEN, JUSSI. Induction motor versus permanent magnet synchronous motor in motion control applications: a comparative study. 2006. Diss.

250. PERÄLÄ, KARI. Kassanhallintakäytännöt Suomen kunnissa. 2006. Diss.

251. POUTIAINEN, ILKKA. A modified structural stress method for fatigue assessment of welded structures. 2006. Diss.

252. LIHAVAINEN, VELI-MATTI. A novel approach for assessing the fatigue strength of ultrasonic impact treated welded structures. 2006. Diss.

253. TANG, JIN. Computational analysis and optimization of real gas flow in small centrifugal compressors. 2006. Diss.

254. VEHVILÄINEN, JUHA. Procurement in project implementation. 2006. Diss.

255. MIROLA, TUULI. Impacts of the European integration and the European Union membership on Finnish export industries – Perceptions of export business managers. 2006. Diss.

256. RAUMA, KIMMO. FPGA-based control design for power electronic applications. 2006. Diss.

257. HIRVONEN, MARKUS. On the analysis and control of a linear synchronous servomotor with a flexible load. 2006. Diss.

258. LIU, JUNHONG. On the differential evolution algorithm and its application to training radial basis function networks. 2006. Diss.

259. LAITINEN, RISTO. Development of LC-MS and extraction methods for the analyses of AKD, ASA, and rosin sizes in paper products. 2006. Diss.

260. KUISMA, PETRI. Seinärakenteen infrapunakontrastin pienentäminen käyttäen ilmajäähdytystä ja säteilysuojausta. 2007. Diss.

261. ELLONEN, HANNA-KAISA. Exploring the strategic impact of technological change – studies on the role of Internet in magazine publishing. 2007. Diss.

262. SOININEN, AURA. Patents in the information and communications technology sector – development trends, problem areas and pressures for change. 2007. Diss.

263. MATTILA, MERITA. Value processing in organizations – individual perceptions in three case companies. 2007. Diss.

264. VARTIAINEN, JARKKO. Measuring irregularities and surface defects from printed patterns. 2007. Diss.

265. VIRKKI-HATAKKA. TERHI. Novel tools for changing chemical engineering practice. 2007. Diss.

266. SEKKI, ANTTI. Successful new venturing process implemented by the founding entrepreneur: A case of Finnish sawmill industry. 2007. Diss.

267. TURKAMA, PETRA. Maximizing benefits in information technology outsourcing. 2007. Diss.

268. BUTYLINA, SVETLANA. Effect of physico-chemical conditions and operating parameters on flux and retention of different components in ultrafiltration and nanofiltration fractionation of sweet whey. 2007. Diss.

269. YOUSEFI, HASSAN. On modelling, system identification and control of servo-systems with a flexible load. 2007. Diss.

270. QU, HAIYAN. Towards desired crystalline product properties: In-situ monitoring of batch crystallization. 2007. Diss.

271. JUSSILA, IIRO. Omistajuus asiakasomisteisissa osuuskunnissa. 2007. Diss.

272. 5th Workshop on Applications of Wireless Communications. Edited by Jouni Ikonen, Matti Juutilainen and Jari Porras. 2007.

273. 11th NOLAMP Conference in Laser Processing of Materials Lappeenranta, August 20-22, 2007. Ed. by Veli Kujanpää and Antti Salminen. 2007.

274. 3rd JOIN Conference Lappeenranta, August 21-24, 2007. International Conference on Total Welding Management in Industrial Applications. Ed. by Jukka Martikainen. 2007.

275. SOUKKA, RISTO. Applying the principles of life cycle assessment and costing in process modeling to examine profit-making capability. 2007. Diss.

276. TAIPALE, OSSI. Observations on software testing practice. 2007. Diss.

277. SAKSA, JUHA-MATTI. Organisaatiokenttä vai paikallisyhteisö: OP-ryhmän strategiat institutionaalisten ja kilpailullisten paineiden ristitulessa. 2007. Diss.

278. NEDEOGLO, NATALIA. Investigation of interaction between native and impurity defects in ZnSe. 2007. Diss.

279. KÄRKKÄINEN, ANTTI. Dynamic simulations of rotors during drop on retainer bearings. 2007. Diss.

280. KARPOVA, TATJANA. Aqueous photocatalytic oxidation of steroid estrogens. 2007. Diss.

281. SHIPILOVA, OLGA. Particle transport method for convection-diffusion-reaction problems. 2007. Diss.

282. ILONEN, JARMO. Supervised local image feature detection. 2007. Diss.

283. BOTAR-JID, CLAUDIU CRISTIAN. Selective catalytic reduction of nitrogen oxides with ammonia in forced unsteady state reactors. Case based and mathematical model simulation reasoning. 2007. Diss.

284. KINNUNEN, JANNE. Direct-on-line axial flux permanent magnet synchronous generator static and dynamic performance. 2007. Diss.

285. VALTONEN, MIKKO. Performance characteristics of an axial-flux solid-rotor-core induction motor. 2007. Diss.

286. PUNNONEN, PEKKA. Impingement jet cooling of end windings in a high-speed electric machine. 2007. Diss.